



# DIGITAL ACCESS TO SCHOLARSHIP AT HARVARD

## Bioinspired, Dynamic, Structured Surfaces for Biofilm Prevention

The Harvard community has made this article openly available.  
[Please share](#) how this access benefits you. Your story matters.

<b>Citation</b>	Epstein, Alexander. 2012. Bioinspired, Dynamic, Structured Surfaces for Biofilm Prevention. Doctoral dissertation, Harvard University.
<b>Accessed</b>	April 17, 2018 3:42:27 PM EDT
<b>Citable Link</b>	<a href="http://nrs.harvard.edu/urn-3:HUL.InstRepos:9904009">http://nrs.harvard.edu/urn-3:HUL.InstRepos:9904009</a>
<b>Terms of Use</b>	This article was downloaded from Harvard University's DASH repository, and is made available under the terms and conditions applicable to Other Posted Material, as set forth at <a href="http://nrs.harvard.edu/urn-3:HUL.InstRepos:dash.current.terms-of-use#LAA">http://nrs.harvard.edu/urn-3:HUL.InstRepos:dash.current.terms-of-use#LAA</a>

*(Article begins on next page)*

© 2012 – Alexander K Epstein  
All rights reserved.

# BIOINSPIRED, DYNAMIC, STRUCTURED SURFACES FOR BIOFILM PREVENTION

## Abstract

Bacteria primarily exist in robust, surface-associated communities known as biofilms, ubiquitous in both natural and anthropogenic environments. Mature biofilms resist a wide range of biocidal treatments and pose persistent pathogenic threats. Treatment of adherent biofilm is difficult, costly, and, in medical systems such as catheters, frequently impossible. Adding to the challenge, we have discovered that biofilm can be both impenetrable to vapors and extremely nonwetting, repelling even low surface tension commercial antimicrobials. Our study shows multiple contributing factors, including biochemical components and multiscale reentrant topography.

Reliant on surface chemistry, conventional strategies for preventing biofilm only transiently affect attachment and/or are environmentally toxic. In this work, we look to Nature's antifouling solutions, such as the dynamic spiny skin of the echinoderm, and we develop a versatile surface nanofabrication platform. Our benchtop approach unites soft lithography, electrodeposition, mold deformation, and material selection to enable many degrees of freedom—material, geometric, mechanical, dynamic—that can be programmed starting from a single master structure. The mechanical properties of the bio-inspired nanostructures, verified by AFM, are precisely and rationally tunable.

We examine how synthetic dynamic nanostructured surfaces control the attachment of pathogenic biofilms. The parameters governing long-range patterning of bacteria on high-aspect-ratio (HAR) nanoarrays are combinatorially elucidated, and we

discover that sufficiently low effective stiffness of these HAR arrays mechanoselectively inhibits ~40% of *Pseudomonas aeruginosa* biofilm attachment. Inspired by the active echinoderm skin, we design and fabricate externally actuated dynamic elastomer surfaces with active surface microtopography. We extract from a large parameter space the critical topographic length scales and actuation time scales for achieving nearly ~80% attachment reduction. We furthermore investigate an atomically mobile, slippery liquid infused porous surface (SLIPS) inspired by the pitcher plant. We show up to 99.6% reduction of multiple pathogenic biofilms over a 7-day period under both static and physiologically realistic flow conditions—a ~35x improvement over state-of-the-art surface chemistry, and over a far longer timeframe. Moreover, SLIPS is shown to be nontoxic: bacteria simply cannot attach to the smooth liquid interface.

These bio-inspired strategies significantly advance biofilm attachment prevention and promise a tremendous range of industrial, clinical, and consumer applications.

## TABLE OF CONTENTS

<b>1. Acknowledgments .....</b>	<b>1</b>
<b>2. Bacterial biofilm and biofouling .....</b>	<b>2</b>
A. BIOFILM AS THE NORMAL MODE OF EXISTENCE FOR EARTH’S PREDOMINANT ORGANISMS, BACTERIA .....	2
B. IMPACTS: ECONOMIC/INDUSTRIAL DAMAGE AND MORTALITY/HEALTH CONTEXT .....	3
C. LIMITATIONS OF CONVENTIONAL ANTIMICROBIAL SURFACES AND TREATMENTS.....	4
D. BIOFILM NONWETTABILITY AS CHALLENGE AND MOTIVATION.....	9
I. <i>Liquid resistance—including ethanol and common disinfectants.....</i>	<i>11</i>
1. Contact angle goniometry and confocal microscope visualization .....	11
2. Scope of wetting resistance to antimicrobials .....	15
3. Stability of the biofilm’s nonwetting function .....	16
4. Genetic mutants and biochemical factors.....	18
5. Decoupling surface topography and chemistry .....	20
II. <i>Vapor resistance—synchrotron microCT .....</i>	<i>24</i>
E. MULTIFUNCTIONAL HAR FIBROUS ARRAYS IN NATURE PROVIDE BIOLOGICAL INSPIRATION FOR MATERIALS SCIENCE SOLUTIONS .....	32
<b>3. Fabrication of bioinspired structures and applications .....</b>	<b>37</b>
A. BENCHTOP SOFT LITHOGRAPHIC DOUBLE-CASTING METHOD.....	37
B. MASTER DESIGN OPTIONS .....	39
C. NEGATIVE MOLD CONSIDERATIONS.....	40
D. DOUBLE REPLICATION EXPERIMENTAL DETAILS .....	41
E. BREAKING THE ONE-TO-ONE REPLICATION BARRIER WITH ELASTOMERIC MOLD DEFORMATION: ARRAY-LEVEL GEOMETRY CONTROL .....	44

F.	CONTROL OF THE MECHANICAL AND OTHER PROPERTIES BY MATERIAL SELECTION .....	49
G.	BEYOND PROPORTIONAL TRANSFORMATION: FEATURE-LEVEL CONTROL OF GEOMETRY, MECHANICS, AND FUNCTION BASED ON STRUCTURAL TRANSFORMATION BY ELECTRODEPOSITION ON PATTERNED SUBSTRATES (STEPS) .....	58
H.	UNIFYING THE FABRICATION PLATFORM TO RATIONALLY PROGRAM NANOSTRUCTURE PERFORMANCE.....	61
<b>4.</b>	<b>Empirical nanopost mechanical properties to validate design and evaluate for applications.....</b>	<b>64</b>
A.	MOTIVATION FOR AN EMPIRICAL CHARACTERIZATION METHOD .....	64
B.	NANOINDENTATION (NI) FOR MULTI-STRUCTURE MEASUREMENTS OF ENGINEERED POLYMERIC MICROSTRUCTURES .....	65
C.	ATOMIC FORCE MICROSCOPY (AFM) FOR SINGLE-STRUCTURE MEASUREMENTS OF ENGINEERED POLYMERIC NANOSTRUCTURES.....	67
D.	VALIDATION OF AFM-BASED MECHANICAL CHARACTERIZATION .....	67
E.	APPLICATION-CRITICAL DYNAMIC MECHANICAL PROPERTIES: STRAIN HARDENING, FATIGUE, VISCOELASTICITY .....	69
<b>5.</b>	<b>Biofilm culture and quantification methods for study of antifouling structured surfaces.....</b>	<b>71</b>
A.	SONICATION, DISPERSAL, AND COLONY FORMING UNIT (CFU) ASSAY .....	71
B.	FLUORESCENCE MICROCOPY AND POST-PROCESSING .....	72
C.	SCANNING ELECTRON MICROCOPY IMAGING .....	73
D.	CRYSTAL VIOLET STAINING AND SPECTROPHOTOMETRY.....	73
E.	BACTERIAL BIOFILM CULTURE PROTOCOLS.....	73
<b>6.</b>	<b>Dynamic structured surfaces for control of biofilm attachment .....</b>	<b>75</b>
A.	PASSIVE STRUCTURES .....	76

I.	<i>Robust control of bacterial patterning and contact mode by tunable interstitial spacing and symmetry</i> .....	76
II.	<i>Effective compliance of HAR nanostructures and mechanoselective adhesion below threshold value</i> .....	84
B.	MECHANICAL ACTUATION .....	89
III.	<i>Uniaxial tensile instrument overview</i> .....	91
IV.	<i>Bottom-up dynamic elastomeric wrinkles</i> .....	94
1.	Wrinkling mechanism, characterization, and control .....	94
2.	Parameter space explored .....	97
A.	<i>Strain amplitude, rate, intermittent vs. continuous</i> .....	97
B.	<i>Topography length scale</i> .....	100
C.	<i>Growth time scale</i> .....	102
D.	<i>Bacterial species dependence</i> .....	102
V.	<i>Top down high-aspect-ratio posts</i> .....	106
1.	Notional results .....	106
C.	MOLECULARLY MOBILE: SLIPPERY LIQUID INFUSED POROUS SURFACE (SLIPS) .....	109
VI.	<i>Bioinspiration from the pitcher plant and the nonwetable biofilm</i> ...	109
1.	Fabrication overview .....	112
VII.	<i>Static condition growth</i> .....	113
1.	Attachment comparison to Teflon and superhydrophobic silicon nanoarrays .....	113
2.	Biofilm slime evaporation, adhesion, and removal .....	117
VIII.	<i>Flow condition growth</i> .....	119
1.	Context of physiological and engineered system flows .....	119
2.	Stability of SLIPS function under prolonged flow .....	120
3.	Cytotoxicity screening via growth curves .....	124
4.	Multiple species and extended growth time scales .....	125
IX.	<i>Prospects for technological development</i> .....	129
<b>7.</b>	<b>Conclusions</b> .....	<b>130</b>
A.	ALL STRUCTURED SURFACES COMPARED FOR EFFECTIVENESS AGAINST BIOFILM ATTACHMENT .....	130

B.	FUTURE BIOINSPIRED ANTIFOULING SURFACE OPPORTUNITIES.....	132
<b>8.</b>	<b>Appendix.....</b>	<b>135</b>
A.	HIERARCHICAL FIBROUS SUPERHYDROPHOBIC SURFACES FOR TUNABLE WETTING PROPERTIES.....	135
B.	COPYRIGHT PERMISSIONS .....	140
<b>9.</b>	<b>List of publications.....</b>	<b>146</b>
<b>10.</b>	<b>References.....</b>	<b>147</b>



## LIST OF FIGURES AND TABLES

Figure 1. Biofilm lifecycle and exemplary health and economic impacts of biofilms. ....	3
Figure 2. Fluorescence images of <i>P. aeruginosa</i> bacterial growth on epoxy (UVO-114) flat substrates functionalized with hydrophobic/hydrophilic and variously charged surface chemistries. ....	6
Figure 3. Bacterial biofilm wetting characterization by contact angle analysis. ....	12
Figure 4. The linearly decreasing trend of contact angle as a function of increasing ethanol concentration observed in a range of hydrophobic materials.....	13
Figure 5. Fluorescent confocal z-stack showing 3D rhodamine staining of <i>B. subtilis</i> colony integrated through the thickness of the film.....	14
Table 1. Contact angles of aqueous solutions of organic solvents on <i>B. subtilis</i> biofilms .....	16
Table 2. Commercial biocides on <i>B. subtilis</i> wild type biofilms .....	16
Figure 6. Persistent biofilm nonwettability is invariable with respect to ethanol concentration across the repellent concentration range. ....	17
Figure 7. Characterization of liquid repellency mechanisms using genetic mutants of <i>B. subtilis</i> biofilms .....	19
Figure 8. Testing role of topography using functionalized polymeric replicas of biofilm microstructure.....	22
Figure 9. Comparison of the WT and sinR mutant morphologies at corresponding magnifications via SEM.....	23
Figure 10. Synchrotron micro-CT reconstructed images of the .....	25
Figure 11. Bio-inspirations for functional surfaces that self-clean and prevent biofouling.....	34
Figure 12. Two-step soft lithography process for creating replicas of nanostructured surfaces with high-aspect-ratio features.....	38
Figure 13. Schematic three-dimensional renderings of various deformations of the PDMS mold, which allow the fabrication of arbitrary arrays of nanoposts with finely-tuned geometries and nontrivial configurations. ....	45

Figure 14. SEM image of an epoxy nanopost array fabricated using a compound deformation .....	47
Table 3. Deformation-induced changes in the geometry of the replicated nanostructures. ....	48
Figure 15. The overall fabrication platform for bioinspired arrays of high-aspect-ratio nanostructures. ....	50
Figure 16. Three orders of stiffness magnitude are accessible via simple prepolymer mixing. ....	53
Figure 17. Anchoring point flexibility is seen in the hybrid stiffness nanoarray replica.....	55
Figure 18. Mechanical in-plane actuation of micro/nanoscale rigid posts that are attached to a flexible, extendible elastomeric substrate, strained by a motorized stage. ....	56
Figure 19. SEM images of electron beam actuated epoxy nanoposts.....	57
Figure 20. Relationships between geometric parameters and the applied force required at the tip of a nanopost to bend it to a given deflection.....	63
Figure 21. SEM images showing mechanical reinforcement of a microstructure by shape transformation using STEPS methods. ....	66
Figure 22. Empirical characterization of nanopost mechanical properties.....	68
Figure 23. Colony-forming unit method of biofilm quantification.....	72
Figure 24. Preferential bacterial attachment in anisotropic environment. ....	77
Figure 25. Schematic of the orthogonal double gradient substrate fabrication, adapting the recently described STEPS method .....	80
Figure 26. Fluorescence images and corresponding Fourier transforms of spontaneously patterned <i>P. aeruginosa</i> bacteria on the combinatorial nanoarray substrate.....	83
Figure 27. Leaching and toxicity screening performed using 20 nm Au-coated samples of a range of candidate polymers. ....	86
Figure 28. Colony forming unit (CFU) measurements of <i>P. aeruginosa</i> biofilm growth on both unpatterned and high-aspect-ratio (HAR) nanopost substrates fabricated from polymers of varying Young's modulus. ....	86

Figure 29. The experimental setup for biofilm growth on dynamic surfaces. ....	91
Figure 30. Fabrication and actuation of periodically wrinkled PDMS elastomer substrates .....	94
Figure 31. As imaged by fluorescence microscopy, (a) the attachment of <i>Pseudomonas aeruginosa</i> PA-14 bacteria on a flat PDMS surface appears random and isotropic, while (b) the bacteria spontaneously pattern on PDMS wrinkles .....	94
Figure 32. Bacterial biofilm attachment after 24 hr growth on elastomeric substrates with respect to topography, dynamic strain (cycling between 10% and 30%), and dwell time between strain events.....	98
Figure 33. Effect of dynamic elastomer surface wrinkle length scale and continuously applied cyclic strain on 24 hr bacterial biofilm attachment. ....	101
Figure 34. Attachment inhibition of <i>Pseudomonas aeruginosa</i> biofilm owing to dynamic strain persists at .....	103
Figure 35. The species dependence of biofilm attachment following 24 hr growth under the matrix of substrate conditions was screened using .....	104
Figure 36. Geometry and replication issues of HAR high-density hexagonal post array. (a) SEM image of original silicon master with photoresist conical tips. (b) Higher magnification showing interstitial dimensions. (c) Side view of single conical-tip nanopost. (d) Replication defects that appeared in PDMS elastomeric replicas.....	107
Figure 37. Effects of PDMS hexagonal HAR conical nanopost array and dynamic strain. Biofilm attachment decreased with the application of dynamic strain, but the addition of the hexagonal array resulted in larger attachment increases. ....	109
Figure 38. Biofilm attachment properties of surface typologies investigated in this study.....	114
Figure 39. 48-hour <i>P. aeruginosa</i> biofilm puddles grown at room temperature on a superhydrophobic nanopost array silicon wafer, subsequently tilted to observe biofilm adhesion. ....	115

Figure 40. <i>P. aeruginosa</i> biofilm puddles grown 24 h on a PTFE porous surface and a PTFE SLIPS surface infused with Krytox 103 .....	116
Figure 41. Split-frame still images and movie showing evaporation dynamics of <i>P. aeruginosa</i> culture droplets on a superhydrophobic PTFE porous surface and a PTFE SLIPS surface infused with Krytox 103.....	116
Figure 42 .Due to the low adhesion of the biofilm-forming bacterial droplet on the SLIPS, the dried bacteria following evaporation of the droplet can be removed from SLIPS simply by adhesive tape.....	118
Figure 43. SLIPS stability in the flow. The tilt angle of water droplets on the surface of the SLIPS was measured over the course of 7 d under water flow of 10mL/min (1 cm/s) through the dual chamber.....	120
Figure 44. Macroscale view of biofilm attachment inhibition on SLIPS. ....	121
Figure 45. Microscale view of <i>P. aeruginosa</i> biofilm attachment on SLIPS and control PTFE surfaces after 24 hour and 7-day growths in 10 mL/min flow. ....	123
Figure 46. Biofilm attachment reduction by SLIPS is species independent.....	126
Figure 47. Efficacy and duration comparison of bioinspired biofilm prevention methods compared to state of the art surface chemistry. ....	131
Figure 48. Five potentially high-impact opportunities for developing future anti-biofilm technology based on our proofs of principle.....	133
Figure 49. Photographs of a water droplet sitting on large area of bulk deposited polypyrrole structures to show the contact angle between the two surfaces in air. ....	136
Figure 50. Three nanostructured surfaces and their wetting properties.....	138

## 1. Acknowledgments

In addition to my advisor Joanna Aizenberg and my informal mentors Boaz Pokroy, Allon Hochbaum, and Philseok Kim, I wish to acknowledge the support of many colleagues and friends. I am grateful to Moshe Shemesh, Yunrong (Win) Chai, Ilana Kolodkin-Gal, Hera Vlamakis, and Sigolene Lecuyer for providing plates, medium, cultures, and invaluable guidance in microbiology tips and techniques. I wish to thank Tommy Angelini for assistance with confocal microscopy, in addition to Prof. Richard Losick (Department of Molecular and Cellular Biology) for allowing me to use a variety of lab equipment. Dr. Alison Grinthal provided insightful assistance and critique of my manuscripts. JD Deng (of CNS) made time to assist in tricky multi-week AFM experiments and Claudia Friedsam assisted with nanoindentation at the Wyss. Picking up where my own engineering left off, James Weaver and Tom Blough graciously fabricated a flow cell and significantly upgraded my uniaxial tensile instrument. And I have valued the camaraderie of my fellow inaugural students, Sung Hoon and Lidiya.

Use of the Advanced Photon Source was supported by the U.S. Department of Energy, Office of Science, Office of Basic Energy Sciences, under Contract No. W-31-109-Eng-38. The BASF Advanced Research Initiative is acknowledged for partial funding of the biofilm research, and the Robert L. Wallace Prize Fellowship for my 2008-2009 funding. This work was performed in part at the Center for Nanoscale Systems (CNS) at Harvard University, a member of the National Nanotechnology Infrastructure Network (NNIN), which is supported by the National Science Foundation under NSF award no. ECS-0335765.

## **2. Bacterial biofilm and biofouling**

### **A. Biofilm as the normal mode of existence for Earth's predominant organisms, bacteria**

Bacteria, the most numerous organisms on earth, represent more biomass than that of all plants and animals combined. (1) Yet, contrary to what was believed as recently as twenty years ago, bacteria exist in nature predominantly as members of biofilms—structured, multicellular communities adherent to surfaces in natural and anthropogenic environments. (2) Biofilms protect their constituent cells in various ways, which makes both clinical and industrial contamination difficult to treat. As self-organized communities, biofilms have evolved to feature differentiated cell phenotypes performing complimentary functions. The associated cooperative behavior of bacterial cells, mediated by cell-cell communications and other factors, enables an increased metabolic diversity and efficiency as well as an enhanced resistance to environmental stress, antimicrobial agents, and the host's defenses. (3-4) Biofilms organize into complex spatial patterns at the macroscopic and microscopic level that evolve over the course of its lifecycle, as depicted in Figure 1. For example, some constituent cells are active in spreading the biofilm while others enter dormant states invulnerable to antimicrobials based on metabolic or reproductive pathways. (5-8) The macroscopic physical properties of biofilms are reported to also protect constituent cells, resisting conventional liquid and vapor-phase treatments, as discussed in Section 2d. (9) Hence antimicrobial treatment is diminishingly effective only hours after bacteria first encounter a surface, or by stage 3 in Figure 1.

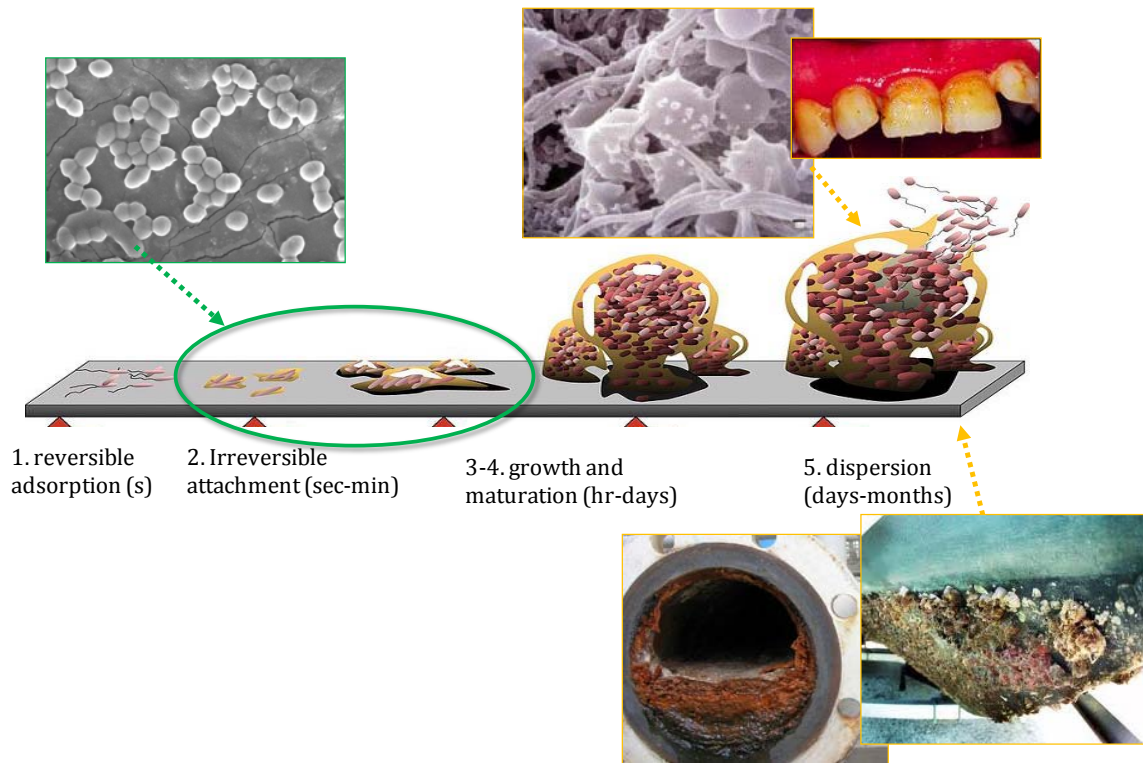


Figure 1. Biofilm lifecycle and exemplary health and economic impacts of biofilms. The lifecycle timeline depicts the general progression, in which (1) individual cells explore and reversibly adsorb to the surface; (2) extracellular matrix (ECM) is produced and the cells irreversibly attach to the target surface; (3 & 4) biofilm architecture develops and matures; (5) motile cells are released from the biofilm under conditions such as nutrient depletion. By the point of maturity, biofilm contamination can result in plaque and oral infection (top), pipe clogging (bottom), and the first stage of ship hull fouling (bottom right).

## B. Impacts: economic/industrial damage and mortality/health context

Biofilms contaminate a wide variety of infrastructure, such as plumbing, oil refineries, paper mills, heat exchangers, medical implants, and building HVAC systems.

(10) Marine fouling, which is precipitated by the accumulation of bacterial and other

microorganismal biofilm on ship hulls followed by progressively larger marine organisms, increases the fuel expenditure of seafaring vessels by up to 40%. (11) And in medical settings, biofilms are the cause of persistent infections ranging from urinary tract to middle ear, and from contact lenses and catheters to prostheses and heart valves, as well as causing dental plaque and gingivitis in the oral cavity. Biofilms trigger immune response, release of harmful toxins, and can physically obstruct indwelling catheters. As a result, hospital-acquired (or nosocomial) infections affect about 10% of patients in the United States, accounting for nearly 100,000 deaths annually. Moreover, biofilms have been estimated by the National Institutes of Health to cause 80% or more of all microbial infections in humans. (12-14) The combined economic impact of biofilms in the United States alone has been estimated to be between several billion dollars to greater than 100 billion dollars annually. (15)

### **C. Limitations of conventional antimicrobial surfaces and treatments**

A wide range of bacterial resistant surfaces have been proposed to inhibit biofilm growth a priori and to *prevent* adverse effects, but the typical strategies rely either on a release of biocidal compounds or on inhibiting adhesion. In the first case, traditional techniques involve the design of coatings that release agents such as antibiotics, quaternary ammonium salts, and silver ions into the surrounding aqueous environment. Such agents have been incorporated into a variety of engineering polymers and other materials. (16) The latter approach has focused on the use of surface chemical functional groups that prevent protein and other adsorption as a means to inhibit bacterial adhesion. Current examples of the latter approach involve: [1] the use of low-surface-energy,



weakly polarizable materials (e.g., Teflon) to minimize the van der Waals interactions for adhesion of biological species (e.g., Tokay gecko) (17); [2] the use of hydrophilic polymeric materials, such as poly(ethylene glycol) (PEG), which form highly hydrated surfaces to potentially prevent protein and bacteria adhesion (18); [3] the use of zwitterionic mixed-charge materials (19) or amphiphilic materials (20) that utilize surface inhomogeneities (i.e., charge or hydrophobicity) to resist adhesion of biofilms at the nano- to micrometer scales (21); or [4] the use of micro/nanoscale topographical materials to geometrically reduce attachment of biofouling organisms in a narrow length scale range. (22)

While some of these reported anti-fouling materials are able to transiently resist particular examples of biofouling adhesion, none is capable of broad spectrum or long-term attachment resistance. A fundamental reason is that all of these state-of-the-art anti-biofouling surfaces exist in static forms, i.e., the surface is static or quasi-static in nature. Permanent interactions between the surfaces and biofilm-forming bacteria can eventually be established depending on the time scales of the adhesion processes. Materials that persistently resist bacteria are difficult to achieve by surface chemistry alone. Even if bacteria are unable to attach directly to a substrate, nonspecific adsorption of proteins and surfactants secreted by bacteria to the surface eventually masks the underlying chemical functionality. (23-25) *P. aeruginosa* forms indistinguishably robust biofilm after 24 hours of growth on a polymer surface regardless of the surface functionality, wetting properties, and charge, as seen in Figure 2, indicating its indifference to surface chemistry alone. Over a longer timescale, a reservoir of leaching antimicrobial compounds is normally finite and subject to depletion. Also, the emergence of antibiotic- and silver-resistant

pathogenic strains, along with new restrictions on the use of biocide-releasing coatings in the marine environment, have necessitated the development of new strategies (26-28)

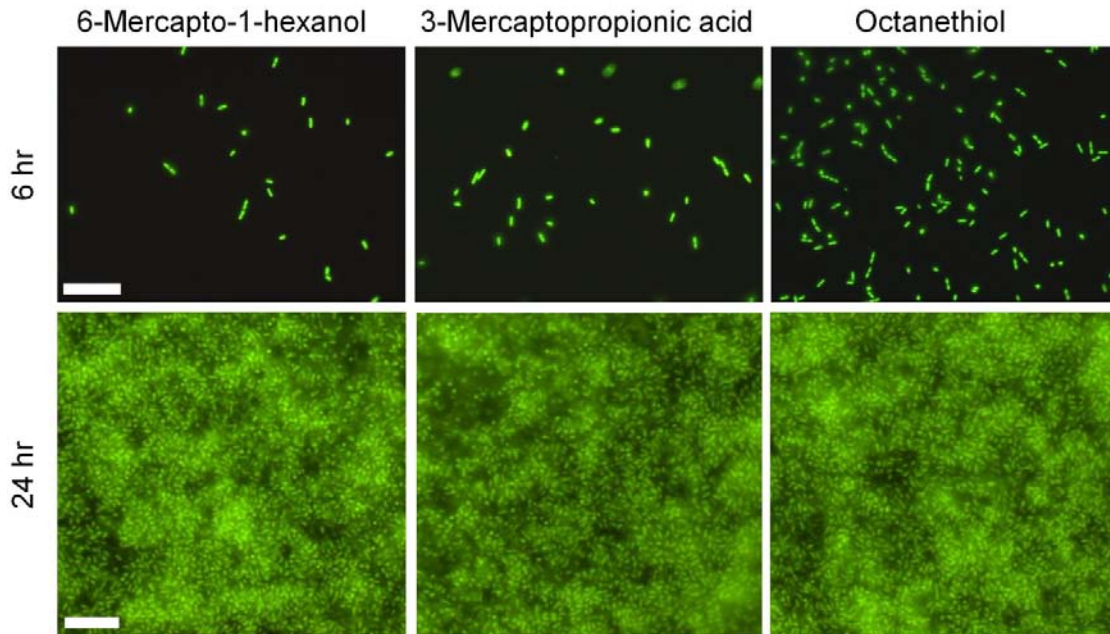


Figure 2. Fluorescence images of *P. aeruginosa* bacterial growth on epoxy (UVO-114) flat substrates functionalized with hydrophobic/hydrophilic and variously charged surface chemistries. Surface chemistry treatments show only transient effects on biofilm growth. They may influence initial attachment, e.g., at 6 hours, but become irrelevant by longer time scales of interest. Scale bars are 10  $\mu\text{m}$ .

Even more commonly employed than “antimicrobial” surfaces are the many varieties of antimicrobial treatments. These have become extensively used to combat biofilm contamination in health care, agriculture and industrial settings, and increasingly by the general public as well. (29) Commercial products employ a wide variety of active chemical agents, or biocides, often delivered in liquid form and sometimes as vapor. Indeed, one review of antiseptics and disinfectants identifies twelve classes of liquid

agents and five common types of vapor-phase sterilants. (29) Most of these biocides act on multiple intracellular targets. For example, chlorhexidine congeals the cytoplasm and disrupts the inner membrane; formaldehyde cross-links macromolecules such as DNA; and peroxygens oxidize the thiol groups in enzymes and proteins. Other liquids, such as ethanol, among the most universal of antiseptics and disinfectants, need only access the cell membrane, as the mode of action is believed to be membrane damage and protein denaturation. Common vapor-phase biocides include ethylene oxide and formaldehyde, both broad-spectrum alkylating agents that attack proteins and other organic compounds. (29)

Regardless of the particular chemistry or mechanism, the biocide must be able to reach the target cell to cause damage. At the multicellular level, therefore, effective biocide must penetrate into the extracellular matrix (ECM)—the slime-like “cement” of biofilm. Biofilms, however, offer their member cells several benefits, in particular, protection from environmental threats. It has been reported that ECM acts as a diffusion barrier and as a charged binding filter for certain antibiotics, (30) and that it complements enzymes and multidrug resistance pumps on cells that remove antimicrobials. (31-32) The ECM composition varies widely among species, but in general its major components are exopolysaccharides and proteins. (33) The resistance to threats covers a wide range of treatments: biofilms exposed to chlorine bleach for 60 minutes are reported to still have live cells (12); biofilms in pipes continuously flushed over seven days with multiple biocides re-colonize the pipes (34), and biofilms have been reported to survive in bottled iodine solution for up to 15 months (35). Yet the remarkable robustness of biofilms

against a broad range of antimicrobials, which differ entirely in chemistry and mechanism, remains a puzzle, despite two decades of biofilm research.

Biofilms protect their constituent cells in various ways, which makes both industrial and clinical contamination difficult and costly to treat. As self-organized communities, biofilms have evolved differentiated cell phenotypes performing complementary functions. The associated cooperative behavior of bacterial cells, mediated by cell-cell communication and other factors, enables an increased metabolic diversity and efficiency as well as an enhanced resistance to environmental stresses, antimicrobial agents, and immune response. For example, some constituent cells are active in spreading the biofilm while others enter dormant states invulnerable to many antimicrobials. (5-8) The macroscopic physical properties of biofilms, in which cells are bound together by protein and exopolysaccharide matrix, also protect them by resisting penetration of conventional liquid and vapor-phase antimicrobials. (9)

Clearly, it is advantageous to prevent rather than treat biofilm formation. Indeed, a wide range of bacteria-resistant surfaces have been proposed, but most strategies rely either on a release of biocidal compounds or on inhibiting adhesion. (16, 36-38) In the first case, traditional techniques involve the design of coatings or bulk materials that release agents such as antibiotics, quaternary ammonium salts, or silver ions into the surrounding aqueous environment. (16) Such agents have been incorporated into a variety of engineering polymers and other materials. The latter approach has focused on the use of surface chemical functional groups such as poly(ethylene glycol) that inhibit protein adsorption as a means to inhibit bacterial adhesion. (39-40)

Both of these strategies, however, are generally transient. Surface molecules are subject to desorption over time, but even if no desorption occurs and bacteria are unable to attach directly to a substrate, nonspecific adsorption of proteins and bio-surfactants can still mask the underlying chemical functionality. (24, 41-42) Additionally, any defects or voids in the surface chemistry could serve as nucleation sites for bacterial attachment. Strategies involving leaching of biocides are limited over a longer timescale since their reservoir is finite and subject to depletion. (38) Also, the emergence of antibiotic- and silver-resistant pathogenic strains, along with new environmental restrictions on the use of biocide-releasing marine coatings, has necessitated the development of new strategies. (26-27)

#### **D. Biofilm nonwettability as challenge and motivation**

We report herein a striking phenomenon that we believe may be a critical property responsible for biofilm integrity and biocide resistance. The surfaces of *Bacillus subtilis* biofilms are strongly liquid repellent - nonwetting - against a broad range of solvents and commercial biocides. Similar to water that is repelled by the lotus leaf (43), these liquids do not spread on and into the biofilm surface. However, while the lotus leaf is merely hydrophobic, i.e. it repels water but is quickly wetted by liquids of lower surface tension\*, *B. subtilis* biofilms resist even ethanol concentrations on the order of 80%. Additionally, we report that the biofilm can effectively resist penetration by applied vapors, even following prolonged exposure. These results reveal the need to understand the bulk phase, macroscopic aspects of biocide interaction with the biofilm

---

\* We refer to the surface tension of a liquid-air interface as the “surface tension of the liquid”.

surface in addition to the molecular interactions with the matrix interior and cells, where biocides ultimately act. Critical limitations may not be recognized if the resistance is not first addressed at the level of liquid wettability and effective biocide access to the biofilm interior.

## I. Liquid resistance—including ethanol and common disinfectants<sup>1</sup>

### 1. Contact angle goniometry and confocal microscope visualization

*Bacillus subtilis* is a ubiquitous bacterium commonly recovered from water, soil, air, and decomposing plant residue that is widely adopted as a model organism for laboratory studies (44). Populations of *B. subtilis* form robust centimeter-scale biofilms both on solid surfaces (colonies) and on liquid surfaces (pellicles) (45), and these biofilms display a characteristic wrinkled morphology, shown in Figure 3. The large area of each biofilm allows us to characterize its wetting properties by measuring the contact angle for a series of liquids that span a broad range of liquid surface tensions. The contact angle of a liquid on a solid surface is the angle formed at the droplet edge between the solid-air and liquid-air interfaces (see schematic in Figure 3). Liquids of high surface tension are repelled by the surface so that the droplet remains almost spherical with the contact angle of  $>90^\circ$ . In contrast, low surface tension liquids tend to spread on the surface, so that they meet the surface at a very small angle. Therefore, contact angles serve as a quantitative measure of wettability. Figure 3 shows the contact angles of water and mixed water-ethanol droplets, with ethanol concentrations ranging from 0% to 100%, applied to wild type *B. subtilis* biofilms. The contact angle remains nearly constant at  $\sim 135\text{-}145^\circ$  in the concentration range from pure deionized water to about 80% ethanol. The contact angle then sharply drops to about  $70^\circ$  at 90% ethanol. This wide repellency

---

<sup>1</sup> These results are published in *Proceedings of the National Academy of Sciences* [doi 10.1073/pnas.1011033108].

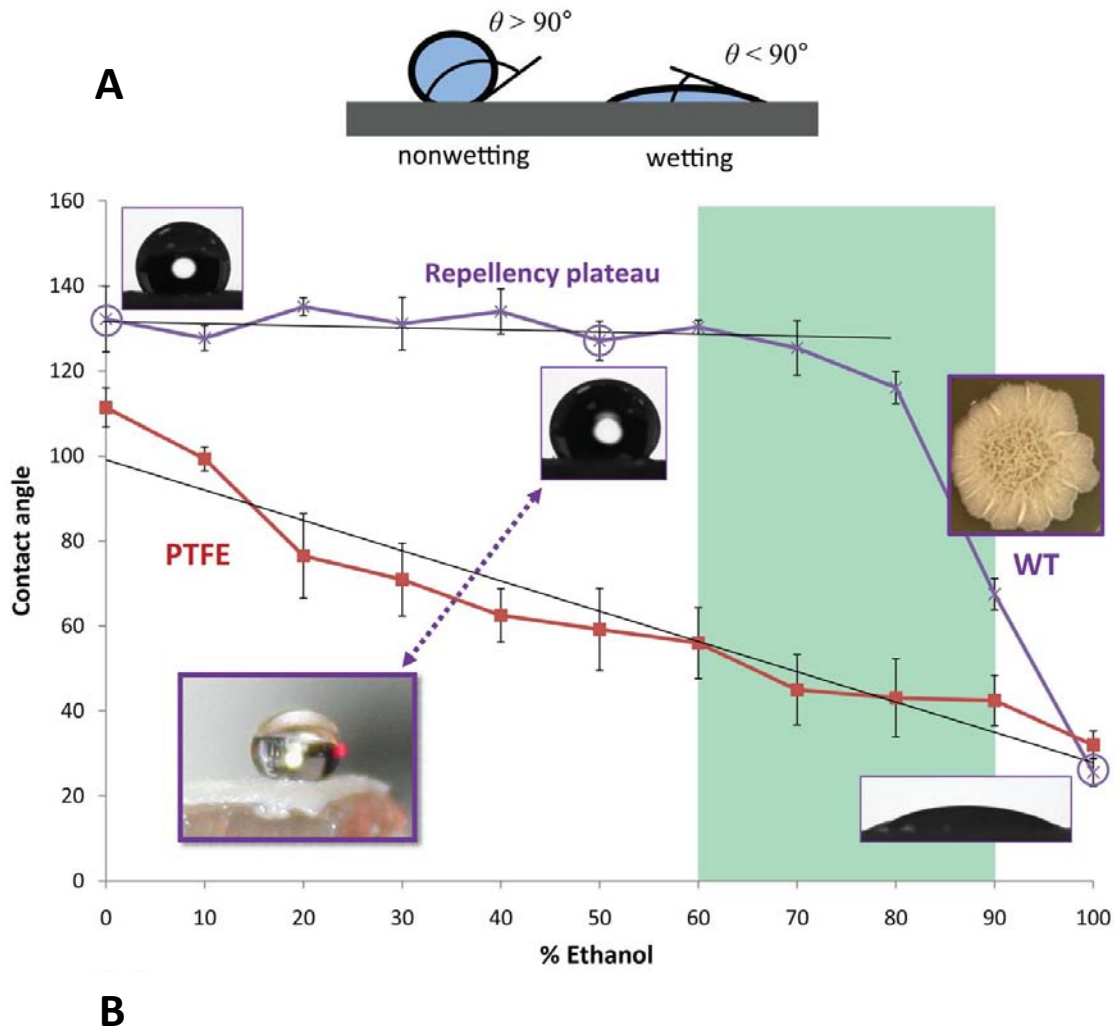


Figure 3. Bacterial biofilm wetting characterization by contact angle analysis. (a) Schematic of the contact angle  $\theta$ : low (high) surface tension liquids generally wet (do not wet) surfaces and have small (large) contact angles. (b) Contact angle of water droplets on a wild type (WT) *B. subtilis* biofilm and a polytetrafluoroethylene (PTFE or Teflon) block as a function of ethanol concentration. A plateau of  $\sim 135$ - $145^\circ$  is seen for the biofilm up to  $\sim 80\%$  ethanol, when it transitions to wetting. In contrast, Teflon displays a roughly linear decrease in contact angle. Liquid drop profiles used for determining the contact angle are inset for wild type biofilm at 0, 50, and 100% ethanol; also inset is a photograph showing the repellency phenomenon for a drop of 50% ethanol on biofilm. Antimicrobial activity of alcohols is believed to be optimal in the 60 to 90% range, denoted as the green region, where the biofilm is largely nonwetting, suggesting that



Figure 3 (Continued)

ethanol-based bactericides may not wick into the biofilm. Error bars are s.d.,  $n = 7$ . Inset photographs show the architecture of the wild type biofilm (right) and a nonwetting droplet of 50% ethanol on the biofilm surface (left).

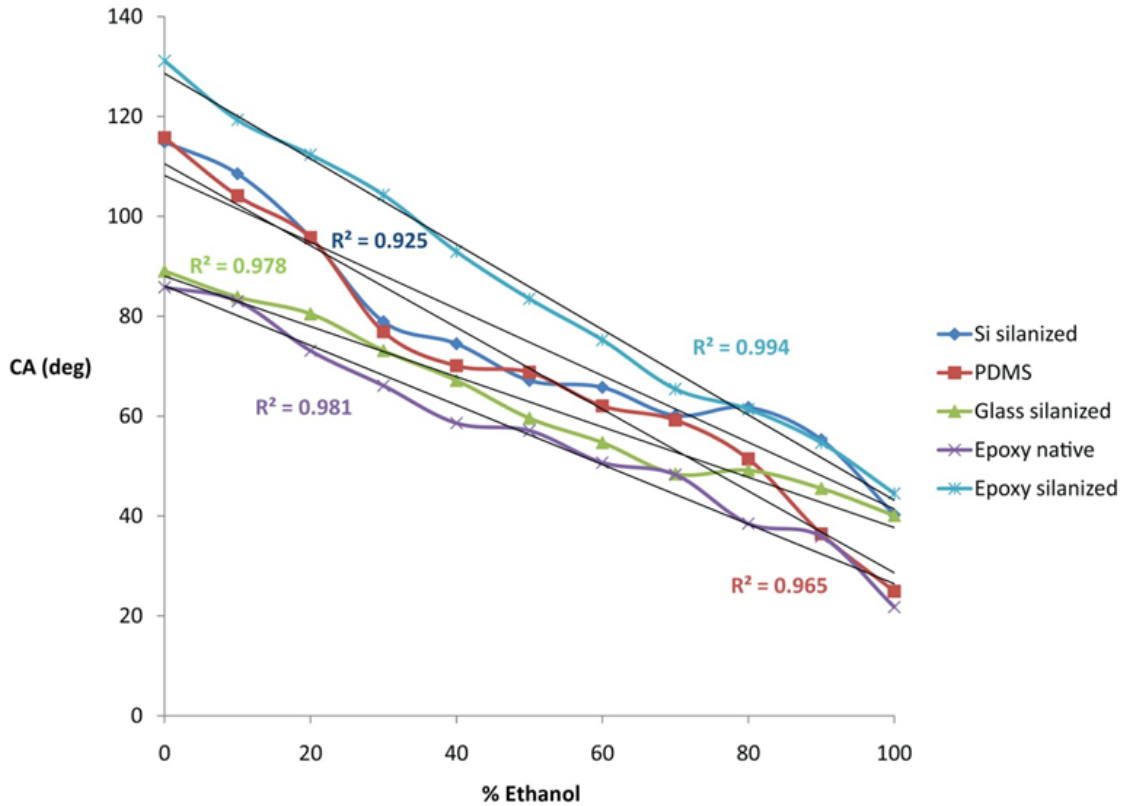


Figure 4. The linearly decreasing trend of contact angle as a function of increasing ethanol concentration observed in a range of hydrophobic materials, in addition to polytetrafluoroethylene (PTFE, or Teflon). Linear fits with  $R^2$  values are shown for each material.

plateau is in stark contrast to the typical wetting behavior of hydrophobic materials such as polytetrafluoroethylene (PTFE, or Teflon), which show a pseudo-linear decrease of contact angle with increasing ethanol concentration and are wetted at ethanol

concentrations as low as 20% (Figure 4). We also observe a similar repellency plateau in *B. subtilis* pellicles—floating biofilms that grow at liquid-air interfaces

High contact angle values indicate that it is energetically unfavorable for the liquid to spread and wick into the textured biofilm surface. Indeed, a rhodamine-stained puddle applied to the biofilm accesses the ECM only partially, leaving extensive areas that are not wetted by the liquid and the vast number of bacterial cells unaffected (Figure 5).

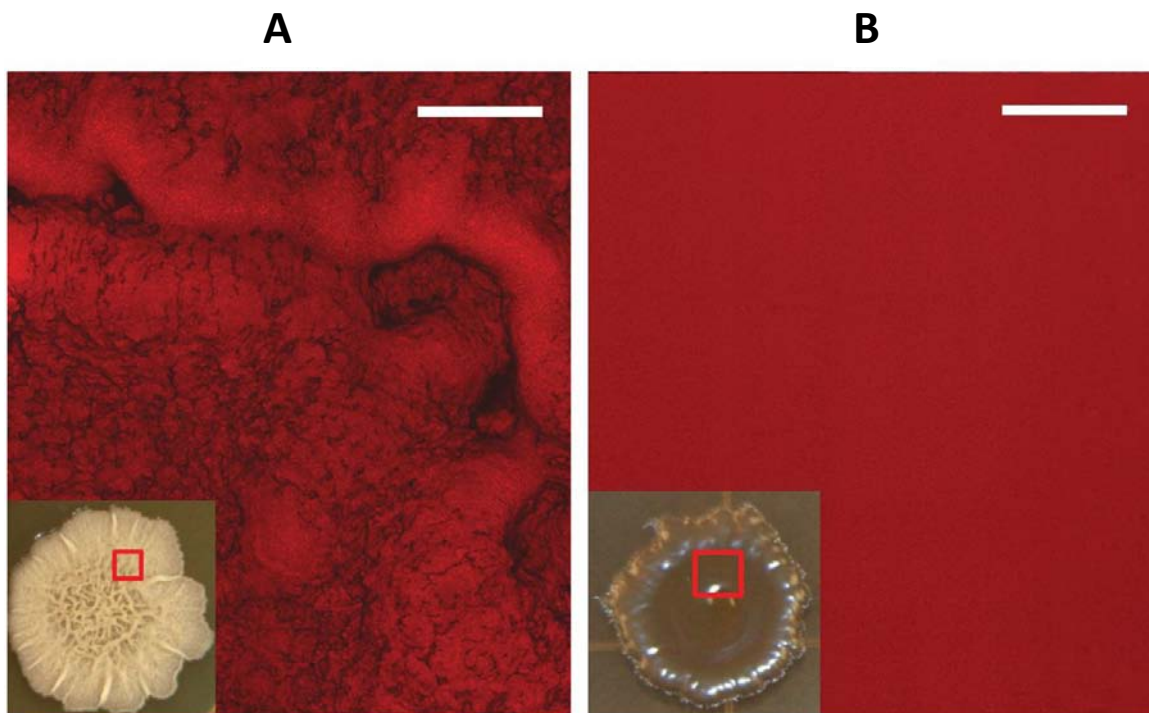


Figure 5. Fluorescent confocal z-stack showing 3D rhodamine staining of *B. subtilis* colony integrated through the thickness of the film. (a) Failure of liquid to access wild type colony. Areas that are stained red correspond to regions that were wetted by the puddle—the liquid footprint—and penetration is only partial. Black, unstained regions correspond to trapped air. (b) Uniform fluorescent staining of *epsH* colony indicates complete, uniform wetting of the entire mutant biofilm by liquid. Scale bars are 250  $\mu\text{m}$ .

## 2. Scope of wetting resistance to antimicrobials

It is important to note that the biofilm surface is nonwetting for much of the alcohol concentration range of 60% to 90% (highlighted by the green rectangle in Figure 3), which is commonly thought optimal for antimicrobial activity based on studies of free-swimming bacteria (29). The plateau observed in the biofilm contact angle curve extends well into the 60-90% range, indicating that even these supposedly lethal concentrations would not wick into the biofilm structure. The antimicrobial activity of alcohols and other solvents is therefore compromised by the strongly nonwetting behavior at clinically relevant concentrations. Furthermore, the nonwetting phenomenon also compromises penetration of other frequently used solvents (Table 1) and commercial biocides (Table 2). While commercial bleach moderately wets the biofilm, Lysol® disinfectant solution, whose active ingredient is 60% ethanol, remains highly nonwetting at 120-130°; and Hibiclens preoperative antiseptic (4% chlorhexidine gluconate, 4% isopropanol, and water) similarly fails to wet the biofilm.

Table 1. Contact angles of aqueous solutions of organic solvents on *B. subtilis* biofilms

	WT	epsH	tasA	sinR
50% Ethanol	139.0 ± 3.9	10.2 ± 2.2	119.7 ± 10.3	128.9 ± 6.3
50% Isopropanol	125.3 ± 2.6	11 ± 1.5	110.9 ± 6.6	112.6 ± 2.1
50% Methanol	137.9 ± 4.0	8.4 ± 1.1	119.3 ± 8.3	115 ± 7.2
50% Acetone	139.7 ± 3.5	7.7 ± 3.0	117.2 ± 9.8	119.8 ± 3.6

Error = standard deviation;  $n = 7$  for WT, 8+ for tasA, 8+ for epsH, 12+ for sinR

WT = wild type; epsH = exopolysaccharide deficient; tasA = matrix protein deficient; sinR = protein and exopolysaccharide overexpressed

Table 2. Commercial biocides on *B. subtilis* wild type biofilms

Test liquid	Contact angle (°)
Clorox bleach	45.9 ± 9.4
Lysol Professional	121.9 ± 6.3
Hibiclens	130.8 ± 10.2
Drain opener (10 sec)	123.0 ± 13.7
Drain opener (5 min)	47.0 ± 0.52

Error = standard deviation;  $n = 9$

### 3. Stability of the biofilm's nonwetting function

Having established the ultra repellency of *B. subtilis* biofilm, we studied the persistence of this phenomenon. Biofilm aging appears to have no effect, i.e., there is no significant reduction in contact angle as the biofilm ages from three days to two weeks. With respect to droplet time and volume on the biofilm surface, the contact angle evolution is also remarkably invariant; the contact angle is identical for a given droplet size of any nonwetting solvent concentration and thus any surface tension (Figure 6). A

deviation only appears at 80% ethanol; hence any lower concentration should similarly fail to penetrate into the biofilm. We further observed nonwetting persistence with repeated application of liquids, which indicates no significant surface degradation. Only exposure to 90% or higher ethanol renders the biofilm wettable by any subsequent concentrations, evidently having altered its surface properties. Whether with regard to biofilm age, time of liquid exposure, or repeated liquid contact, biofilm liquid repellency appears to be a highly persistent phenomenon.

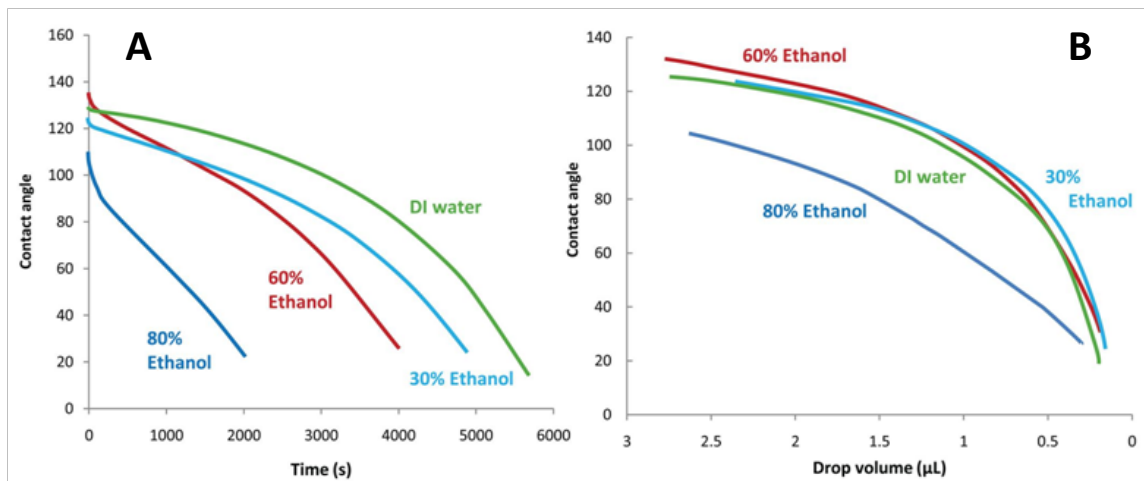


Figure 6. Persistent biofilm nonwettability is invariable with respect to ethanol concentration across the repellent concentration range. Drops of four ethanol-water concentrations were tracked for contact angle during evaporation on the surfaces of wild type *B. subtilis* colonies. (a) Evaporation contact angles decay faster in time for higher ethanol concentrations. This is expected due to ethanol’s high vapor pressure and due to some contact line pinning, or sticking of the droplet edge to surface heterogeneities (46). (b) The evaporation contact angle as a function of drop volume, however, traces the same curve for deionized water, 30%, and 60% ethanol, in spite of dramatic surface tension decrease, and only shows large deviation at the 80% grade—roughly the threshold concentration between nonwetting and wetting behavior.

#### 4. Genetic mutants and biochemical factors

To identify the underlying biochemical and physical features of the biofilm that might be responsible for this behavior, we performed a similar analysis for *B. subtilis* mutants that lack or over-express primary ECM components. Along with the wild type biofilm, we prepared three mutants: exopolysaccharide-deficient (*epsH*), matrix protein-deficient (*tasA*), and overproduced exopolysaccharide and protein (*sinR*). (47) Each of the phenotypes is shown in Figure 7. The *epsH* biofilms are completely wetted by ethanol at any concentration, and even by pure water. Consequently, exposure of the *epsH* mutant to a rhodamine-labeled liquid results in a uniform fluorescent signal, confirming complete penetration of the rhodamine solution into the biofilm (Figure 5). While the *epsH* biofilms are also wetted by 50% solutions of other low-surface-tension liquids, such as methanol, isopropanol, or acetone, the *tasA* biofilms show moderate repellency, with a contact angle of  $\sim 110\text{-}120^\circ$  for these liquids (Table 1). Hence, the exopolysaccharide plays a primary critical role in biofilm repellency, while the *tasA* protein appears to play a secondary, indirect role, although the fact that neither the matrix protein nor the polysaccharides individually preserve biofilm repellency shows that both of these biomolecules are required for full resistance. In contrast to the *epsH* and *tasA* mutants, *sinR* biofilms with overexpressed polysaccharide and protein components show persistent liquid repellency, only slightly inferior to that of the wild type (see Figure 7). The corresponding wild type and matrix-mutant pellicles exhibit the same qualitative wetting behaviors as colonies.

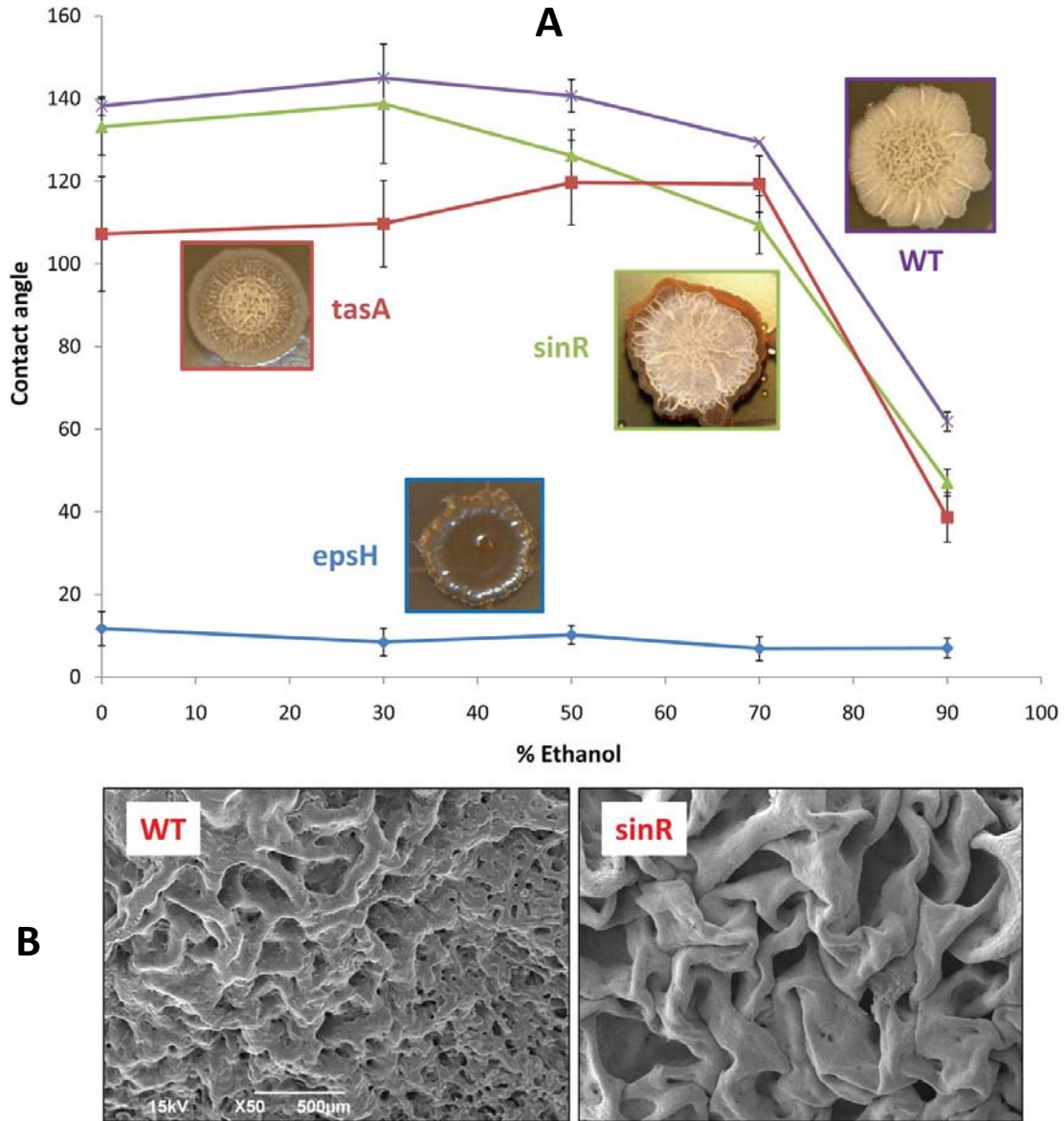


Figure 7. Characterization of liquid repellency mechanisms using genetic mutants of *B. subtilis* biofilms lacking either the carbohydrate-rich exopolysaccharides (*epsH*) or the bulk protein in the extracellular matrix (*tasA*), or overproducing both components (*sinR*). (a) The phenotypes are inset adjacent to their respective contact angle curves. Highly wrinkled *sinR* biofilm, with excess *tasA* protein and *epsH*, exhibits slightly decreased repellency relative to wild type, possibly related to suboptimal topography. Error bars are s.d.,  $n = 7$  for wild type (WT) and Teflon,  $n = 8+$  for *tasA*,  $8+$  for *epsH*, and  $12+$  for *sinR*. A standard Wilcoxon two-sided test was performed to test statistical significance in

Figure 7 (Continued)

contact angle differences (1% and 5% significance level). The contact angle for epsH is statistically different from any other strain; WT is statistically different from tasA at all ethanol concentrations, and from sinR at ethanol concentrations  $\geq 50\%$ ; tasA and sinR are statistically different except at 50% and 90% ethanol concentration (and 70% at significance level 1%). (b) Scanning electron microscope (SEM) images showing the surface features of the critical point dried wild type (WT) biofilm (left) and the sinR mutant (right).

## 5. Decoupling surface topography and chemistry

We note that in addition to the chemical contribution of surface molecules, the wetting properties of materials are known to be modified by complex surface microstructure. (48-49) In particular, wild type biofilm's micro- and nanoscale features with highly reentrant curvatures (Figure 8) may be as important for this wetting resistance at lower surface tensions. (50) Indeed, the epsH and tasA mutants lack the wrinkled architecture of the wild type, while the sinR mutant slightly overexpresses the larger scale wrinkled topography (47) but appears smoother than the wild type at the 10-100  $\mu\text{m}$  scale (Figure 8 and Figure 9). To clarify the potential role of the biofilm microstructure, we replicated the biofilm in epoxy resin (51), and verified by scanning electron microscopy (SEM) that the topography of the polymeric replicas reproduced the complex features of the biofilm at the micron level (Figure 9). (52) Creating a geometric replica allows the topography and surface chemistry to be decoupled, as the surface chemistry can then be separately modified. We fabricated a series of epoxy biofilm replicas as well as flat epoxy surfaces, each with and without hydrophobic coating, and



compared the contact angle as a function of ethanol concentration (Figure 8). For a pure water droplet, the microtopography of the unmodified wild type replicas alone renders the surfaces moderately hydrophobic, with a contact angle of  $\sim 115^\circ$ , while the same flat surface is mildly hydrophilic (contact angle  $\sim 85^\circ$ ). Moreover, fluorinated wild type replicas, which combine native microtopography with hydrophobic surface chemistry, reproduce the  $\sim 135^\circ$  hydrophobicity level of the native biofilm. Droplets containing ethanol, however, do not follow this behavior: none of the replicas reproduce the nonwetting plateau typical of the live biofilm. In particular, all of the replicas—including those with both the wild type topography and hydrophobic coating—undergo a pseudo-linear drop in contact angle with increasing ethanol concentration (Figure 8), similar to Teflon. These results suggest that both the topographic and surface chemistry features of the extracellular matrix work together to give the biofilm its highly nonwetting behavior toward water, but that topography and simple hydrophobic chemistry cannot completely account for the observed extreme repellency of the biofilm surface toward low surface tension liquids.

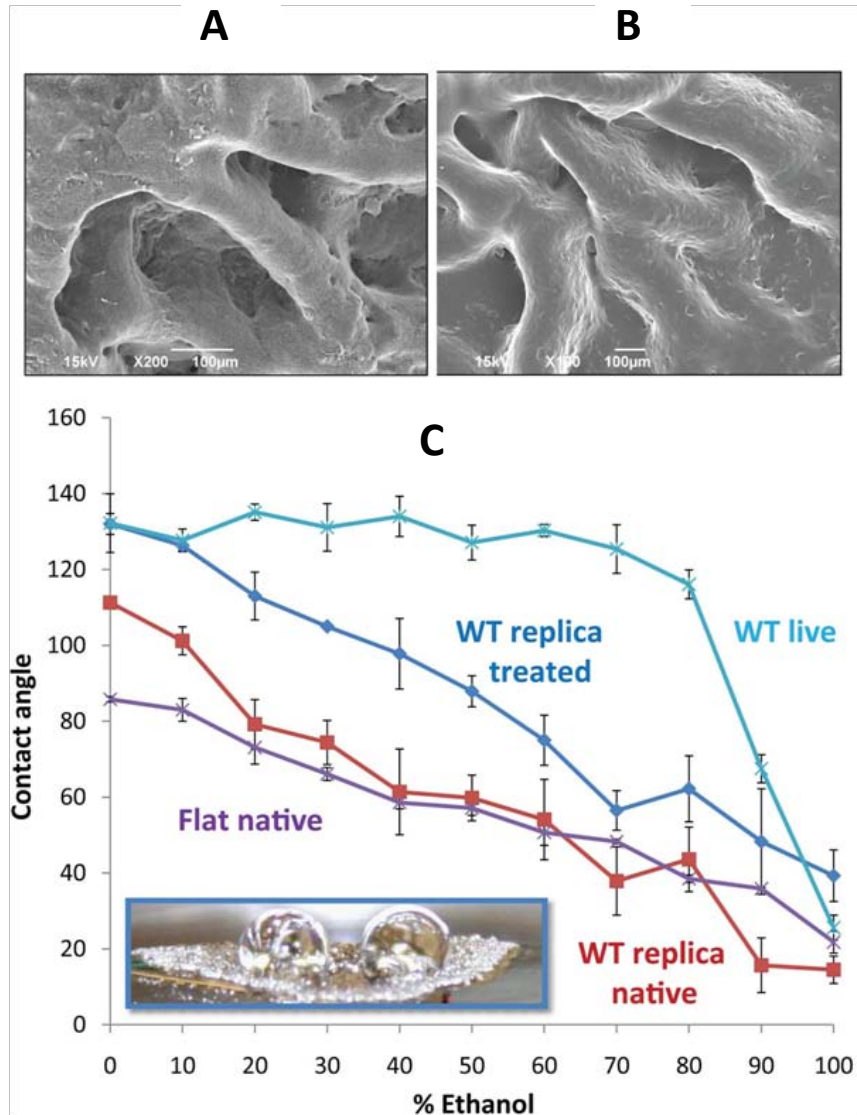


Figure 8. Testing role of topography using functionalized polymeric replicas of biofilm microstructure. (a) Scanning electron microscope (SEM) image showing the surface features of the critical point dried live wild type (WT) biofilm; (b) SEM image showing the surface features of the UV-cured epoxy replica of the wild type biofilm. Microscale topography is reproduced well, although dehydration artifacts may occur in the critical point dried sample. (c) Contact angle of a live wild type colony, a native (uncoated) epoxy replica fabricated by adapting soft lithography (51), a fluorinated replica, and a native (uncoated) flat epoxy substrate. Inset shows an epoxy biofilm replica with applied drops of 30% ethanol. Error bars are s.d.,  $n = 7$ .

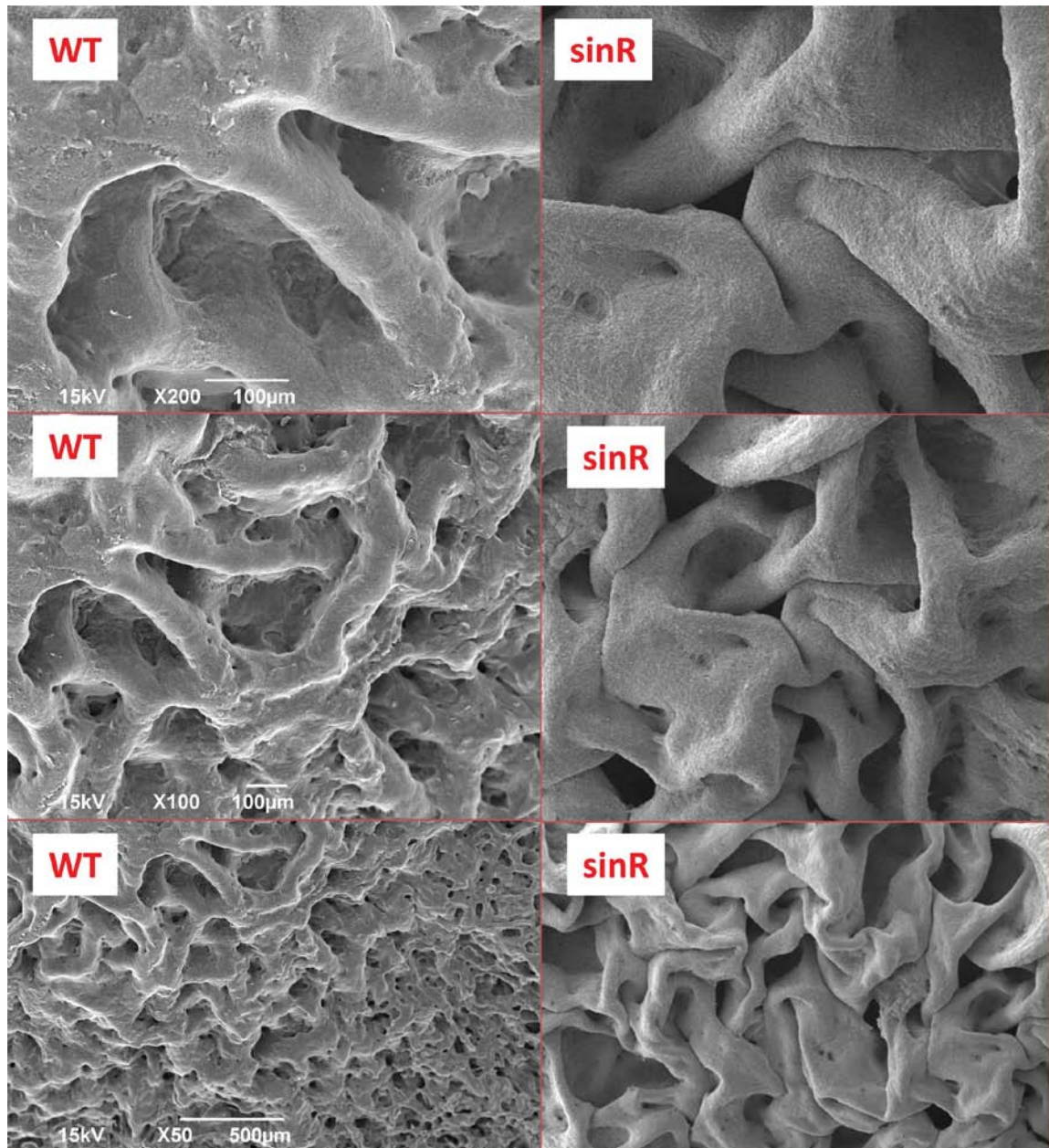


Figure 9. Comparison of the WT and sinR mutant morphologies at corresponding magnifications via SEM. The sinR mutant, which overproduces matrix protein and exopolysaccharides, is seen to slightly overexpress the larger scale wrinkled topography but appears smoother than the wild type at the 10-100 µm scale.

## II. Vapor resistance—synchrotron microCT

In addition to liquids, many environmental threats to bacterial biofilms, and indeed, quite a number of antimicrobials reported over the last five decades (53-56), are presented to the surface in vapor phase. Therefore we also investigated surface gas penetration of wild type as well as matrix-altered *B. subtilis* biofilms. To assess how readily a gas penetrates into the biofilm, we prepared the biofilm (as described in Materials and Methods) and exposed it to a test vapor that deposited a radiation contrast agent wherever it could access on or in the sample, therefore revealing the extent of penetration upon X-ray imaging (vapor was presented by Atomic Layer Deposition as described in Materials and Methods). We imaged the biofilm using synchrotron-generated X-rays and micro computed tomography (see Materials and Methods): regions of high intensity within the biofilm indicate where the gas has penetrated and alumina has been deposited. In all the wild type samples, the images show a sharp gradient of intensity close to the surface as shown in Figure 10a: the gas penetrates only about 10  $\mu\text{m}$  below the surface. However, penetration is markedly deeper in the *tasA* and *epsH* mutants, as shown by the much thicker bright region in Figure 10bc. Thus, as for liquid repellency, biofilm gas impenetrability also requires both the protein and the polysaccharide matrix components.

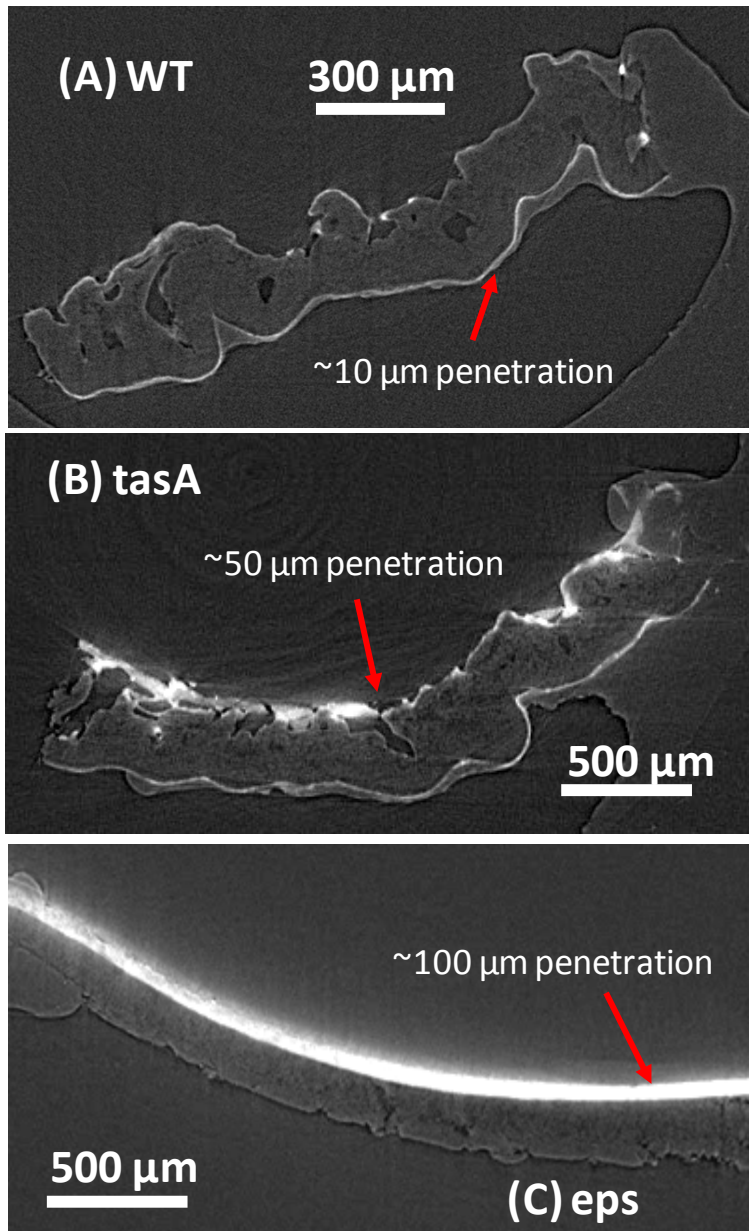


Figure 10. Synchrotron micro-CT reconstructed images of the (a) wild type (WT), (b) *tasA* mutant, and (c) *epsH* mutant of *B. subtilis* biofilms following atomic layer deposition (ALD) of heavy metal oxides by vapor exposure (see Materials and Methods). In the wild type biofilm, the vapor phase ALD precursors only penetrate a short distance. In *tasA* and particularly the *eps*-deficient colony, deep gas penetration was observed.

The presented data uncovers a new phenomenon and a new challenge: that *Bacillus subtilis* biofilm colonies and pellicles are extremely liquid and gas repellent, greatly surpassing the properties of known repellent surfaces such as Teflon and Lotus leaves. We demonstrate that the biofilm surface is persistently nonwetting against up to 80% ethanol as well as other organic solvents and commercial biocides. We show that the biofilm nonwetting properties arise from both the polysaccharide and protein components of the extracellular matrix, and are a synergistic result of surface chemistry, multi-scale surface roughness and reentrant topography. Moreover, we report the gas impenetrability of the biofilm surface, implying defense capability against vapor-phase antimicrobials as well.

Biofilms underlie a growing public threat in the form of nosocomial deaths, contaminated water, sick building syndrome (building occupant illness due to airborne contaminants), etc. To our knowledge the effort to control them has not considered the possibility that biocides might be resisted simply on account of being liquids or gases. While antiseptics and disinfectants have become ubiquitous, they are clearly not optimized for biofilms. Persistent biofilm nonwettability and gas impenetrability therefore represent significant obstacles against many of our most commonly used biocides: since liquids and gases cannot fully penetrate into the matrix, they cannot access all the subsurface cells and are largely ineffective. Our results reveal the need to study biocide resistance in terms of the macroscopic interaction with the biofilm surface in addition to the molecular-scale interactions with the matrix molecules and cells. Such insight could help address the longstanding question of how a broad range of antimicrobials that differ entirely in chemistry and mechanism can all fail. Our findings

further suggest that new delivery strategies may be severely compromised if they do not take into account the level of liquid wettability or gas penetration—to be effective against biofilms, antimicrobial delivery may well require a solvent or diluent specifically designed to penetrate into the biofilm surface. If surface properties are highly species-specific, approaching antimicrobial design from this perspective could also provide a way to selectively target particular biofilms.

*B. subtilis* biofilms grow in exposure to air, potentially extending our findings to biofilm communities in a wide range of environments, such as air ducts, sewers, liquid storage tanks, and porous soil media. These liquid repellency properties may in fact have evolved in response to *B. subtilis*'s natural environment, soil, where water leaches heavy metals, antibiotics, and other toxins. Interestingly, *B. subtilis* is now being used for crop protection against pathogenic bacteria and fungi in the soil, and an understanding that this plant protection might be a result of robust, protective biofilms colonizing and shielding the roots from water-borne pathogens has recently emerged. (57) Furthermore, the repellency phenomenon is general to both solid-associated colonies and liquid-associated pellicles.

Biofilms also exist in fully submerged environments, and because they grow in continuous contact with liquids, they may not present the same properties that we report here. However, biofilms that are primarily but not exclusively submerged, such as those only periodically exposed to flows, in pipes and tanks, may in fact exist at least partially in a nonwetting state. Our results may highlight the need to consider this possibility not only for direct delivery of liquid antimicrobials, but also for optimization of systems based on beneficial biofilms, such as bioremediation reactors.

The ability of *B. subtilis* biofilms to resist wetting may be considered particularly surprising in light of the fact that *B. subtilis* secretes surfactin (58-59), a biomolecule that enhances biofilm spreading by lowering the effective surface tension of liquids and that could similarly be expected to increase wetting. It has been shown that differences in surfactin concentration along the biofilm can produce surface tension gradients that are sufficient to pull *B. subtilis* pellicles upward on glass slides. However, although the gradients in surface tension may be large enough to pull the biofilm, the total reduction in surface tension due to surfactin production during pellicle growth is only about 10%. (58) Although the spatio-temporal location, transport and absorption of surfactin molecules have not been characterized, this suggests that the concentration of surfactin at the biofilm surface may be fairly small.

To our knowledge, the extreme liquid repellency of *B. subtilis* biofilm has not been reported for any natural material: numerous studies have analyzed the “lotus effect” of superhydrophobic plant leaves and insects, but none of these surfaces can resist wetting by both lower surface tension liquids and water. (60-63) Insights from the latter examples have been pivotal in the design of synthetic superhydrophobic surfaces, but the design of synthetic surfaces with broad-spectrum repellency, with no comparable model, has only recently been achieved and has yet to overcome a high degree of mechanical fragility and reliance on intensive fabrication and chemical derivatization. (46, 64) As a resilient, environmentally adaptive repellent surface composed of only nontoxic biomolecules, *B. subtilis* biofilm holds promise as a new model surface that can open new directions in anti-wetting applications. Beyond *B. subtilis*, biofilms have evolved as a survival strategy across a huge diversity of species and environments, based on equally



diverse matrix compositions and architectures; exploring whether and how repellent surface behaviors have emerged across the bacterial population could provide a rich, untapped source for understanding mechanisms and designing surfaces for liquid and gas repellency. In particular, further study of the surface features--potentially related to the dynamic nature of the live biofilm and its complex biomolecules--that synergize with the topographic and chemical features isolated by our experiments to confer resistance to low surface tension liquids may provide insight into the fundamental factors responsible for wetting behavior as well a basis for new biomimetic designs.

### **Experimental method details**

*Biofilm Preparation.* *Bacillus subtilis* NCIB 3610 (wild type), *epsH*, *tasA*, and *sinR* knockout mutant biofilm colonies were prepared as follows. Microcolonies of each *B. subtilis* strain were taken from streaked freezer plates and incubated in Luria broth (LB) cultures for 18 hours at 23° C. The cultures were drop cast (3  $\mu$ L per drop) on 10 cm diameter MSgg minimal medium agar plates and incubated for varying time periods at room temperature to grow colonies. (45) Surface pellicles were also grown in six-well plates by inoculating MSgg medium with the wild type and matrix-mutant *B. subtilis* in LB media.

*Contact Angle Measurement.* Static and time-domain contact angle measurements were performed on the biofilm colonies at various time points, on polymeric biofilm replicas, and on a Teflon block (McMaster-Carr) using a contact angle goniometer with screw-actuated syringe and accompanying software. 10% v/v increments of deionized water-ethanol solutions from 0% to 100% ethanol and 50% v/v aqueous solutions of methanol, isopropyl alcohol, and acetone, were prepared. Additionally, four commercial

biocides were obtained: Clorox bleach, Lysol Professional (liquid collected for drop-wise application), Hibiclens, and CVS drain cleaner. At least three contact angle measurements were collected per sample on untested areas outside the centre. Additionally, qualitative contact angle observations were made by repeatedly applying deionized water droplets on the same area of a colony to probe for repellency degradation, by applying ethanol-water mixtures to *B. subtilis* pellicles to compare to colony wetting behavior, and by applying phosphate-buffered saline droplets to colonies.

*Biofilm Replication.* Negative molds of 1 week old wild-type colonies were produced from polydimethylsiloxane (PDMS) (Dow Sylgard 184) with a prepolymer-to-curing agent ratio of 10:1. After extensive mixing of the prepolymer and curing agent, the mixture was degassed under vacuum to eliminate air bubbles. The PDMS mixture was then poured on the colony and underlying agar substrate, which was cut out by razor from the larger MSgg agar plate and placed in a small Petri dish. The PDMS mould thermally cured at room temperature for 24 hours. After curing, the agar was easily removed from the PDMS and the remaining biofilm “master” was fully dissolved during 15 minutes of sonication in a bath using a mixture of 1 part chlorine bleach, 1 part acetic acid, and 4 parts deionized water. The negative PDMS mould was also cleaned with ethanol, isopropanol, and acetone. To produce polymer replicas of the colony, the commercial UV-initiated one-part epoxy UVO-114 (Epoxy Technology) was chosen. Multiple epoxy replicas of the week-old WT colony were fabricated; also, multiple flat UVO-114 epoxy replicas of a glass slide were fabricated by the PDMS molding method. Half of the colony and glass slide replicas were left as native epoxy surfaces while half

were sputter-coated with 10 nm Pt/Pd and hydrophobized by perfluorodecanethiol in vapor phase deposition.

*Imaging.* Critical point drying of biofilm colonies for scanning electron microscopy (SEM) comparison to replicas was performed as follows. Samples of wild type, *tasA* mutant, and *epsH* mutant *B. subtilis* colonies were fixed in glutaraldehyde for 1 hour at multiples of 12 hours after drop casting 3  $\mu$ L of LB culture onto MSgg agar plates. After fixing, the samples were stepped through 10% grades of ethanol, given at least 30 minutes per step, and allowed to completely dehydrate overnight in absolute ethanol. They were then critical point dried on a Tousimis Auto Samdri 815 Series A. Imaging to compare the dried and epoxy replicated biofilm was performed on a Zeiss field emission Ultra55 SEM. To assay penetration of liquid into colony texture, rhodamine diluted 1:500 in DI water was placed dropwise on a *B. subtilis* WT and *epsH* colony until it formed a puddle; after waiting one minute, it was blown off by compressed air. Fluorescent microscopy z-stacks in a 6 x 6 tile pattern, covering a 1.2 x 1.2 mm total field of view and the depth range of fluorescent signal, were taken on a Leica TCS SP5 scanning laser confocal. The z-stacks were merged in Leica software and a maximum intensity merge was obtained with ImageJ.

*Micro-computed tomography.* Critical point dried samples of wild type, *tasA* mutant, and *epsH* mutant *B. subtilis* colonies were coated for one hour in a Cambridge NanoTech Savannah 200 Atomic Layer Deposition chamber sequentially with trimethylaluminum precursor gas which deposits alumina ( $\text{Al}_2\text{O}_3$ ) at 45 °C and hafnia ( $\text{HfO}_2$ ) at 65 °C. This was done in order to assess penetration of the precursor gasses while simultaneously providing x-ray radiation contrast. On site at the Argonne National

Lab, Advanced Photon Source, Station 13-BMD, the samples were carefully sectioned by razor and each mounted into a 2mm inner diameter hollow plastic tube. Each sample was mounted in a three-jaw chuck and imaged over a 360° rotation, with a beam energy of 40 kV. Radiographs of ~3 μm/pixel resolution were reconstructed into 3-D volumes using the IDL software package and analyzed. Parts of the biofilm that were less dense and more porous were more permeable to gas diffusion and hence to oxide deposition. Areas that had heavier oxide deposition absorbed more radiation, producing darker transmission images.

#### **E. Multifunctional HAR fibrous arrays in Nature provide biological inspiration for materials science solutions**

Biology is replete with examples of functional structures, whose properties are unmatched in today's man-made materials. Key features of biological structures are their dynamic nature, responsive behavior and often multi-functionality, which all comprise the goals for the next-generation smart artificial materials. There is a growing body of information describing natural structures with sophisticated design strategies that lend the organisms and plants superior mechanical, optical, adhesive, self-cleaning, actuation and sensing capabilities.(43, 65-72) Interestingly, the common feature of these largely unrelated designs is the use of fibers and high-aspect-ratio nano- and micro-structures. Nanostructures on the surface of the lotus leaf make the leaves superhydrophobic, and the droplets of water containing the collected insects and dust will roll off, and so maintain a clean leaf surface.(43) A gecko's feet are comprised of half a million setae fibers. Each seta is tipped with ~1000 nanometer-sized spatulae. This multi-scale fibrous assembly

offers a unique, reversible adhesion mechanism that holds geckos to surfaces in a self-cleaning fashion.(65-66) Complex, hierarchically-structured high-aspect-ratio silica fibers in the sponge Venus's Flower Basket provide amazing fiber-optical capabilities combined with superior mechanical properties.(67-68) Fish and amphibians have fibrous structures (cilia) on the surfaces of their bodies connected to a hair cell at their base that detect water flow.(69-70) Due to this sensing ability fish can swim in narrow caves—even without the possibility for eye sight—and sense other organisms moving in their vicinity.(69) Echinoderms cover their skin with high-aspect-ratio spines and mobile pedicellaria that provide an effective antifouling mechanism, preventing the settlement and growth of other organisms, by active movement.(71) Pedicellaria—small claw-like extensions on the aboral surface of starfish and sea urchins—essentially exist as dense arrays of environmentally responsive biological  $\mu$ -actuators.(71)

It has been a long-standing aspiration of bio-inspired materials science to understand the underlying construction principles of biological materials and to reproduce their unique features synthetically. We asked ourselves the question whether it is feasible to design a finely tunable, multifunctional, responsive nanostructured material that will show self-cleaning properties à la lotus leaf, will be capable of movement and reversible actuation à la echinoderm spines and pedicellaria and of sensing the force field à la fish skin. While nanostructured superhydrophobic surfaces inspired by the lotus flower and the adhesive properties of gecko feet have been mimicked with success, (73-75) actuation/sensing at the sub-micron scale is a challenging goal. Sensor arrays inspired by fish skin (76) are still lacking the key features related to their selectivity, tunable geometry and sensitivity. We have recently demonstrated that by using a

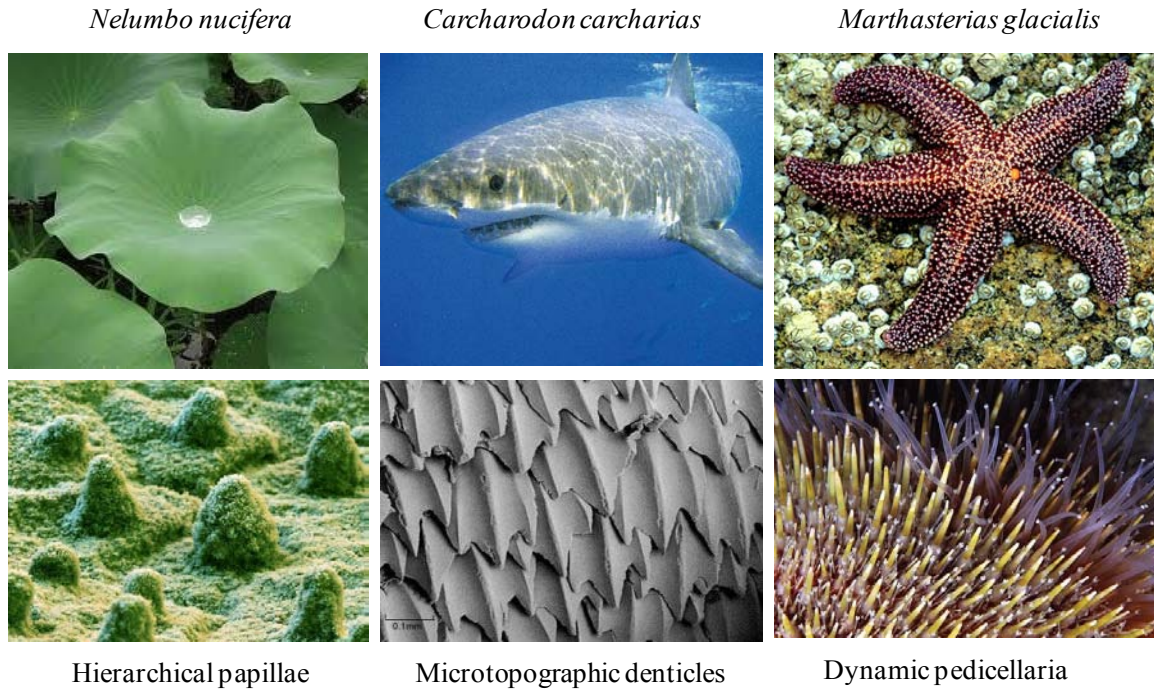


Figure 11. Bio-inspirations for functional surfaces that self-clean and prevent biofouling.

hydrogel muscle one can reversibly actuate Si nanostructures, which dynamically change their orientation in response to humidity, with a 60 ms response time.(77) While providing a successful example of a bio-inspired approach to controlled actuation at the nanoscale, this hybrid design had several structural limitations, including: (i) the nanostructures themselves were passive units and their movement was induced by a hydrogel that responded to one stimulus; (ii) the nanostructures were made of Si and, therefore, they had a fixed, high degree of stiffness that restricted the deflection and required high forces; and (iii) with no control over the stiffness, the extent of actuation was adjusted by using Si nanoarrays with various aspect ratios, which involved a highly expensive and labor-intensive deep-etching fabrication procedure for each substrate. In

the current study we wanted to take this bio-inspired design to the next level and use a truly “*materials*” approach to develop a low-cost procedure for producing an arbitrarily-designed actuated surface with high-aspect-ratio nanostructures that are themselves responsive to a variety of stimuli and have a finely-tuned geometry and stiffness.

In contrast, the persistent antifouling properties of a range of biological surfaces with active topographic features have been described. Nature provides some clues to preventing microbial colonization of surfaces by this alternative strategy. For example, while ship hulls constantly amass layers of algae and other microorganisms, materials with topographical features mimicking the skin of sharks have shown increased resistance to marine biofouling at certain length scales. (78) In this case, the shark is in constant motion, and the skin’s structures are static. Conversely, the skins of sedentary marine organisms known as echinoderms, e.g., star fish and sea urchins, are densely decorated with spiny, constantly moving microstructures known as pedicellaria that prevent larvae and microorganisms from attaching to the skin. (79-81) Such mechanical frustration of dynamic, physical structures may provide a more persistent and nontoxic form of inhibitive interaction between bacteria and surfaces. Indeed, bacterial cells are already known to respond to surface topography and mechanics, and their behavior can be manipulated using only spatial and mechanical cues. (82-84) Surface attachment is an integral step in biofilm formation that impacts chemical signaling pathways between and within bacterial cells. (85) Dynamic topographical features may influence the arrangement and the resulting behavior of cells on surfaces and affect biofilm development. (86) Yet, the strategy of mechanical frustration--and the role of topographic parameters with respect to surface motion parameters—has not been applied or studied in

a synthetic surface as a potential nontoxic solution for controlling bacterial biofilm attachment.



### 3. Fabrication of bioinspired structures and applications<sup>2</sup>

#### A. Benchtop soft lithographic double-casting method

Over the last several years, we have developed a comprehensive materials-based platform for the fabrication of bio-inspired surfaces and nanofibers whose assembly can be finely controlled. In contrast to conventional fabrication techniques such as photolithography and electron- beam lithography, our platform does not require use of a clean room and is easily performed on the benchtop. Many degrees of freedom—material, geometric, mechanical, dynamic—can be programmed starting from a single, simple master structure. And whereas conventional methods to produce regular arrays of surface-attached nanofibers are restricted to a very limited choice of materials and a highly sophisticated and expensive fabrication process, our approach enables application of a wide range of materials, including metals, polymers, and ceramics.

At its core, our fabrication platform adopts and significantly extends the soft lithography method originally pioneered by Whitesides, et al. (87) The soft lithography technique has been introduced recently as a low-cost alternative to conventional lithography and has been shown to be an extremely powerful method for the high-resolution replication of microfabricated substrates in an elastomeric polymer – polydimethylsiloxane (PDMS). (88-90) PDMS has been widely used to form polymeric arrays of micron-sized posts for a variety of applications, including control of cellular adhesion and wettability.(91-93) Due to the low level of stiffness of PDMS, only limited

---

<sup>2</sup> These results are published in *Advanced Materials* [doi 10.1002/adma.200801432], *Nano Letters* [doi 10.1021/nl200426g], *MRS Proceedings*, [doi 10.1557/PROC-1236-SS09-07] and *Nano Today* [doi 10.1016/j.nantod.2011.12.005].

aspect ratios were achievable, and irreversible collapse was shown to occur in high-aspect-ratio posts.(94) Fabricating high-aspect-ratio (HAR) fibers inspired by biological

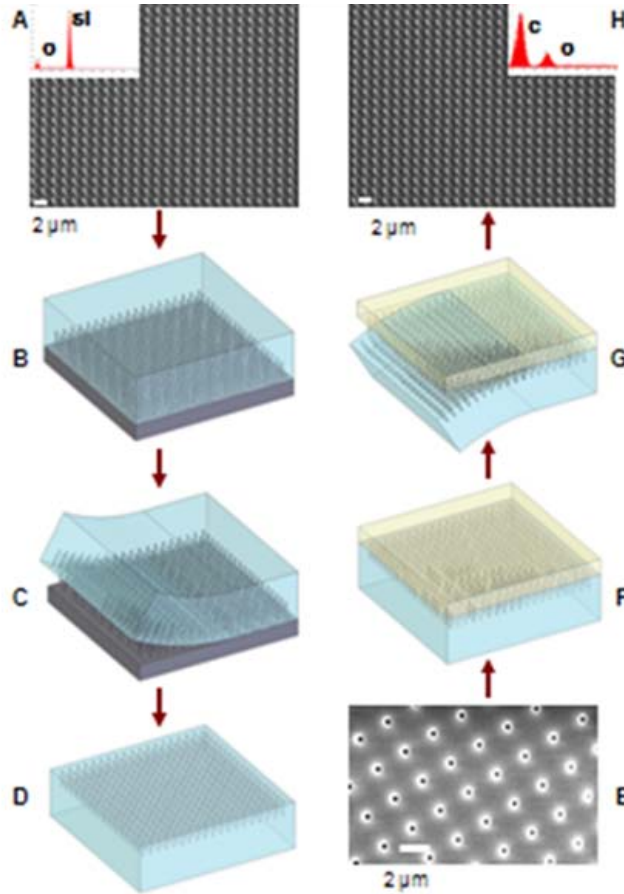


Figure 12. Two-step soft lithography process for creating replicas of nanostructured surfaces with high-aspect-ratio features. (A) SEM image of an exemplary original nanostructured surface—a silicon master bearing a square array of 8- $\mu\text{m}$ -long posts with the diameter of 250 nm and the pitch of 2  $\mu\text{m}$ . The oblique view is used to best visualize the structure. The insert is an EDS spectrum. B) Liquid PDMS precursor is poured onto the master treated with an anti-sticking agent and cured. C) The cured PDMS is peeled off from the master. D) The negative PDMS mold, which contains an array of high-aspect-ratio wells corresponding to the posts of the positive master, is surface-treated with an anti-sticking agent. E) SEM image of the PDMS mold, revealing the high-aspect-ratio wells. F) Liquid precursor (polymer, liquid metal) is poured onto the negative PDMS mold and cured. G) The PDMS mold is peeled from the cured positive replica. H)

Figure 12 (Continued)

SEM image of an exemplary nanostructured replica fabricated from epoxy resin. The insert is an EDS spectrum. The replicated structure is geometrically indistinguishable from the master shown in A.

structures such as neuromasts or cilia requires more stability and rigidity than provided by such a soft elastomer. Hence we have built upon the soft lithography replication method to allow the fabrication of a biomimetic array of stable, high-aspect-ratio features, a critical functional requirement of biological actuated nanostructures and sensors. In our approach, we employ a double-replication approach as shown in Figure 12, and we cast the final replica in the material or materials of choice. PDMS is not the final nanostructured material: it is used as a secondary elastomeric mold for casting the replica in the material of choice. As a result, the stability and stiffness of the replicated structures can be controlled by choosing as the final material one with the desired mechanical properties. With this basic approach, it becomes possible to tailor the properties of HAR structures' stability and stiffness through material design, as well as to effect nontrivial transformations of the nanostructure geometry and surface chemistry following the casting step (95-97).

## **B. Master design options**

In the double replication approach (Figure 12), the initial master surface can be formed by standard lithographical techniques, grown bottom-up (for example, nanowires), or even be a live biological sample (98). Nearly any topography can serve as

a master surface, with the main requirement being that the negative mold must be able to peel off or detach easily, ensuring that the master remains undamaged and is faithfully replicated. The master can also be treated with a nonstick surface chemistry such as fluorinated silane to aid peel-off. From a fabrication design perspective, parameters such as the fiber spacing, radius, length, etc., can be specified in the master, but these parameters can also be extensively modified downstream in our platform. In Figure 12A, we have taken a Si nanofiber array that was produced by Bosch etching, a pulsed etching-passivation technique that allows very high aspect ratio structures to be made (99). The pitch (center to center distance between the posts) is  $a_0 = 2 \mu\text{m}$ , post radius  $r_0 = 125 \text{ nm}$  and post length  $l_0 = 8 \mu\text{m}$ , for an aspect ratio of 32.

### C. Negative mold considerations

We cast a negative replica of the fibrous master in either PDMS or other nonstick materials, such as polyfluoropolyether (PFPE) and paraffin (Figure 12B-E). PDMS offers a number of advantages: it is inert, reusable, and inexpensive. It is compliant and elastically deforms up to 300% strain, such that it releases well even from rough master topographies. A PDMS mold can even be used to cast PDMS replicas by applying a fluorinated layer to the mold surface. In any case, the mold (Figure 12D-E) has an array of wells, into which the final replica material is cast in liquid or vapor form and solidified (Figure 12F). The mold is then either peeled off (PDMS, PFPE) (Figure 12G) or heated and sacrificially dissolved (paraffin). Figure 12H shows an epoxy replica of the original silicon HAR nanofiber array, which is indistinguishable by SEM.

The fabrication procedure up to this point is outlined in Figure 12. The initial high-aspect-ratio master can be either formed by standard lithographical techniques, grown bottom-up (for example, nanowires) or a biological sample. In this paper, we demonstrate our procedure by replicating arrays of Si nanoposts with the pitch  $a_0$  (distance between the posts), the post radius  $r_0$  and length  $l_0$  (Figure 12). We formed a negative replica of the structure coated with an anti-sticking thin layer in PDMS or paraffin (Figure 12B-E). An important requirement is that the negative replica must be able to peel off or detach easily without disrupting the Si fine structure, so that the features are accurately replicated on a large scale (Figure 12C). The created PDMS or paraffin mold (Figure 12D-E) has an array of wells, into which the desired material (polymer, liquid metal or ceramics) is cast in liquid form and cured (Figure 12F). The mold is then either peeled off (PDMS) (Figure 12G) or heated and dissolved (paraffin) to reveal the replicated structure. Figure 12H shows an epoxy-replicated nanoarray that reproduces the original master with the nanometer-scale resolution. These surfaces exhibit superhydrophobic, self-cleaning properties and the water droplets remain suspended on the tips of the nanoarray and roll off the surface, similar to the properties reported for the original Si masters.(64, 100)

#### **D. Double replication experimental details**

An array of silicon nanoposts was fabricated using the Bosch process, as described elsewhere. (99-100) The silicon nanopost arrays were treated with an anti-sticking agent (tridecafluoro-1,1,2,2-tetrahydrooctyl)-trichlorosilane (Gelest Inc.) by exposure in a desiccator under vacuum overnight.

Negative replicas were produced from polydimethylsiloxane (PDMS) (Dow-Sylgard 184) with a prepolymer-to-curing agent ratio of 10:1. After extensive mixing of the prepolymer and curing agent, the mixture was poured on the silicon nanopost substrate and placed in a vacuum desiccator for one hour to eliminate all air bubbles. It was then thermally cured in an oven for 3 hours at 70° C. After cooling, the negative PDMS mold was gently peeled off the substrate. The negative PDMS mold was then cleaned extensively with ethanol, isopropanol, and acetone sequentially, dried and treated in nitrogen plasma for 1 min in a Femto Diener<sup>®</sup> plasma cleaner. After this surface treatment, the negative mold was placed in (tridecafluoro-1,1,2,2-tetrahydrooctyl)-trichlorosilane environment in a desiccator under vacuum overnight.

In order to produce the final replica of the master one pours the desired material in liquid form into the negative replica wells (Figure 12F). It is essential to ensure that this material completely fills the negative replica and solidifies inside it. In order to prevent the formation of bubbles trapped between the mold material and the original structure, a vacuum is applied over the liquid. Once the material has solidified, the negative replica is simply peeled off, leaving behind the free-standing nanostructured material. Using this method one can form replicated nanostructures from a variety of materials such as: polymers (e.g. epoxy, PP, PE, PVA, PMMA, PDMS, various hydrogel and shape memory polymers) and metals and alloys which have a low melting point (e.g. Ga, InBi and Woods alloy). In this work most of the nanostructured replicas were made from a commercial UV-initiated one-part epoxy UVO-114<sup>™</sup> (Epoxy Technology). This epoxy was chosen due to the ease of use and a relatively high Young's modulus of ~1 GPa.

For the experiments involving the control of the flexural modulus of the nanostructures, two liquid epoxy resins—Dow D.E.R. 331™, a liquid reaction product of epichlorohydrin and bisphenol A, and Dow D.E.R. 732™, a viscosity-reducing reaction product of epichlorohydrin and polypropylene glycol—were mixed in different proportions. The mixtures were based on 10% increments of components by weight, from 10 % to 100 %. In all compositions, UV cross-linking initiator Cyracure UVI 6976™ (Dow) was added to the mixture in a constant 5 weight % amount.

To produce 4-point flexure test epoxy samples, 10 x 8 x 62 mm custom aluminum blocks were placed in a glass bowl; PDMS was poured and cured as described above to create molds. Each of the eleven epoxy mixtures as well as the commercial UV-initiated one-part epoxy UVO-114™ (Epoxy Technology) were sequentially pipetted into the PDMS molds flush with the tops of the wells. Each flexure sample was cured by placing molds directly under a B-100 ultraviolet lamp (UVP Blak-Ray) inside a photochemical cabinet until fully cured, which required from 20 minutes to several hours depending on the composition. Mixtures with higher percentage of D.E.R. 331 required more time to crosslink.

A custom-built mechanical test system was used to test the epoxy samples in 4-point bending and determine their flexural modulus. The system had a displacement resolution of 10 nm, controlled by a step motor with 100 N capacity, and a load resolution of 0.01 N. It was set up on a pneumatic table to shield against vibration and was operated by a computer through LabView. The fixture's upper anvil pins were set at 28 mm apart and lower pins were spaced at 56 mm. A displacement rate of 500 μm/s and a maximum deflection of 3 mm were used for compliant samples, decreasing to 0.5-1.5

mm deflection for stiffer samples, as dictated by the step motor maximum load. The load-deflection data were plotted into linear elastic curves whose slopes were calculated and, along with the anvil and sample geometries, were used in the 4-point bending equation to obtain the flexural moduli of the epoxy replicas.

### **E. Breaking the one-to-one replication barrier with elastomeric mold deformation: array-level geometry control**

The fabrication of fibrous surfaces with varying geometric parameters using a basic one-to-one double-replication procedure can become prohibitively expensive, requiring customized Si masters for each new design. Moreover, conventional lithography limits fabrication to normally oriented nanofibers. In biological systems, however, natural high-aspect-ratio fibers are often oriented in various directions and have a range of anisotropic cross-sections with important functional implications (101-102).

For example, tilted fibers are critical in the adhesive properties (103) of gecko feet on surfaces and to anisotropy in wettability in some man-made nanostructured surfaces. (104) The elliptical cross-section of superficial neuromasts—structures that detect water flow on the body surface of fish and amphibians—provides the ability to discern the direction of water flow. (76).

One breakthrough of our approach is that the replication no longer need be a one-to-one process. Nontrivial geometric transformations from the master to the replica are easily achieved by deforming the flexible negative PDMS mold after casting but before solidifying the final replica material. The mold deformation technique allows us to form a wide range of nanofiber array geometries, including different 2D lattice symmetries and



fiber cross-sectional shapes, all based on the same original master (95). We can uniaxially extend, compress, bend, shear, or twist the mold to transform the original geometry, as shown in Figure 13A-H. PDMS is an optimal mold material in this regard because its low Young's modulus and high elastic limit differentiate it from rigid molds that strictly permit one-to-one replication.

There are several types of array-level geometric control enabled by PDMS mold deformation, with exemplary deformation types shown in Figure 13 and summarized in Table 3. The deformation magnitude and direction simultaneously determine the final unit cell of the nanoarray and the degree of cross-section anisotropy. Hence, this is a

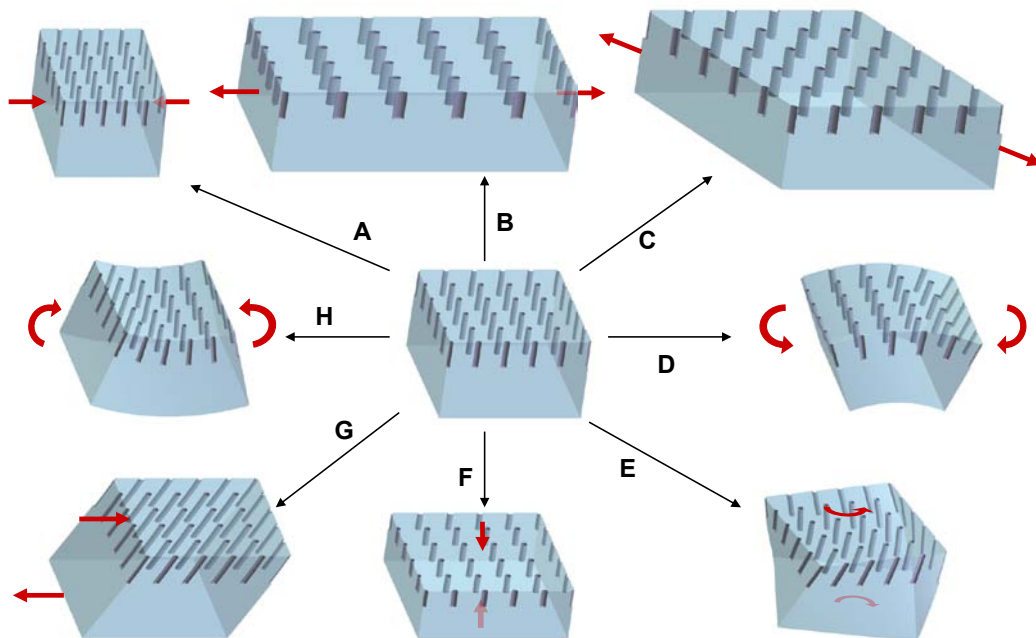
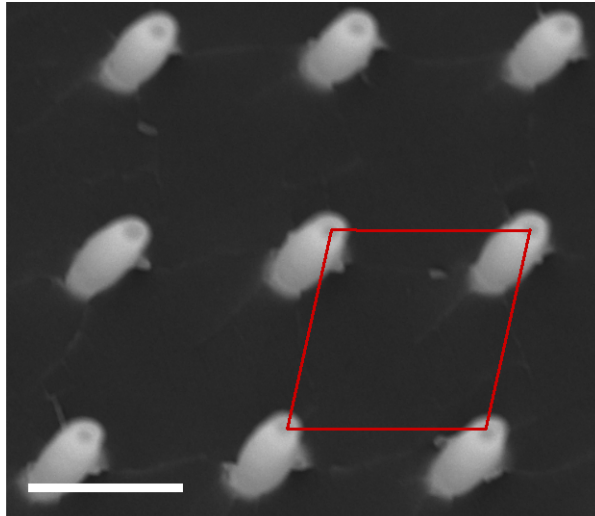


Figure 13. Schematic three-dimensional renderings of various deformations of the PDMS mold, which allow the fabrication of arbitrary arrays of nanosticks with finely-tuned geometries and nontrivial configurations. The unmodified mold (center) can be: A) compressed along the  $[100]$  direction; B) stretched along the  $[100]$  direction; C) stretched along the  $[110]$  direction; D) uniformly curved concavely; E) torsioned around the  $[001]$

Figure 13 (Continued)

axis; F) compressed along the [001] direction; G) sheared along the [100] direction; or F) uniformly curved convexly.

proportional transformation process, and there is a coupling of feature and array-level geometry control. By deforming the PDMS negative molds via stretching or compression in the principal directions of the 2D array of posts, we can transform the original 2D square lattice to a rectangular or rhombic lattice and the original circular cross-sections of the nanoposts to elliptical (Table 3, Figure 13A-C). By deforming the mold in the general [hk0] direction, a parallelogram unit cell with finely-tuned parameters can be formed. The amount of the deformation determines both the degree of ellipticity and the unit cell of the nanoarray. Tilted structures can be formed by applying a shear deformation to the mold. The amount of the shear determines the tilt angle, and the direction of the shear determines the tilt direction. The length of the posts,  $l_0$ , can be changed by compressing the negative mold perpendicular to the 2D array (Table 3, Figure 13F). We also have the ability to form twisted nanostructures (Figure 13E) or curved surfaces with different radii of curvature (concave or convex) very similar to echinoderm skin (Figure 13D,H). To ensure the fabrication of an arbitrary array of nanostructures, any combination of the deformation types can be applied. Figure 14 shows an example of an epoxy nanostructured surface that was fabricated using a compound deformation of the mold consisting of a square array of normally-oriented, 8  $\mu\text{m}$ -deep, circular wells with  $a_0 = 2 \mu\text{m}$  and  $r_0 = 125 \text{ nm}$ . By applying a 20% stretch and 12.5% shear in the [110] direction, we created a structure that exhibits tilted nanoposts with  $t \cong 7^\circ$ ,  $\theta \cong 78^\circ$  and  $a \cong 2.18 \mu\text{m}$ .



**2  $\mu\text{m}$**

Figure 14. SEM image of an epoxy nanopost array fabricated using a compound deformation that included a 20% stretch and 12.5% shear in the [110] direction, viewed normal to the surface. The 2D array of posts displays a rhombic symmetry (unit cell highlighted in red). This combined deformation-mode created a structure that exhibits tilted nanoposts with  $t \cong 7^\circ$ ,  $\theta \cong 78^\circ$  and  $a \cong 2.18 \mu\text{m}$ .

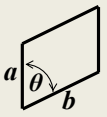

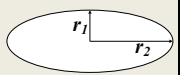
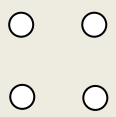
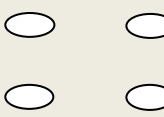

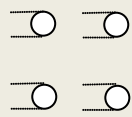
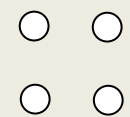
Parameter	Deformation Type				
	No deformation	Stretching / compressing along [100]	Stretching / compressing [110]	Shearing along [100]	Compression along [001]
<b>a</b>	$a_0$	$1/3a_0 < a < 3a_0$	$a_0 < a < 2.1 a_0$	$a = a_0$	$a \cong a_0$
<b>b</b>	$b_0 = a_0$	$3a_0 > b > 1/3a_0$	$b = a$	$b = a_0$	$b = a$
<b><math>\theta</math></b> 	$\theta_0 = 90^\circ$	$\theta = \theta_0$	$12.5^\circ < \theta < 167.5^\circ$	$\theta = \theta_0$	$\theta = \theta_0$
<b>Tilt (<math>t</math>)</b> 	$t_0 = 0$	$t = t_0$	$t = t_0$	$0 < t < 63.4^\circ$	$t = t_0$
<b>Post lengths (<math>l</math>)</b>	$l_0$	$l \cong l_0$	$l \cong l_0$	$l_0 < l \leq \sqrt{5}l_0$	$1/3l_0 < l < l_0$
<b>Cross section</b> 	$r_1 = r_2 = r_0$	$r_1 < r_2$	$r_1 < r_2$	$r_1 = r_2 = r_0$	$r_1 = r_2 > r_0$
<b>2D array symmetry</b>	square 	rectangular 	rhombic 	square 	square 

Table 3. Deformation-induced changes in the geometry of the replicated nanostructures. One can linearly extend PDMS to 3 times its original length and the Poisson's ratio of PDMS is  $\nu = 0.5$  (105). All calculations have taken the Poisson's ratio effect into account. Note:  $r_1$  and  $r_2$  are the radiuses of the cross-section in the principle directions 1 and 2 respectively.

## **F. Control of the mechanical and other properties by material selection**

Another key advantage of our fabrication platform is the ability to specify the materials comprising the fabricated nanofibers. Whereas conventional lithographic procedures are limited essentially to silicon, the Young's modulus of a double-replicated nanostructure can vary from less than one MPa to hundreds of GPa (95, 106). Using this method one can form replicated nanostructures from synthetic as well as biological polymers (e.g., epoxy, hydrogels, silk, shape memory polymers), metals with a low melting point (e.g., Wood's and Field's alloys), and ceramics deposited through atomic layer deposition (e.g., alumina), as shown in Figure 15R. Furthermore, the Young's modulus of the array can be finely controlled by varying the ratio of two different prepolymers. As shown in Figure 16, by variably mixing two epoxy formulations, we have produced epoxy nanofiber surfaces with a modulus ranging from tens of MPa to several GPa (95). The modulus range of such a two-polymer system was extended another order of magnitude through compositing silica nanoparticles in the polymer matrix, reaching tens of GPa. A modulus-versus-composition calibration curve based on a series of material tests provides us the means to control fiber modulus and functions such as passive bending (107). Figure 16 prescribes the recipe for a polymer mixture that will endow a nanopost array with an arbitrary, required stiffness in the MPa-GPa range.

Figure 15. The overall fabrication platform for bioinspired arrays of high-aspect-ratio nanostructures. (A) SEM image of an exemplary original nanostructured surface—a silicon master bearing a square array of 8- $\mu\text{m}$ -high fibers with a diameter of 250 nm and a pitch of 2  $\mu\text{m}$ . The insert is an EDS spectrum. (B) Liquid PDMS or other elastomeric negative mold precursor is poured onto the master, which may be treated with an anti-sticking agent, and cured. (C) The cured PDMS is peeled off from the master. (D) The negative PDMS mold, which contains an array of high-aspect-ratio wells corresponding to the nanofibers of the positive master, can be surface-treated with an anti-sticking agent. (E) SEM image of the PDMS mold, revealing the high-aspect-ratio wells. (F) Liquid precursor (polymer, liquid metal) is poured onto the negative PDMS mold and cured. Alternatively, ceramic precursor may be deposited by atomic layer deposition. (G) The PDMS mold is peeled from the cured positive replica. (H) SEM image of an exemplary nanostructured replica fabricated from epoxy resin. The insert is an EDS spectrum. The replicated structure is geometrically indistinguishable from the master shown in A). (I)-(P) Schematic 3D renderings of various deformations of the PDMS mold, which allow arbitrary array-level geometric control with finely tuned geometries and nontrivial configurations (95). The unmodified mold (center) can be: (I) compressed along the [100] direction, (J) stretched along the [100] direction, (K) torsioned about the [001] axis, (L) uniformly concavely curved, (M) sheared along the [100] direction, (N) compressed along the [001] direction, (O) stretched along the [110] direction, or (P) uniformly convexly curved. (Q) top view of an epoxy nanofiber array fabricated using a compound shear and 45° extension of the mold. (R) Geometric control of the replica via negative mold deformations can be compounded, for example a [110] extension and a shearing-induced tilt. (S) A wide range of materials may be used for the final nanoarray. SEM image is of ceramic nanofibers cast from a PDMS mold by ALD. (T)-(W) Casting of the replica material in liquid form enables arbitrary Young's modulus—at least 5 orders of magnitude—and other material properties. Furthermore, it is possible to fabricate multi-material replicas that provide spatial control of stiffness, magnetization, etc. and introduce functional gradients in the system. (106) As an example, rigid fibers may be flexibly tethered to a rigid substrate via an elastomeric layer for controlled actuation only at the base. (X) Surface chemistry can be modified independently of the

Figure 15 (Continued)

materials choice by plasma treatment or thiolation. (Y) Schematics showing the step-by-step feature-level geometric control of structural transformation by electrodeposition on patterned substrates (STEPS). The dimensions of the features can be finely tailored independent of the array parameters using this part of the fabrication platform (97). The three schemes employ either a sputter-coated metal electrode (type I), evaporated metal electrodes from the top (type II), or evaporated metal electrodes at an angle (type III). Green: parent substrate, yellow: metal coating, blue: polypyrrole. SEM insets (Z) show the gradually increasing diameter of cylindrical fibers and the decreasing space between adjacent fibers as type I deposition progresses from right to left; an array of conical nanostructures transformed by type II from cylindrical fibers; directionally bent conical structures transformed from upright cylindrical fibers using STEPS type III.





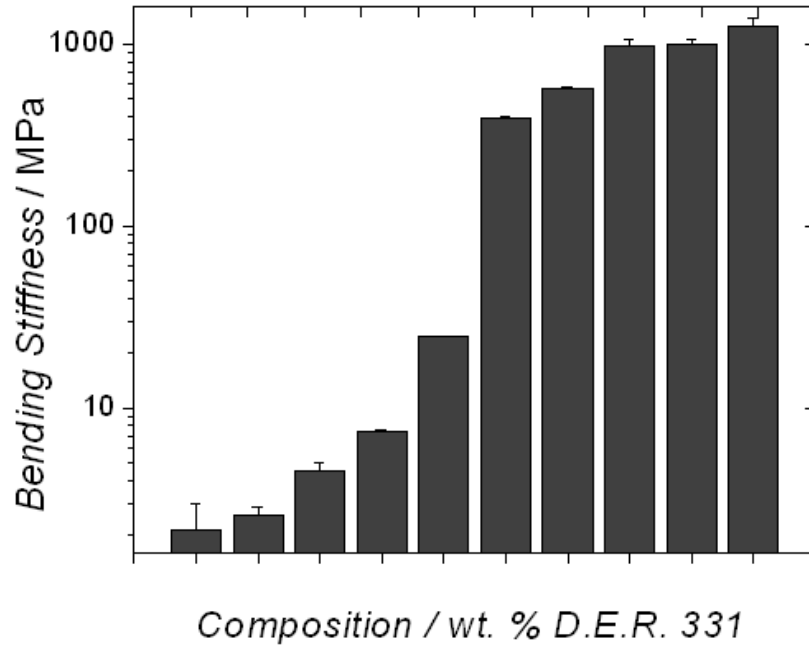


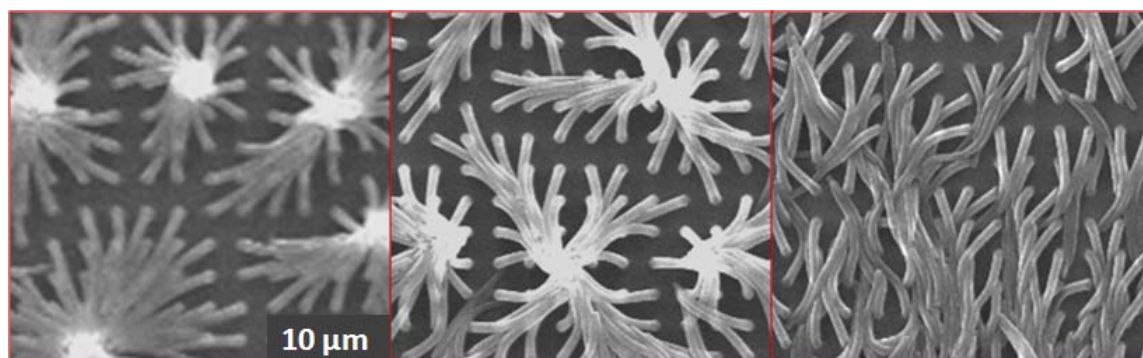
Figure 16. Three orders of stiffness magnitude are accessible via simple prepolymer mixing.

Beyond monolithic replicas comprised of a uniform material system and mechanical properties, we have extended our method to make possible spatially defined multi-material nanofibers for sophisticated sensitivity and assembly behavior (Figure 15T-W and Figure 17). To achieve this, multiple casting materials are stratified during the casting process depicted in Figure 15F to vary relevant properties along the height of the structure. The fibers may be fabricated from a stiff replica material (shown in green), for example, while the bulk substrate is flexible (shown in red); or there can be a compliant interlayer linking the stiff nanostructures and the stiff substrate. To fabricate a multi-material nanoarray, additional steps are added to the core fabrication process. Once the replica prepolymer is applied to the negative mold and allowed to fully penetrate the

wells, the excess is removed. At this point, a compliant interlayer can be spin-coated on at a lower speed and cured, followed by regular casting of the substrate (106). Material property gradient control between the bulk and nanofiber materials is possible, for example by varying the degree of crosslinking of one material layer before interdiffusion with the next layer.

Such a “flexible anchoring” configuration, depicted in Figure 15W, is of great functional interest. Biological structures such as the superficial neuromasts of fish depend on stiffness gradients and anisotropy (69), pointing to important applications in the fabrication of engineered nanoarrays for flow sensors and sophisticated artificial cilia. The higher elastic range of motion allowed by flexible anchoring points also suggests that these nanostructures are mechanically more resilient than their monolithic analogues. Flexibility of the anchoring points is demonstrated by solvent evaporation-driven capillary assembly of stiff monolithic, hybrid-stiffness, and soft monolithic nanoposts in Figure 17.

Meanwhile, we have fabricated a proof of concept for mechanically actuated rigid epoxy micro/nanostructures attached to a flexible PDMS substrate. In Figure 18 we imaged the sample on an optical microscope under continuous, cyclic uniaxial extension and tracked the motion of the rigid posts relative to one another. The unit cell was extended 60% in the load direction, with a corresponding Poisson contraction. This novel hybrid replica was extremely flexible and contour-fitting, as also seen in Figure 18.



**Uniform Stiffness**  
1 GPa

**Hybrid Stiffness**  
1 GPa posts/100 MPa substrate

**Uniform Stiffness**  
100 MPa

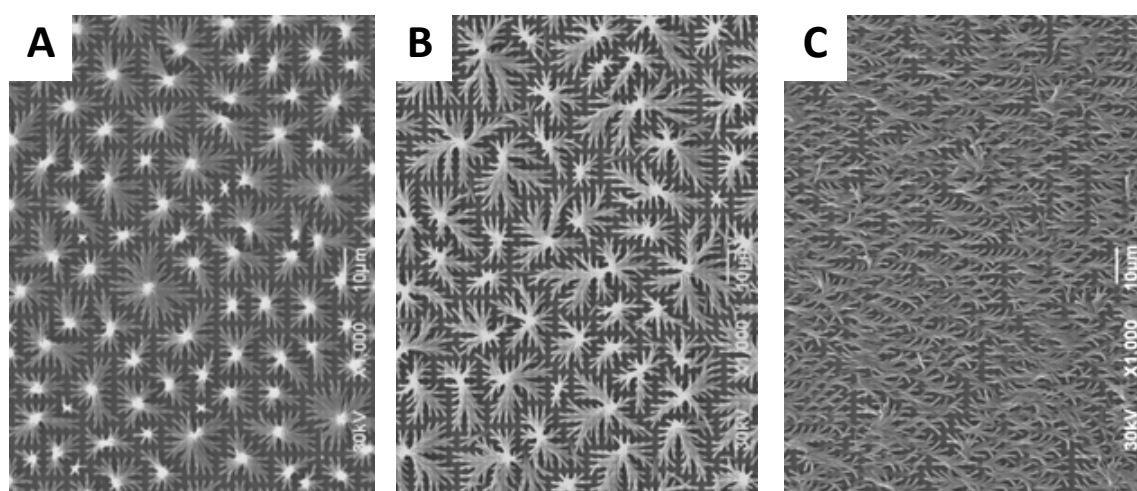


Figure 17. Anchoring point flexibility is seen in the hybrid stiffness nanoarray replica (B), in which rigid posts are able to elastically hinge at their soft attachment points. The hybrid posts can tilt more than the monolithic rigid system (A) but do not bend above the attachment point as in the all-soft system (C).

In addition to spatial control over material composition, we can also vary the surface chemistry of the fibers (Figure 15X) by using plasma treatment or functionalization. These treatments allow us to modulate the mechanical and adhesion properties independently and extend our control over surface phenomena such as wetting.

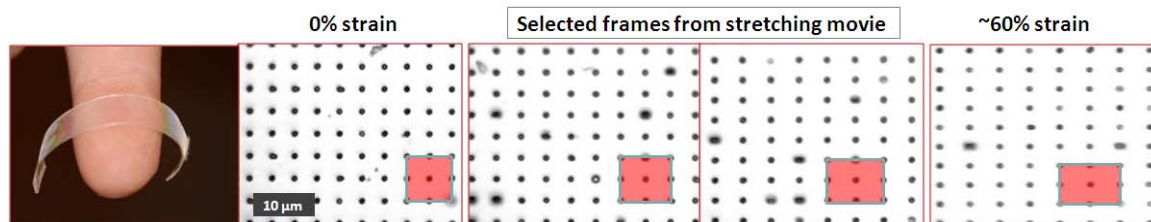


Figure 18. Mechanical in-plane actuation of micro/nanoscale rigid posts that are attached to a flexible, extendible elastomeric substrate, strained by a motorized stage. The sample is shown fitting the contour of the author’s finger at left.

Due to the relatively low forces needed to move the posts in our typical structures, we can also demonstrate actuation under the Scanning Electron Microscope (SEM) (see Figure 19B). In this case, the actuation is probably driven by the electrostatic forces imposed by the e-beam, as modeled by Seminara, et al. (108) This movement is reversible and can be repeated multiple times: the posts bend into the e-beam when the beam is focused on a small area, and return to their normal orientation once the e-beam is not concentrated on a small scanning area. The actuation of the array of tilted nanoposts (as in many biological systems) is shown in Figure 19C. We emphasize that this is only an illustration of the ability of these posts to respond in a controlled manner to an external force.

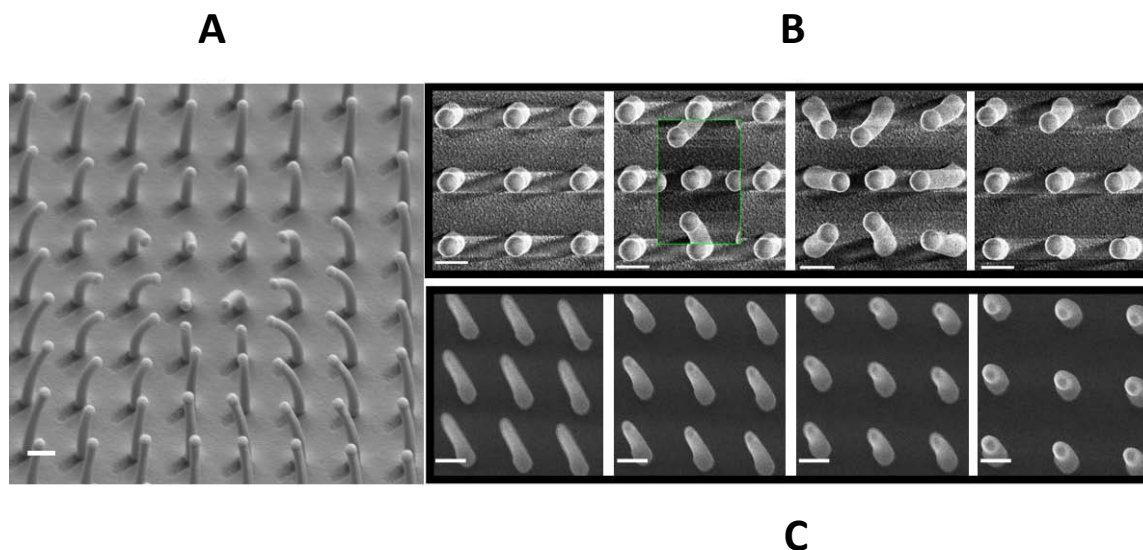


Figure 19. SEM images of electron beam actuated epoxy nanoposts. (A) Area of posts that have been forced to bend into the center of the e-beam scanning area. This image was captured after focusing at high magnification for a short period and then rapidly increasing the scanning area. The viewing angle is oblique to the surface. (B) Illustration of the reversible character of the actuation process, showing snapshots from the full movie. From left to right: time zero just as the e-beam was applied; bent posts after the e-beam was focused on the outlined area for 29.5 sec, contrasted with their original condition in the frozen background; extensive post relaxation after the e-beam was allowed to scan a larger area again. (C) Illustration of the actuation of the posts that were initially in a tilted position (produced by shearing of the PDMS mold during the epoxy-curing procedure), showing snapshots. From left to right: time zero just as the e-beam was applied; after 1.2 sec of exposure; after 2.4 sec of exposure; and after 5.3 sec of exposure.

**G. Beyond proportional transformation: feature-level control of geometry, mechanics, and function based on Structural Transformation by Electrodeposition on Patterned Substrates (STEPS)**

Up to this point, our fabrication platform has augmented the core double-replication process with both extensive material and array-level geometry control. Yet programming mechanics, geometry, and function at the feature level, independent of the array-level properties, has not been possible. For example, deformation of a mold in the  $[hk0]$  direction intended to change nanoarray symmetry also changes the fiber cross-section, which may or may not be desired.

Recently we have developed a new nanofabrication method that allows an array of nanofibers to be precisely re-shaped by the deposition of conductive polymers. This method, referred to as “Structural Transformation by Electrodeposition on Patterned Substrates” (STEPS), breaks the proportional transformation barrier and makes it elementary to change feature-level dimensions and to produce nontrivial 3D transformations—all without changing the 2D lattice. The transformed nanofibers can then be used as masters for double-replication into the desired materials. Tapered, anisotropic, curved, and overhanging shapes can all be readily made by STEPS, and isolated nanostructures can even be bridged to form continuous networked arrays for new classes of bioinspired applications (97).

To produce feature-level geometric transformations, a metal layer (e.g. gold or platinum) is first deposited onto a HAR nanofiber array. Since our original Si nanofiber master is fabricated by the Bosch process, an iterative etching process, both the Si and

replicated epoxy fiber walls are scalloped rather than smooth (which affects the metal layer and polymer deposition as discussed below.) The metal layer functions as an electrode, and when the sample is placed into a conductive monomer aqueous solution and voltage is applied, conductive polymer (e.g., polypyrrole) starts to electrochemically deposit on the metal. The rate of deposition is controlled by changing the voltage, while the size and shape of the resultant HAR fibers are precisely controlled by adjusting both the voltage and total electrodeposition time (97). Figure 15Y summarizes three process schemes for controlling the feature-level geometric control of scalloped fibers.

Depending on the metallization method, each scheme enables specific transformation types. In scheme I, a continuous electrode is formed by isotropic sputtering.

Electrodeposition on sputter-coated electrodes (type I) results in a smooth, conformal film that increases the fiber dimensions by the deposited thickness in all directions. This effectively increases diameter without significantly changing length. At the same time, the spacing between adjacent pillars decreases and the space-filling factor of the substrate increases, as shown in Figure 15Z for a square array of HAR nanofibers. In STEPS types II and III, a set of discontinuous electrodes is formed by line-of-sight electron beam evaporation on the tops of sidewall scallops. These isolated electrodes set the stage for our unique ability to modify nanofiber profile along the axial direction; hence, what is typically seen as a fabrication defect of the Bosch process is exploited in STEPS (109). The large continuous electrode on the substrate surface causes polymer to deposit only there initially, but this layer eventually connects to the ring electrode on the first scallop and bridges the gap. From then on, the polymer continues jumping the “rungs” of an electrode “ladder” and the resulting gradient of deposition time from basal to distal ends

of the nanostructure leads to the conical transformation as shown in Figure 15Y,II. This enables applications such as mechanical reinforcement of nanoarrays for robustness (97), controlling fiber assembly-based particle capture properties, etc. New anisotropic geometries furthermore become possible when metal electrodes are deposited onto the nanostructures at an angle, forming C-shaped electrodes on each fiber scallop (Figure 15Y,III). Electrodeposition on this substrate forms a polymer backbone on one side of each fiber, causing it to bend like a bimetallic strip. Such a curved geometry is distinct from and complements the straight tilted geometry produced by mold shearing. These curved nanostructures allow further control of anisotropy in assembly.

Perhaps most importantly, with the capability to create either continuous or stepwise gradient patterns from a single master structure, the final nanofiber arrays no longer need to be uniform over their entire area. We can perform either continuous or stepwise withdrawal of the substrate from the electrodeposition bath, leading to a gradient of electrodeposition time along the substrate withdrawal direction and therefore to a gradient of geometrical parameters. Multiple gradients, such as orthogonal or triaxial, can even be fabricated on a single substrate by rotating the axes of gradients over two or more electrodeposition steps. The resulting combinatorial libraries have made it possible for the first time to systematically study the combinatorial effects of geometric parameters on surface properties on a single substrate. This capability allows us to co-optimize the surfaces for self-assembly and a wide range of downstream applications, including nanotopographic cues for bacterial and cell behavior on patterned substrates, screening mechanical robustness of different taper profiles against abrasion, memory and



storage, ciliary transport in microfluidics, fluid flow sensing, dry adhesion, and water and ice repellency (110-113).

## **H. Unifying the fabrication platform to rationally program nanostructure performance**

When engineering a functional surface bearing high-aspect-ratio nanoposts, one should consider the stability of the expected structures. There are several factors that can lead to the collapse of nanoposts (114): a collapse due to the self-weight (115); adhesion forces between the posts and the base surface (94); and lateral adhesion. (115)

Calculations show that the first two are much too small to affect our structures; however, the importance of the second factor increases in the case of tilted nanostructures. The lateral adhesion force is the strongest of the three and has to be taken into account. The critical aspect ratio, below which there will be no lateral collapse, is given by

$$\frac{l}{d} = \left( \frac{0.57E^{1/3}a^{1/2}}{\gamma_s^{1/3}d^{1/6}(1-\nu^2)^{1/12}} \right) \text{ where } d \text{ is the diameter of the posts, } \gamma_s \text{ is the surface energy}$$

and  $\nu$  is the Poisson ratio of the nanostructured material and  $a$  is the pitch. (94, 114)

The mechanics of nanoposts is a key issue when designing surfaces for functional assembly processes and applications in actuation/sensing. To control the mechanical sensitivity of the nanoarray, we may systematically apply the different parts of our fabrication platform, combining mold deformation, material selection, and STEPS feature-level transformation. Considering the final nanostructure, when a stimulus force  $F$  acts on the tip of a nanopost of length  $l$ , perpendicular to the fiber, the tip deflection  $\delta$  is given by  $\delta = Fl^3 / 3EI$ , where  $E$  is the Young's modulus and  $I$  is the moment of inertia

(116). For a post with a circular cross-section of radius  $r$ , the moment of inertia is given by  $I = \pi r^4/4$ . Given typical values for epoxy nanoposts of  $E = 1$  GPa,  $l = 8$   $\mu\text{m}$ ,  $r = 125$  nm, a force of about 1.1 nN is needed to deflect the tip of the post by 1  $\mu\text{m}$ . As shown in Figure 20, to control post flexibility we can adjust the radius (which scales as fourth power), the length (cubic power), the modulus (linear dependence), or any combination thereof (95). As both geometric and material parameters control the nanoarray sensitivity, it is very helpful to consider the “effective stiffness”  $S_{effect} = F / \delta$ , where  $\delta$  is the deflection, to help determine what strategy to employ for a target flexibility range. For nanoposts of arbitrary dimensions and materials, the ratio of their  $S_{effect}$  allows their direct comparison, e.g., for a circular cross-section:

$$\frac{S_{1effect}}{S_{2effect}} = \left( \frac{E_1}{E_2} \right) \left( \frac{l_2}{l_1} \right)^3 \left( \frac{r_1}{r_2} \right)^4$$

This dimensionless parameter allows the direct and simple comparison of the effective bending properties of the nanostructures.

The demonstrated unique capability of our approach to create nanostructures with elliptical cross-sections would also make it possible to design a truly biomimetic sensor that responds to an anisotropic flow field in a manner similar to cilia in fish and amphibians. (76) In this case, the moment of inertia in the directions of the two radii will be:  $I_1 = \pi r_1^3 r_2/4$  and  $I_2 = \pi r_1 r_2^3/4$ , and for the given force, the deflection in the direction of  $r_1$  compared to  $r_2$  scales as  $(r_2/r_1)^2$ .

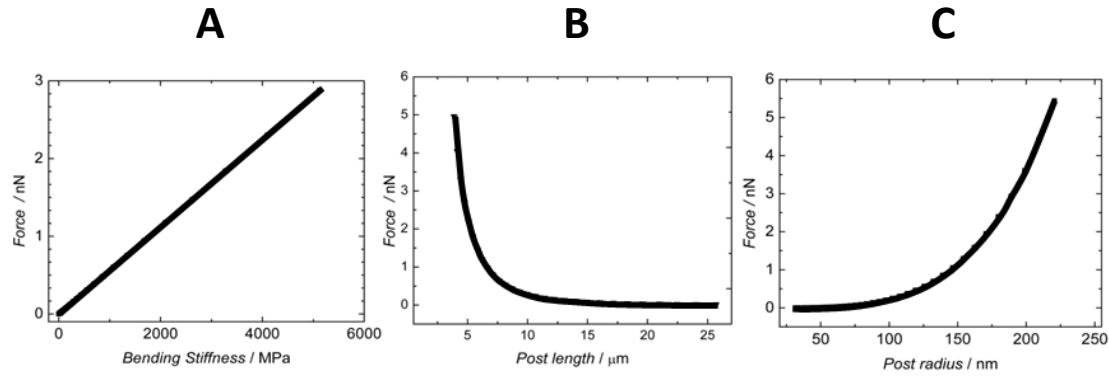


Figure 20. Relationships between geometric parameters and the applied force required at the tip of a nanopost to bend it to a given deflection,  $Y_{lz} = 0.5 \mu\text{m}$  as a function of (A) post bending modulus [ $l = 8 \mu\text{m}$ ,  $r = 125 \text{ nm}$ ]; (B) post length [ $r = 125 \text{ nm}$ , and  $E = 1 \text{ GPa}$ ]; and (C) post radius [ $l = 8 \mu\text{m}$ ,  $E = 1 \text{ GPa}$ ].

Complex 3D microstructures with tightly tuned mechanics can be fabricated simply by combining multiple STEPS methods, e.g., starting with a modified-feature nanoarray or its replica, and evaporating a new set of metal electrodes and performing subsequent STEPS procedures. Moreover, serial composition of STEPS can be combined through iterative mold-cast cycles with the mold deformation and materials selection aspects of the overall fabrication platform for virtually limitless programming possibilities. Indeed, all these sub-methods can be combined over one or multiple fabrication cycles to yield an enormous range of mechanical, geometric, and material properties.

#### **4. Empirical nanopost mechanical properties to validate design and evaluate for applications<sup>3</sup>**

##### **A. Motivation for an empirical characterization method**

Designing functional nanoarrays with specific mechanical properties is only possible if we are able to characterize their real behavior and calibrate our predictions with empirical results. Indeed, we have up to this point relied on Eulerian beam mechanics to predict and design the sensitivity of a HAR nanostructure to the applied force. Given that these structures are in the submicron range, where surface area to volume ratios are significantly higher than in the macroscopic regime, it is not necessarily a given that macroscale beam mechanics can be applied without correction. Furthermore, many mechanical properties of nanoarrays cannot easily be modeled *a priori* because of their complexity and nonlinearity.

Relatively scant attention has been devoted to the mechanical robustness and fitness for technological application of nanofibrous surfaces beyond the bench. Along the lines of our previous nanoindentation study on a gradient of micropost taper profiles (97), the studies that have been reported principally rely on ensemble measurements (117-120). Others are even coarser, applying such test methods as bulk abrasion (121). Systematic mechanical tests of individual HAR surface nanofibers have not been described to our knowledge.

---

<sup>3</sup> These results are published in *Nano Letters* [doi 10.1021/nl200426g] and in *Nano Today* [doi 10.1016/j.nantod.2011.12.005].

## **B. Nanoindentation (NI) for multi-structure measurements of engineered polymeric microstructures**

HAR nanopillars practical usefulness in a wide range of potential technologies can be limited by poor mechanical stability and susceptibility to breaking and collapse. The STEPS process provides a simple means to create mechanically reinforced nanostructures through either uniform conformal coating of these structures using the STEPS I process, or controlled increase of their basal size. Figure 21 shows the mechanical reinforcement of a microstructured array by shape transformation using STEPS methods. (122) The arrays of Y-shaped microposts in these SEM images were strengthened by either uniformly increased thickness following conformal PPy deposition, STEPS I (Figure 21a), or by increased base thickness following STEPS II (Figure 21b). In the latter case, the structures become tapered in cross-section and have increased width at the bottom to resist bending stresses.

We used an Agilent G200 nanoindentation system to compare the structural deformation of the original Y-micropost structure (Figure 21c, left) and incrementally reinforced microstructures. The cell-centered 10 mN nanoindentations were applied with a standard Berkovich tip. Figure 21c shows that permanent deformation sharply decreased as the structure was reinforced. Figure 21d shows finite element method (FEM) simulations to model the structural response of the epoxy replicas of the original Y-micropost and a STEPS-reinforced Y-micropost. A 5- $\mu\text{m}$ -tall original Y-micropost structure with arm length of 4  $\mu\text{m}$  and a width of 1  $\mu\text{m}$  was modeled using COMSOL FEM software. The tapered Y-micropost structure was 2  $\mu\text{m}$  wide at the bottom and tapered to a 1  $\mu\text{m}$  at the top. We assumed a uniformly distributed compressive load of

100 MPa for both structures, using the material properties of UV-cured epoxy resin. The tapered micropost structure shows a two-fold decrease in the maximum induced stresses compared to that of the original Y-micropost. The array of Y-shaped microposts was specifically used here to demonstrate the range of characteristic features of the shape evolution in the STEPS process. Among other properties, it provides a good example of the transformation of isolated columns into a closed-cell structure with interconnected walls.

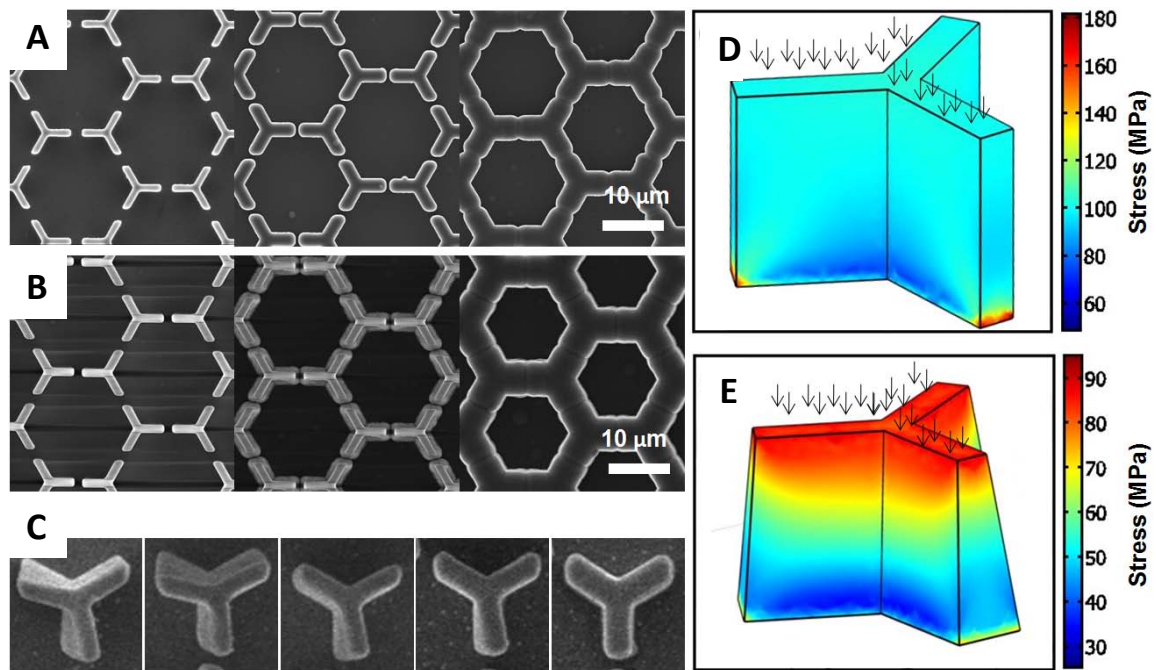


Figure 21. SEM images showing mechanical reinforcement of a microstructure by shape transformation using STEPS methods. All the images are of epoxy replicas of STEPS-modified structures. (a) Increasing the thickness of the structure using sputter coated metal electrodes. (b) Formation of a tapered cross-section using evaporated metal electrodes. (c) Comparison of the mechanical stability of epoxy replicas of the original structure (left) and incrementally reinforced microstructures (from left to right) following a series of cell-centered 10 mN nanoindentations with a Berkovich tip. (d, e) FEM simulations for an original microstructure, (d) and a STEPS-modified, tapered

Figure 21 (Continued)

microstructure, (e) under a distributed compression loading of 100 MPa. Height = 5  $\mu\text{m}$ , Arm = 4  $\mu\text{m}$ , Width = 1  $\mu\text{m}$ . STEPS-reinforced tapered structure shows a two-fold decrease in the maximum induced stress compared to the original structure.

### **C. Atomic force microscopy (AFM) for single-structure measurements of engineered polymeric nanostructures**

Taking a cue from atomic force microscopy (AFM) measurements of nanowire bridges and cantilevers (123-125), we have applied AFM to perform the single-structure mechanical measurements of our engineered fibers. We have developed a sample preparation method in which the test fibers are oriented horizontally so that the AFM cantilever can accurately apply z-direction bending forces. Spring constant calibration was performed for each cantilever used, allowing the mechanical properties of an individual fiber to be probed. Specific test locations were programmed along with open or closed loop test parameters.

### **D. Validation of AFM-based mechanical characterization**

To validate AFM-based single fiber measurement, we first tested the bending stiffness of HAR silicon nanoposts ( $h = 6.8 \mu\text{m}$ ,  $r_{\text{base}} = 150 \text{ nm}$ ,  $r_{\text{tip}} = 90 \text{ nm}$ ), shown in Figure 22A. By testing silicon, a very well characterized material, we sought to compare the empirical and analytical bending behavior. As noted above, Euler beam mechanics predicts an inverse cubic relationship between the bending stiffness of a cantilever and the length at which a force is applied (Figure 22B, inset). The empirical stiffness-length curves are plotted in Figure 22B, yielding a power relationship of  $-3.06 \pm 0.2$ , highly

consistent with the analytical value. In addition, the measured effective stiffness of the silicon nanopost was consistent with its geometry from SEM images and its elastic constants. Thus the AFM characterization method has been shown to be viable and accurate, opening new avenues to measure the dynamic and nonlinear mechanical properties of bioinspired nanoposts.

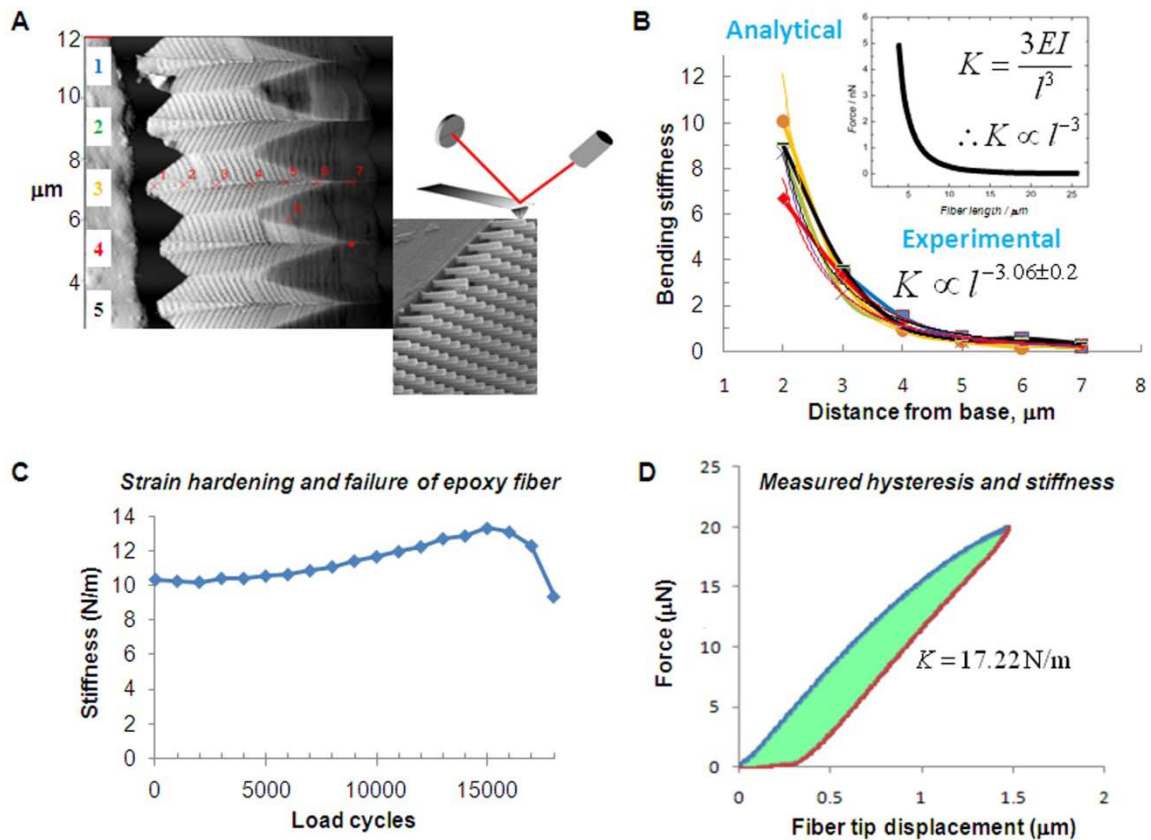


Figure 22. Empirical characterization of nanopost mechanical properties. (A) Sample preparation for single fiber measurement by AFM and scan of five silicon nanofibers ( $h = 6.8 \mu\text{m}$ ,  $r_{\text{base}} = 150 \text{ nm}$ ,  $r_{\text{tip}} = 90 \text{ nm}$ ). A cross-section is mounted at 90 degrees such that the AFM cantilever tip can test the mechanical properties of single nanofeatures in bending. The contact-mode scan shows the  $1 \mu\text{m}$  interval locations along five silicon nanofibers where force and displacement were measured to validate mechanical characterization by AFM in reference to Euler beam theory. (B) Empirical best-fit



Figure 22 (Continued)

effective stiffness curves for 1  $\mu\text{m}$  interval locations along the lengths of the five silicon nanofibers. These curves show an average decay of power  $\sim 3$ , in excellent registry with the inverse cubic relation of effective stiffness to cantilever length in the analytically predicted curve (inset). This helps confirm that the AFM-based single nanofeature characterization approach is viable and accurate. (C) The fatigue life of a single epoxy fiber ( $l = 9.0 \mu\text{m}$ ,  $r_{\text{base}} = 1.05 \mu\text{m}$ ,  $r_{\text{tip}} = 0.85 \mu\text{m}$ ), important for long-term applications, is characterized by AFM. The nanofiber monotonically increases in stiffness by 30.6% over 15,000 load cycles applied at 16 Hz and 91  $\mu\text{m/s}$ , consistent with strain hardening behavior, which decreases its sensitivity. After this point the stiffness rapidly drops off and structural failure occurs. (D) Using AFM characterization, the effective stiffness of HAR epoxy microfibers is measured to be 17.22 N/m, and the hysteresis of the load-unload curve is measured, highlighted in green. Such minor hysteresis of 32% reveals that epoxy nanofibers are primarily elastic in their behavior in this bending range.

### **E. Application-critical dynamic mechanical properties: strain hardening, fatigue, viscoelasticity**

Unlike effective stiffness, a number of application-critical aspects of our polymer nanoarrays are difficult to predict *a priori*. Fatigue life and strain hardening at the micro/nanoscale, for example, should be measured empirically (126-127), and these have critical bearing on application fitness. For example, synthetic cilia and neuromasts must flex constantly in performing their function, but their sensitivity would change with time in the case of strain-induced stiffening or accumulation of fatigue damage. The performance characteristics would therefore drift over the operating lifetime of the nanoarray, which itself is expected to be finite.

We cyclically deflected and relaxed a square epoxy microfiber ( $l = 9.0 \mu\text{m}$ ,  $r_{\text{base}} = 1.05 \mu\text{m}$ ,  $r_{\text{tip}} = 0.85 \mu\text{m}$ ) by AFM tip and tracked its effective stiffness evolution, shown in Figure 22C. A maximum tip displacement of  $0.8 \mu\text{m}$  from the initial position was maintained in each load cycle. The fiber was found to increase monotonically in effective stiffness from  $10\text{N/m}$  by  $30.6\%$  over  $15,000$  load cycles (applied at  $16 \text{ Hz}$  and  $91 \mu\text{m/s}$ ), consistent with strain hardening behavior. After this point the stiffness rapidly dropped off, indicating structural failure. From our empirical characterization it is apparent that (1) the force sensitivity of epoxy HAR  $\mu$ -structures will decrease over time; (2) alternatively, more energy will be needed to sustain a given displacement; and (3) epoxy nano/microfibers are subject to fatigue failure after an order of  $10,000$  cycles at  $16\text{Hz}$ . These empirical properties are critical to consider in suitability assessment for different applications.

An additional nanofiber response property that is difficult to predict is viscoelasticity. A large relaxation time and hysteresis in the load-unload cycle would limit the frequency of stimuli that can be detected in sensor applications, for example, and high-speed assembly or actuation would require more energy. Applying our AFM characterization to a slightly thicker epoxy nanofiber that measured  $17.22 \text{ N/m}$ , we were able to characterize its load-unload behavior (Figure 22D). The area highlighted in green depicts the hysteresis loop for a force curve of  $20 \mu\text{N}$  (max deflection =  $1.5 \mu\text{m}$ , rate of deflection =  $6 \mu\text{m/s}$ ). This hysteresis of  $32\%$  of work done reveals that epoxy nanoposts are still primarily elastic over this bending range. At higher load frequencies, however, the hysteresis will of course increase and should be considered in the application context.

## **5. Biofilm culture and quantification methods for study of antifouling structured surfaces**

### **A. Sonication, dispersal, and colony forming unit (CFU) assay**

The attached bacteria or biomass on various polymer samples was quantified using a multi-step process of cell removal, serial dilution, and plating for viable cell counts, as shown in Figure 23. (128) First, each polymer sample was individually placed into a 50 mL conical tube containing 15 mL of 3 mM D-tyrosine in PBS at pH 7.5 and incubated at room temperature for 30 minutes to promote biofilm disassembly. The samples were bath-sonicated for 10 minutes. 200  $\mu$ L of each sonicated solution was pipetted into a 96-well plate and serially 10-fold diluted. 10  $\mu$ L of each serial dilution of each sample were pipetted in parallel onto an LB agar plate, which was briefly tilted to spread the drops into parallel lines and was then incubated for 36-48 hours at room temperature or for 24 hours at 37 °C for counting. Bacterial colony forming units (CFU), individual bacteria that reproduce into visible colonies, were counted on each plate and the CFU values were compared at corresponding dilution factors.

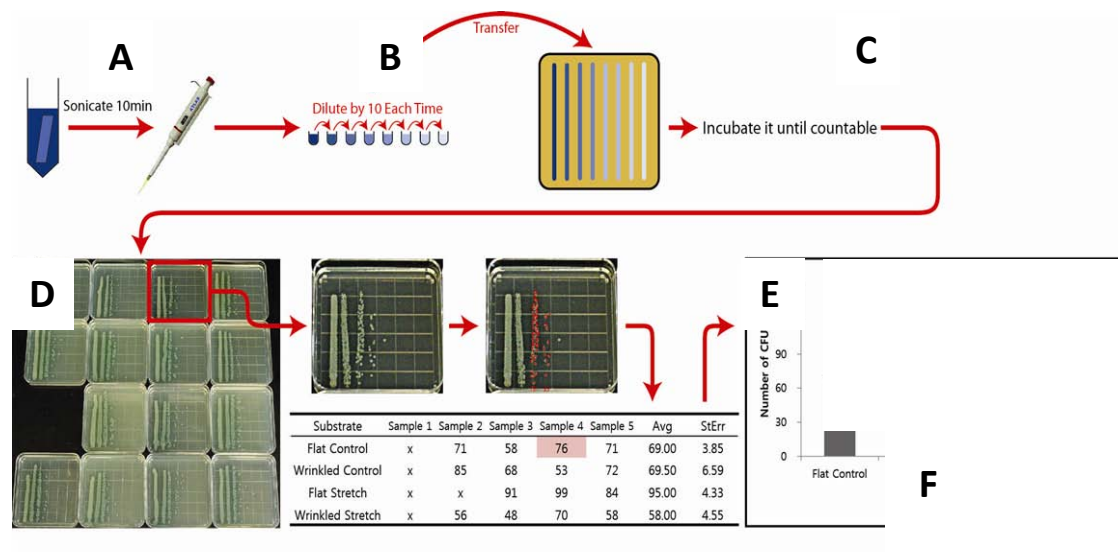


Figure 23. Colony-forming unit method of biofilm quantification. A substrate with associated bacterial biofilm is (A) incubated in phosphate buffered saline prior to bath sonication. (B) Serial tenfold dilution of the liquid in which the substrate is sonicated allows screening of 8 orders of magnitude of concentration on square agar plates (D). CFU are counted (E) and compared at the dilution factors that result in a value range of ~10-100, and the data are tabulated for analysis (F).

## B. Fluorescence microscopy and post-processing

For fluorescence imaging of attached bacterial cells, substrates with associated biofilm were gently rinsed in phosphate buffered saline (PBS) (1x) (Lonza Biowhittaker), and the adherent bacteria were fixed by 5% glutaraldehyde solution for at least 1 h. Following another PBS rinse, 0.01% Triton X100 in PBS (PBST) was used to permeabilize the bacteria membranes over 15 min, after which the cells were stained with 0.5  $\mu$ M SYTOX green nucleic acid stain (Invitrogen) in PBST for 30 min, after which they were placed in a dish filled with PBS for fluorescence imaging. (128) Imaging was performed on a Leica DMX microscope. To analyze the fluorescence intensity of

micrographs, the average intensity image of a sample's micrograph set was generated in ImageJ and the average  $[(R+G+B)/3]$  pixel value and standard deviation were computed for each average intensity image. To analyze the ordering present in different fluorescence micrographs, Fast Fourier Transforms (FFT) were performed and contrast-optimized using ImageJ.

### **C. Scanning electron microscopy imaging**

For SEM imaging, samples were fixed for 1 hr in 5% glutaraldehyde, serially dehydrated for 1 hour in each of 25%, 50%, and 75% ethanol/deionized water, followed by dehydration overnight in absolute ethanol. Samples were then CO<sub>2</sub> critical-point dried in a Tousimis autosamdri 815B, sputter coated with ~10 nm gold, and imaged on a JEOL JSM-6390LV scanning electron microscope.

### **D. Crystal violet staining and spectrophotometry**

Substrates with associated biofilm were removed from the respective experimental setup, gently rinsed in PBS, and stained by 0.1% crystal violet for 20 min. (129) The stained samples were rinsed in a DIW bath and the bound crystal violet was eluted from each sample into 4 mL of 100% EtOH. Absorbance values at 590 nm of the resulting EtOH solutions were measured on a Perkin Elmer Lambda 40 UV-Vis spectrometer.

### **E. Bacterial biofilm culture protocols**

Bacterial precultures were prepared by suspending a scraped colony from an agar plate into 10 mL LB (EMD LB Broth Miller) in loosely capped tubes and incubating in

an orbital shaker (200 rpm, 37 °C) for 18-22 h, to the stationary phase. *Pseudomonas aeruginosa* PA-14, *Staphylococcus aureus* MN8 and *Escherichia coli* W3110 strains were used. For each species, 1% initial seeding concentration of preculture was respectively added to the following biofilm-promoting growth media: TB (BD Bacto Tryptone), TSB supplemented with 0.5% glucose and 3% NaCl, and M9 minimal medium supplemented with 0.2% Casamino Acids and 0.5% Glycerol. Experiments performed in six-well plates were static benchtop and performed at room temperature.

## 6. Dynamic structured surfaces for control of biofilm attachment<sup>4</sup>

In contrast to surface-chemistry based antimicrobial approaches, the effects of topographical features on bacterial adhesion and biofilm formation are poorly understood. Nature provides some clues to preventing microbial colonization of surfaces by this alternative strategy. For example, ship hulls constantly amass layers of algae and crustaceans. Yet materials with topographical features mimicking the skin of sharks have shown increased resistance to marine biofouling at certain length scales. (78) Physical structures may provide a more persistent form of inhibitive interaction between bacteria and surfaces. Indeed, mammalian cells respond to surface topography and mechanics and their behavior can be manipulated using only spatial and mechanical cues. (82-84) Bacteria have also been reported to respond to mechanical cues. Surface attachment is an integral step in biofilm formation and impacts chemical signaling pathways between and within bacterial cells. (85) Substrate elastic modulus, for example, has been suggested to affect the density of surface colonization. Specifically, on flat surfaces in the Young's modulus range of 1 to 100 MPa, a positive correlation is reported between attachment density and surface modulus. (130) Topographical features can influence the arrangement and the resulting behavior of cells on surfaces and may affect biofilm development. (86) However, the roles of specific surface structures in modifying bacterial attachment and subsequent behavior—particularly the role of geometric parameters relative to the mechanical properties of the surface structures—remain unclear.

---

<sup>4</sup> These results are published in *Nanotechnology* [doi 10.1088/0957-4484/22/49/494007] and in forthcoming publications in *Proc. Nat. Acad. Sci.* and in *New J. Physics*.

Here we first present new findings on the interactions governing bacterial assembly on nanopost substrates. The attachment and biofilm accumulation behavior were studied by altering the symmetries, dimensions, and pitch (center-to-center distance) of nanopost arrays using a combinatorial approach. Additionally, the attachment of bacteria to nanostructured substrates as a function of the effective stiffness was investigated and compared to the attachment to flat, unpatterned surfaces. Rather than rely on intrinsic material modulus, we exploit a derived effective stiffness, dependent on both the material and geometric properties of the surface, to direct bacterial adhesion and to affect biofilm growth. Actively dynamic actuation of the microstructured surface is then introduced, and finally a liquid-based dynamic surface is investigated.

## **A. Passive structures**

### **I. Robust control of bacterial patterning and contact mode by tunable interstitial spacing and symmetry**

The replication method used to fabricate the polymer high-aspect-ratio (HAR) nanopost substrates can be modified to create post arrays with a range of dimensions and symmetries from the same elastomeric molds. (131) Applying precise sets of deformations to the elastomeric molds while the replica material is cured in them allows nanopost cross-sections to be proportionally elongated, nanoposts to be tilted away from the vertical axis, and the array to be transformed from square to rectangular or rhombic. Additionally, substrate curvature or twist can be introduced. These substrate



modifications are possible either through simultaneous mold deformations or through iterative mold deformation and replication steps.

In particular, the four-fold symmetry of the square post array used in pitch gradient samples can be broken by uniaxial extension of the mold during the substrate curing step. In this manner, the square post array is transformed into a rectangular array, where the post pitch is expanded in one lattice direction and contracted in the orthogonal direction due to Poisson compression (Figure 24a). Previous work demonstrated the spontaneous assembly of bacteria on periodic post arrays and suggested a model for bacterial patterning by surface contact area maximization. (86) With this principle in mind, we designed substrates to align bacterial adhesion on surfaces using only topographical cues.

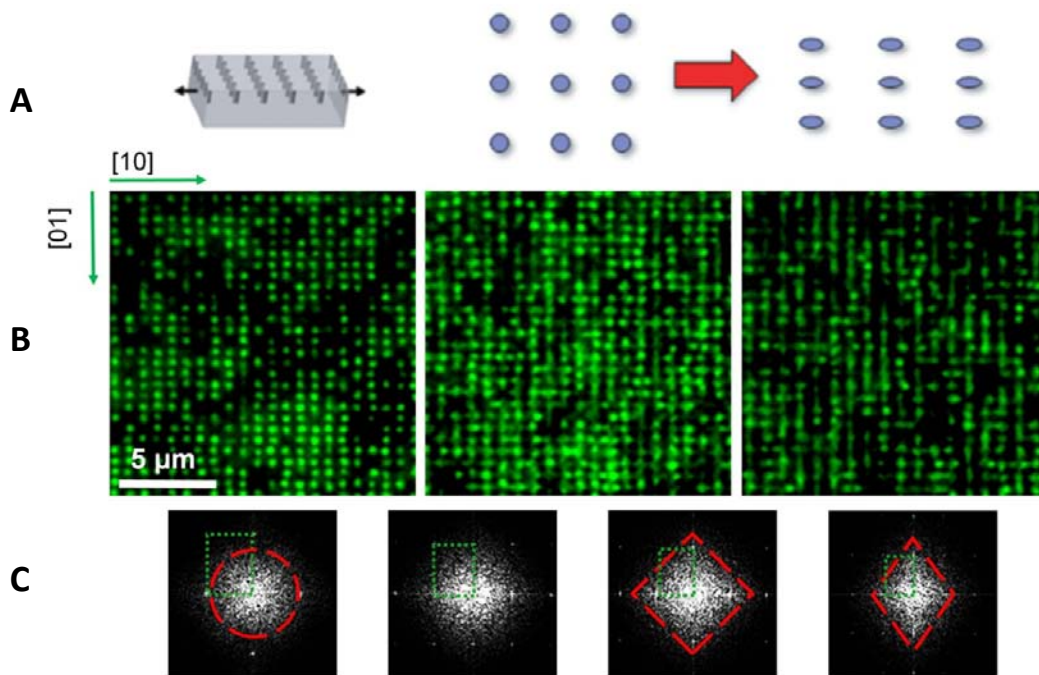


Figure 24. Preferential bacterial attachment in anisotropic environment. (a) Schematic of uniaxial elastomeric mold stretching and the resultant nanopost array transformation from

Figure 24 (Continued)

square to rectangular symmetry. (b) Fluorescence images of *P. aeruginosa* bacteria following 18 hour growth on nanopost substrates with rectangular symmetry and increasing pitch in both directions from the left image to the right one. The vertical [01] lines of bacteria in the rightmost image are consistent with surface contact area maximization as a driver for spontaneous attachment. (c) From left to right, Fourier transforms of rectangular high-aspect-ratio nanopost arrays show the induced directional patterning of bacteria by surface structure periodicity alone. The elongation of the central spot indicates that bacteria preferentially lie along the [01] direction.

Using uniaxial extension of a surface with square symmetry and a spatial post pitch gradient across the substrate during the curing step, we generated a rectangular post array with spatially varying pitch along both lattice parameters. *P. aeruginosa* was cultured on these anisotropic HAR nanopost arrays, and their self-assembled patterns were observed by fluorescent microscopy (Figure 24b). Consistent with previous results (86), the bacteria attach in different configurations depending on the pitch of the posts. At the small-pitch extreme (0.9  $\mu\text{m}$ ) the bacteria align themselves with the posts, oriented normal to the substrate, forming a rectangular array on the surface. As the post pitch increases the bacteria align themselves in the orthogonal directions of symmetry of the array by lying in the plane of the substrate.

The organizational characteristics of the bacterial patterns are more clearly seen in the Fourier transforms (FFT) of the fluorescence intensity images (Figure 24c). The small points correspond to positional ordering peaks and the anisotropy of the diffuse central spot corresponds to the orientational ordering of the rod-like cells. The positional ordering peaks are spaced at larger distances along the [01] vertical direction

(corresponding to smaller post spacing in real-space) than in the [10] horizontal directions, indicating cellular registration with the rectangular post symmetry. Within the closely spaced posts, where the cells align normal to the substrate, the positional ordering peaks reflect the rectangular symmetry of the bacterial pattern, but the central spot is isotropic. This lack of orientational order in the FFT image is a result of the fact that the cells are oriented parallel to the angle of viewing, and when viewed along their long axis, the rod-like cells lack orientational anisotropy. Moving across the substrate, as the posts get farther apart, the positional ordering peaks get correspondingly closer together, and the central spot becomes anisotropic as the cells lie in the plane of the substrate and normal to the viewing angle. Further across the pitch gradient, there is a point at which bacteria can bridge neighboring posts along the contracted [01] direction but can no longer do so along the stretched [10] direction of the array. Due to their contact area maximization behavior, the bacteria preferentially lie in the contracted direction, as can be seen by the vertical lines in the fluorescence image (Figure 24b) and in the anisotropic stretching of the central spot in the same direction (Figure 24c). This uniaxial orientational ordering confirms that the bacteria adopt specific and robust configurations when adhering to the substrate and demonstrates the influence of surface topography on bacterial assembly.

Several experiments used a combinatorial substrate of posts in an array of square symmetry with a variation of the pitch of posts from one end of the substrate to the other. To make the rectangular symmetry post array with a pitch gradient, a replica was made from a uniaxially stretched PDMS mold of a square array pitch gradient pattern. The

mold was stretched and the epoxy was cured on the stretched mold. The array consisted of posts having a diameter of about 300 nm and a height of about 2  $\mu\text{m}$ .

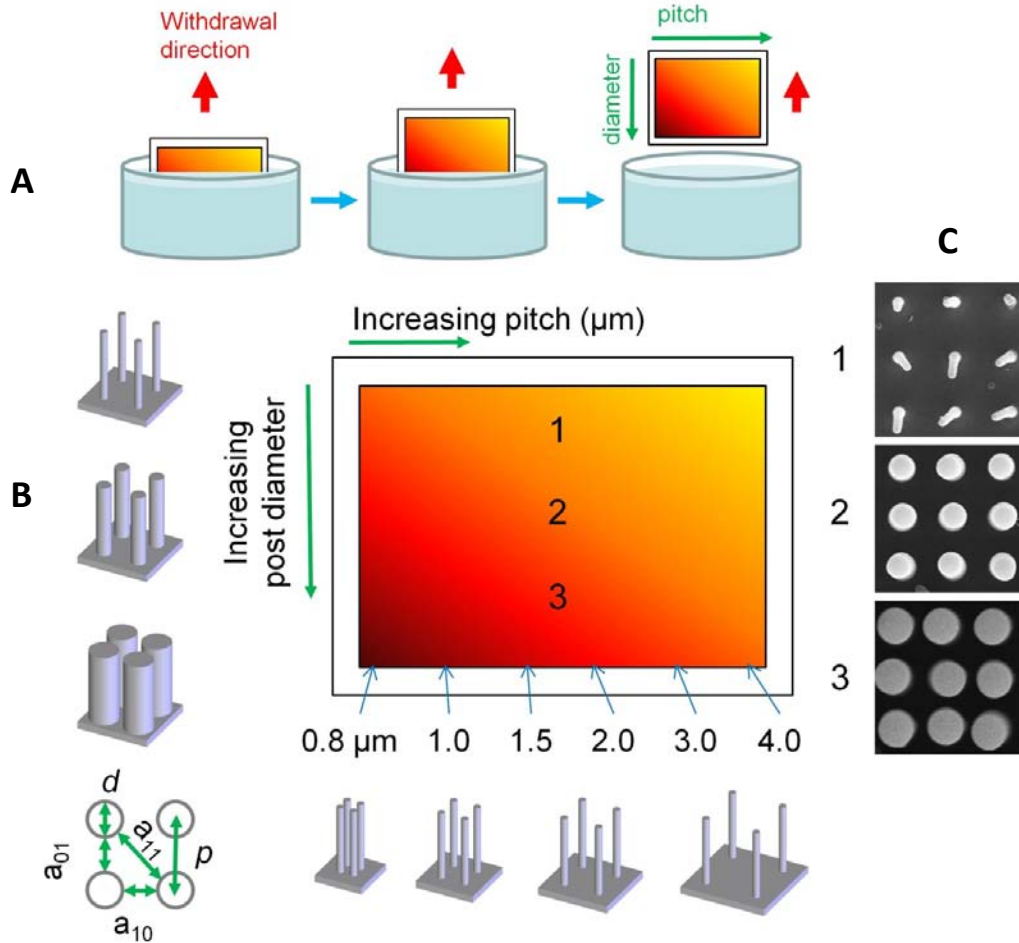


Figure 25. Schematic of the orthogonal double gradient substrate fabrication, adapting the recently described STEPS method [30]. (a) A high-aspect-ratio nanopost array with a pitch gradient from left to right in the orientation shown above was withdrawn in discrete steps in the perpendicular direction from the electrodeposition bath, resulting in discrete increases in nanopost diameter from the top of the substrate to the bottom. This substrate was then replicated multiple times using a fast double-molding method [29]. (b) The final combinatorial substrate includes both a pitch ( $p$ ) gradient from 0.8  $\mu\text{m}$  to 4.0  $\mu\text{m}$  and an orthogonal nanopost diameter ( $d$ ) gradient from 300 nm to  $\sim 1 \mu\text{m}$ . The interstitial spaces  $a[10]$  and  $a[01]$  are respectively the difference of  $p - d$  in the  $[10]$  and  $[01]$

Figure 25 (Continued)

directions. (c) Top-down SEM images of the double gradient nanoarray at three locations with  $p = 1.66 \mu\text{m}$ . The thin nanoposts at location 1 appear bent because they are flexible.

Post substrates with orthogonal post pitch and diameter gradients were fabricated using the STEPS method described previously. (122) An epoxy (UVO-114) replica of a nanopost array, containing a pitch gradient from 4.0 down to 0.9  $\mu\text{m}$  across the substrate, was sputter coated with 50 nm of Au to make the surface electrically conductive. The gold-coated sample was then 80% submerged into an electrochemical cell with 0.1 M pyrrole monomer and 0.1 M sodium dodecylbenzenesulfonate as electrolyte. Potentiostatic (0.55V vs. Ag/AgCl) electrodepositions of polypyrrole were employed with stepwise withdrawal of the sample in the direction perpendicular to the pitch gradient in four equal, discrete steps at  $t = 15, 30, 45,$  and 60 minutes (Figure 25). Between time points the sample was stationary with 30 minutes of equilibration and drying time. Since the withdrawal direction was perpendicular to the pitch gradient, an orthogonal gradient of nanostructure diameter corresponding to the PPy growth time was obtained.

Polymer replicas consisting of square post arrays were also fabricated from UVO-114, NOA 61, and NOA 65 – to vary substrate stiffness – by curing under UV lamps at 130  $\text{mW}/\text{cm}^2$  for 20, 60, and 60 minutes respectively. These arrays had dimensions of 2  $\mu\text{m}$  pitch, 250 nm diameter, and 8  $\mu\text{m}$  tall posts with a projected area of 4  $\text{cm}^2$ . Flat substrates of equal area were fabricated from the same polymers to serve as controls.

The Young's moduli of the NOA 61 and NOA 65 polymers were determined by the four-point flexure method described in Chapter 3D, except that the flexure samples were fabricated, in triplicates, with the following dimensions: length = 40 mm, width = 5

mm, thickness = 1.5 mm, and the mechanical measurements were performed on an Instron 5566 universal test system.

By precisely controlling the topography of the post array, we further demonstrate the ability to drive long-range bacterial assembly from a disordered to an ordered state and vice versa. Starting with a HAR nanopost array that had been fabricated with a pitch gradient, we have fabricated a unique two-dimensional gradient substrate by adapting the Structural Transformation by Electrodeposition of Polymers (STEPS) technique (122), as shown in Figure 25a. A gradient of nanopost diameters was thus superimposed in the orthogonal direction, creating a 2-D combinatorial array as shown in Figure 25b. Epoxy replicas of the combinatorial array were then fabricated using a double-casting soft lithography method. (132) *P. aeruginosa* cultures were grown to 18 hours on the epoxy replicas, and the resulting attachment was studied along the pitch and diameter gradients of the substrate by fluorescence microscopy. Pronounced effects of both post pitch and diameter on the mode of bacterial attachment were observed.

For large-pitch regions of the array, increasing nanopost diameter drives the bacterial patterning to order, first in the [01] and [10] in-plane directions on the substrate, and with further increased diameter, the bacteria begin to orient normal to the substrate. This result recapitulates the effect of decreasing post pitch, showing that the wall-to-wall gap (pitch minus diameter), rather than the pitch or diameter per se, is the critical ordering parameter. The in-plane configuration is maximized with a gap of approximately  $a_{10} = 0.90 \mu\text{m}$ . Correspondingly, the bacteria attaching on a region of the substrate with smaller pitch were observed to first pattern in the [01], [10] arrangement, then assemble into the out-of-plane configuration with increasing diameter; diameter-

pitch combinations producing a [11] gap dimension of about 1.05  $\mu\text{m}$  maximize this configuration. Finally, the bacteria attachment becomes random and disordered as the spacing between posts further diminishes. At this point, the interstitial space is insufficient for the cells to insert between nearest neighbor posts. Conversely, no orientational ordering results from combinations of pitch and native diameter in which

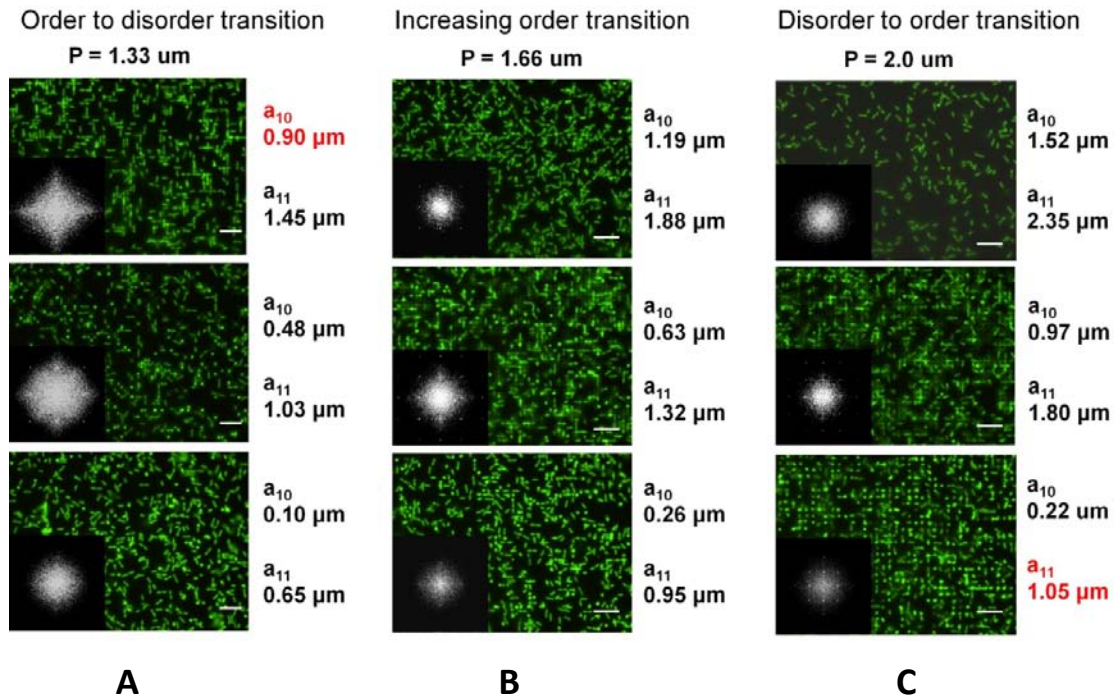


Figure 26. Fluorescence images and corresponding Fourier transforms of spontaneously patterned *P. aeruginosa* bacteria on the combinatorial nanoarray substrate. The image sequences show attachment along regions of equal pitch and increasing diameter, from top to bottom. The interstitial spacing, not center-to-center pitch, of the HAR nanoarray is the functional parameter of the substrate for spontaneous bacterial patterning on the surface. By precisely tuning nanoarray geometry, the effect can be controlled.  $P$  is center-to-center [10] spacing;  $a_{10}$  and  $a_{11}$  are wall-to-wall [10] and [11] spacing. (a) An order to disorder transition is induced as the  $a_{11}$  interstitial space is decreased to the point that bacteria can no longer insert between nearest neighbor nanoposts. (b) Initially in-plane bacteria transition to out-of-plane order as the interstitial space becomes optimized

Figure 26 (Continued)

for out-of-plane insertion. (c) Initially disordered bacteria transition to a high degree of order. Scale bars are 8  $\mu\text{m}$ .

the spacing is larger than the length of the bacterial cells, as expected from the contact area maximization behavior model. (86) The fluorescence microscopy images and corresponding FFTs in Figure 26a-c demonstrate these finely controlled transitions between order-to-disorder, increasing order, and disorder-to-order. Moreover, the length scale of the gap for optimal ordering closely correlates to the length scale of the bacterium, which is about 1  $\mu\text{m}$ . Therefore, by designing a HAR nanostructured substrate with the appropriate length scale interstices, bacteria can be induced to order in arbitrary patterns.

## **II. Effective compliance of HAR nanostructures and mechanoselective adhesion below threshold value**

In addition to controlling bacterial attachment to surfaces through the use of nanostructures and nanotopography, the mechanical properties of a surface have recently been reported to play a role (130). This phenomenon was demonstrated using flat surfaces in the Young's modulus range of  $\sim 1$  to  $\sim 100$  MPa and showed that there is a positive correlation between the density of attached bacteria and the substrate stiffness. The substrate stiffness in this case was modulated by the pH during fabrication of the polyelectrolyte multilayers. However, a bacteria-inhibitive material in the 1 MPa or



lower stiffness regime may not be practical for some technological or device applications due to low mechanical rigidity. A monolithic material rather than a surface coating would also not be susceptible to potential delamination. In this study, we use HAR surface nanoarrays comprised of the bulk material to emulate a thin, ultra-compliant surface coating. The nanopost dimensions were 2  $\mu\text{m}$  pitch, 250 nm diameter, and 8  $\mu\text{m}$  height. Bacteria near the nanoarray surface interact with highly flexible cantilevers rather than with a flat surface. The most flexible nanoposts in our study deflect  $\sim 5 \mu\text{m}$  per 100 pN of force applied to the tip perpendicular to the long axis of the post, based on Eulerian

beam mechanics:  $\delta = \frac{Fl^3}{3EI}$ , where  $\delta$  is the tip deflection,  $F$  applied force,  $l$  post height,  $E$

elastic modulus, and  $I$  moment of inertia. By comparison, for a bacterium to indent a flat surface  $\sim 5 \mu\text{m}$  per 100 pN, the elastic modulus would need to be  $\sim 5 \text{ Pa}$ . For this, we assume the 200 nm radius cells to apply force with their hemispherical poles and we use

the Hertzian elastic contact model for indentation:  $\delta = \left( \frac{4E}{3F(1-\nu^2)} R^{0.5} \right)^{2/3}$ , with  $\delta$  the

indentation depth,  $\nu$  Poisson's ratio,  $E$  elastic modulus,  $F$  applied force, and  $R$  indenter radius. By this analysis, the soft, hair-like surface attains effective stiffness (force per unit deflection or deformation) six orders of magnitude lower than the constituent polymers, which are themselves in the range of 20 to 2000 MPa, seven to nine orders of magnitude higher Youngs modulus than required for a flat surface.

Using the HAR nanoarray platform and a CFU biofilm quantification assay (see Experimental), we investigated the attachment density of bacteria on surfaces as a function of the nanoarray effective stiffness. The effective stiffness was controlled by selection of the polymer so as to keep the nanoarray geometry constant. Candidate

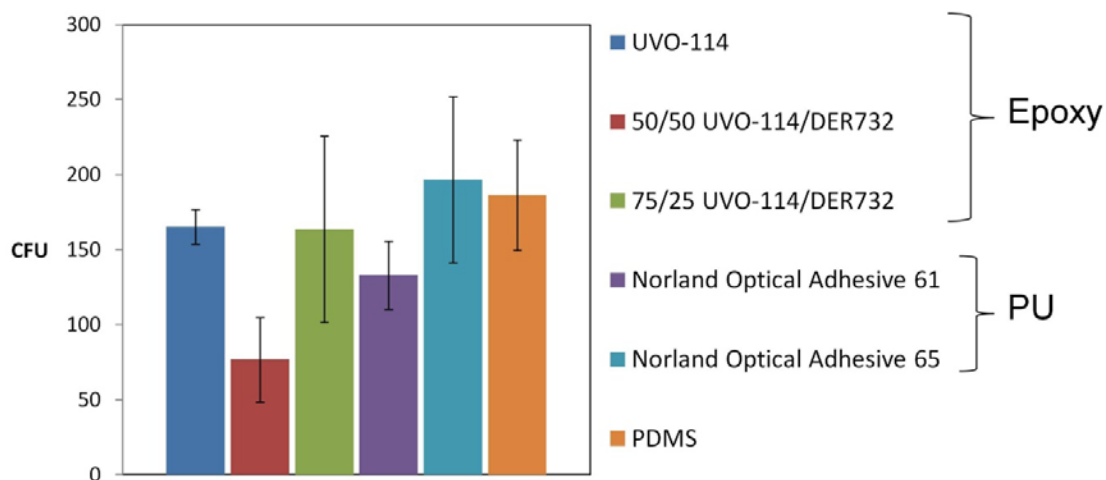


Figure 27. Leaching and toxicity screening performed using 20 nm Au-coated samples of a range of candidate polymers. UVO-114, NOA61, and NOA65 were selected for their low leaching/toxicity, based on high CFU counts, as well as for their photocurability and their range of modulus values. CFU were based on  $10^{-4}$  dilutions.

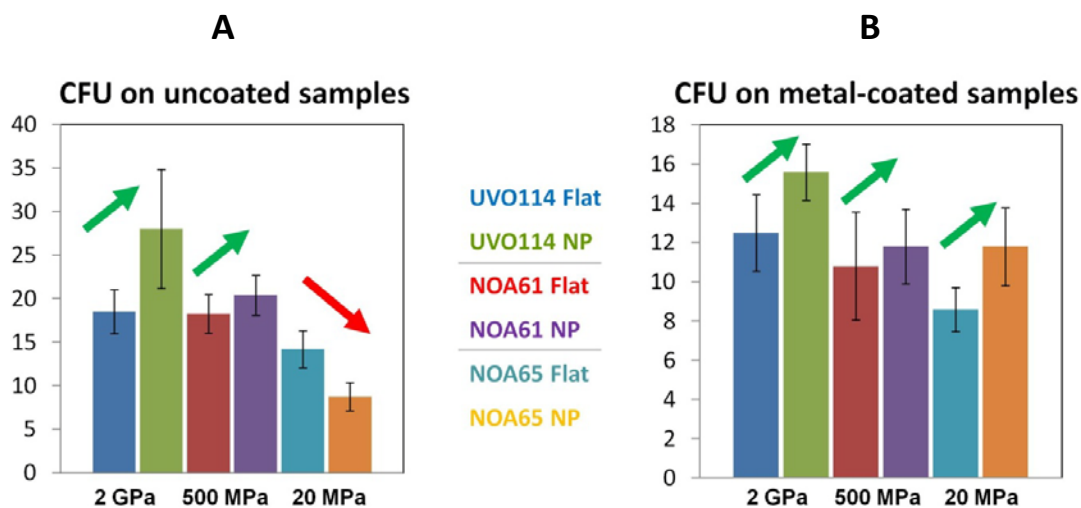


Figure 28. Colony forming unit (CFU) measurements of *P. aeruginosa* biofilm growth on both unpatterned and high-aspect-ratio (HAR) nanopost substrates fabricated from polymers of varying Young's modulus. (a) The UVO114 (2 GPa) and NOA61 (500 MPa) nanopost substrates show increased growth versus the unpatterned control substrates. However, a biofilm growth crossover regime with respect to the addition of HAR

Figure 28 (Continued)

nanoposts occurs in the softest polymer, NOA65. Despite a surface area increase, resultant biofilm decreases. (b) The crossover regime is not observed when a 20 nm gold coating is applied to the nanoposts, which increases their effective stiffness, indicating the upper bound of an effective

polymer systems were first screened for leaching toxicity to *P. aeruginosa*. Flat substrates made of each polymer were sputter coated with 20 nm Au to mask their native surface chemistry, and biofilms cultured on these substrates were quantified (Figure 27). The polyurethanes NOA65, 20 MPa; NOA61, 500 MPa; and the epoxy UVO114, 2000 MPa were selected for their low leaching toxicity (as measured by high viable cell counts), photocurability, and broad range of modulus values. The relative cytophilicity of each of these three polymers without sputtering was similarly determined, showing slight differences in CFU for biofilm growth inhibition. CFU were based on  $10^{-4}$  dilutions.

As seen in Figure 28a-b, the numbers of CFUs measured from 27-hour biofilms cultured on 2 GPa and 500 MPa nanoarrays were larger than on the corresponding flat surfaces. This trend may be expected based on the nanoarrays' larger surface area versus flat substrates. However, a biofilm growth crossover regime occurs for the 20 MPa NOA65 polymer nanoarray. On this ultra-compliant structured surface, despite the surface area increase, resultant biofilm actually decreases with respect to the addition of HAR posts. Since the material cytophilicities are similar, these results suggest that the extremely low effective stiffness experienced by cells interacting with the soft, hair-like surface inhibits biofilm accumulation. (By comparison, *P. aeruginosa* forms indistinguishably robust biofilm after 24 hours on a polymer surface regardless of the

surface chemical functionality, as seen in Figure 2, suggesting its indifference to surface chemistry alone.) Based on the flexible cantilever model of nanoarray effective stiffness discussed above, the minimum threshold for this mechanoselective behavior is on the order of 5  $\mu\text{m}$  surface deformation per 100 pN force—equivalent for a bacterium attaching to a flat surface with an elastic modulus of  $\sim 5$  Pa.

In contrast, the growth crossover regime is not observed once a 20 nm gold layer is applied to the same three polymer nanoarrays, as shown in Figure 28b. The estimated effect of the gold layer, whose modulus is 79 GPa, is to stiffen by about 20x the polymer-metal core-shell nanoposts. With this increase in the HAR nanoarray effective stiffness, the growth crossover in the 20 MPa polymer nanoarray is not observed, suggesting the upper bound of a biofilm growth inhibition range. These effective stiffness values are themselves lower estimates, as bacteria are in contact with not only the distal ends of the nanoposts, but also the geometrically stiffer basal ends, and indeed, with the basal plane. The “average” effective stiffness of these surfaces, at which the mechanoselective adhesion phenomenon occurs, can be assumed to be higher.

Regardless, the passively dynamic nature of such surfaces may present an unstable and unfavorable attachment target for bacteria. Their deformation under imposed bacterial forces can cause them to read as a fluid-like solid, whereas biofilms seek secure and immobile surfaces to colonize. Therefore, the principle of effective stiffness-mediated inhibition of bacterial attachment may constitute promising surface treatments in diverse applications for preventing biofilm accumulation.

By applying a novel combinatorial platform, we have elucidated key nanometer-scale geometric and mechanical parameters of surfaces that drive long-range bacterial

adhesion patterns and biofilm growth behavior. The interstitial spacing between surface features is experimentally confirmed to be the critical parameter controlling assembly, and it can be used to induce specific ordering phases using a range of feature sizes on the order of the bacterial cell. Furthermore, for the first time, the mechanoselective bacterial attachment of bacteria on compliant high-aspect-ratio nanostructures has been described. This extends the recent finding of bacterial mechanosensitivity to a much lower effective stiffness regime of  $\sim 50 \mu\text{m/nN}$ , equivalent to flat films with modulus as low as 5 Pa. Moreover, it suggests a completely new strategy to exploit mechanoselective adhesion. When the effective compliance of the hair-like nanoarray is increased beyond a threshold, biofilm growth is inhibited as compared to a flat control surface. As this is strictly a mechanical-structural property and does not rely on surface chemical functionalization, it is not susceptible to masking and may be persistent. As a potential new strategy, HAR nanoarrays mimicking an extremely compliant flat surface offer promise for diverse applications for controlling and inhibiting biofilm accumulation.

## **B. Mechanical actuation**

The persistent antifouling properties of a range of biological surfaces with active topographic features have been described. Nature provides some clues to preventing microbial colonization of surfaces by this alternative strategy. For example, while ship hulls constantly amass layers of algae and other microorganisms, materials with topographical features mimicking the skin of sharks have shown increased resistance to marine biofouling at certain length scales. (78) In this case, the shark is in constant motion, and the skin's structures are static. Conversely, the skins of sedentary marine

organisms known as echinoderms, e.g., star fish and sea urchins, are densely decorated with spiny, constantly moving microstructures known as pedicellaria that prevent larvae and microorganisms from attaching to the skin. (79-81) Such mechanical frustration of dynamic, physical structures may provide a more persistent and nontoxic form of inhibitive interaction between bacteria and surfaces. Indeed, bacterial cells are already known to respond to surface topography and mechanics, and their behavior can be manipulated using only spatial and mechanical cues. (82-84) Surface attachment is an integral step in biofilm formation that impacts chemical signaling pathways between and within bacterial cells. (85) Dynamic topographical features may influence the arrangement and the resulting behavior of cells on surfaces and affect biofilm development. (86) Yet, the strategy of mechanical frustration--and the role of topographic parameters with respect to surface motion parameters—has not been applied or studied in a synthetic surface as a potential nontoxic solution for controlling bacterial biofilm attachment.

Here we report on the development and capability of a synthetic platform inspired by the echinoderm skin to reduce and control bacterial biofilm attachment. The surface in our setup was based on polydimethylsiloxane (PDMS) elastomer with microscale wrinkle topography and on cyclic uniaxial stretching of this surface, which induces sharp transformations of the topography during the extend-release cycle. Bacterial biofilm attachment to the dynamic substrates was studied under a matrix of parameters, including the mechanical strain amplitude and timescale, surface topography length scale, bacterial species and cell geometry, and growth time. The optimal conditions for achieving up to ~80% *Pseudomonas aeruginosa* biofilm reduction after 24 hr growth and 62% after 48 hr

growth were determined through a matrix of experiments. At the same time, divergent effects on the attachment of *P. aeruginosa*, *S. aureus*, and *E. coli* biofilm showed that the dynamic substrate also enables an effective new means of species-specific biofilm inhibition--or selection for a desired type of bacteria—without reliance on any toxic or transient surface chemical treatments.

### III. Uniaxial tensile instrument overview

The mechanical frustration strategy of echinoderms' nonfouling skin was adapted in the simplified form of a uniaxially stretching elastic surface, as schematically shown in Figure 29a. By using an elastomer, the substrate can be cyclically extended and relaxed over time without material degradation. When the substrate is stretched in one direction, it also contracts in the perpendicular directions, due to the Poisson ratio of an elastomer.

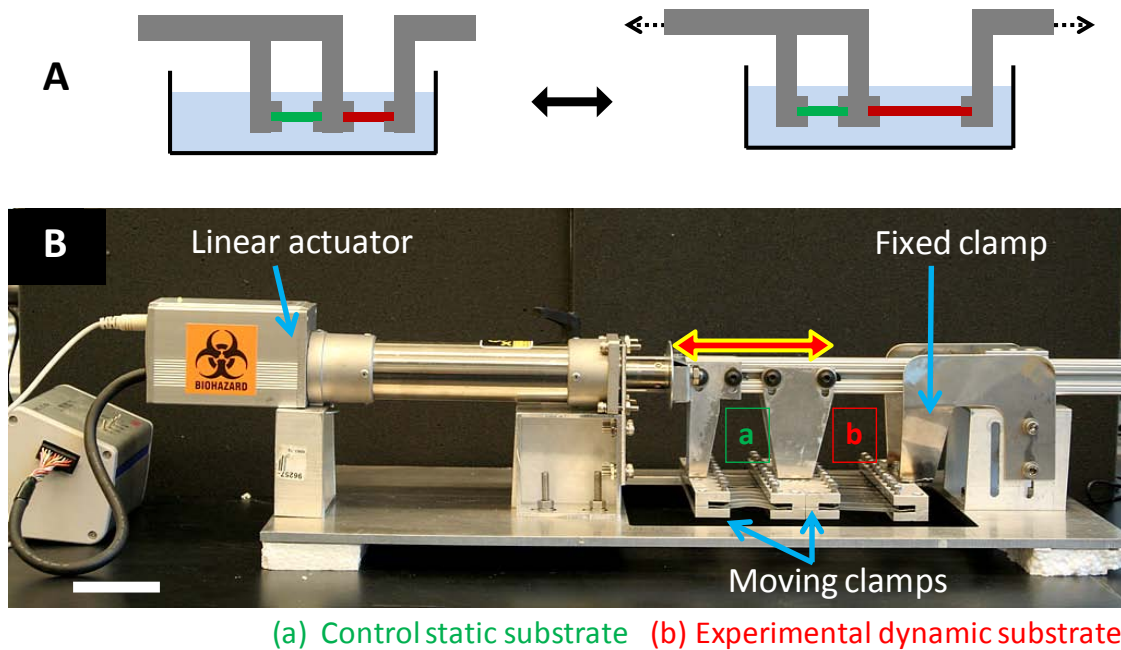


Figure 29. The experimental setup for biofilm growth on dynamic surfaces. (a) Uniaxial strain applied to an elastomeric substrate as a simple bioinspired dynamic surface. (b) A

Figure 29 (Continued)

uniaxial tensile instrument was fabricated allowing 20 elastomeric samples to be tested simultaneously. A laptop combined with a logic controller are capable of driving continuous cyclic strain as well as step waveforms (incorporating pauses), and control of strain amplitude and rate. Custom-made grippers independently clamp both static (control) and dynamic substrates submerged in bacterial culture (not shown) during a growth experiment. Scale bar = 5 cm.

analogous to the moving pedicellaria of the echinoderm, points on the surface of the dynamically strained elastomer move relative to each other during a stretch-release cycle. The biocompatible elastomer polydimethylsiloxane (PDMS), with an elastic deformation limit of 300%, was chosen for this study. (133)

A custom-made uniaxial tensile instrument was fabricated and assembled, allowing 20 elastomeric substrates—10 static and 10 dynamic--to be tested in parallel for attachment of bacterial biofilm. A laptop with “RCPC” control software (IAC) and a programmable logic controller (Moeller easy512 AC-RC) drove an IAC linear servo actuator with 100 N force capacity. Both continuous cyclic strain as well as step waveforms incorporating arbitrary pauses (dwell time) could be produced. The instrument could also be programmed to vary the strain magnitude and rate (i.e., velocity of the grippers). As shown in Figure 29b, the overhead traveling rail carried two sets of movable gripper arrays, in addition to a fixed gripper array attached to the base of the instrument. When clamped in the grippers, the exposed length of each 1 x 5 cm elastomer substrate was 3 cm, and this length was considered to be 0% strain. To expose substrates to biofilm attachment during experiments, the substrate grippers were submerged in a



glass container with bacterial culture. The container was set atop a magnetic stir plate and a stir bar in the container gently mixed the liquid.

## IV. Bottom-up dynamic elastomeric wrinkles

### 1. Wrinkling mechanism, characterization, and control

Polydimethylsiloxane (PDMS) that is treated with oxygen plasma while elastically stretched can generate highly regular and controllable parallel “wrinkle” topography upon release. This effect is a result of the very thin silica layer that forms on the surface of PDMS, which is stiffer than the elastomer and buckles under longitudinal

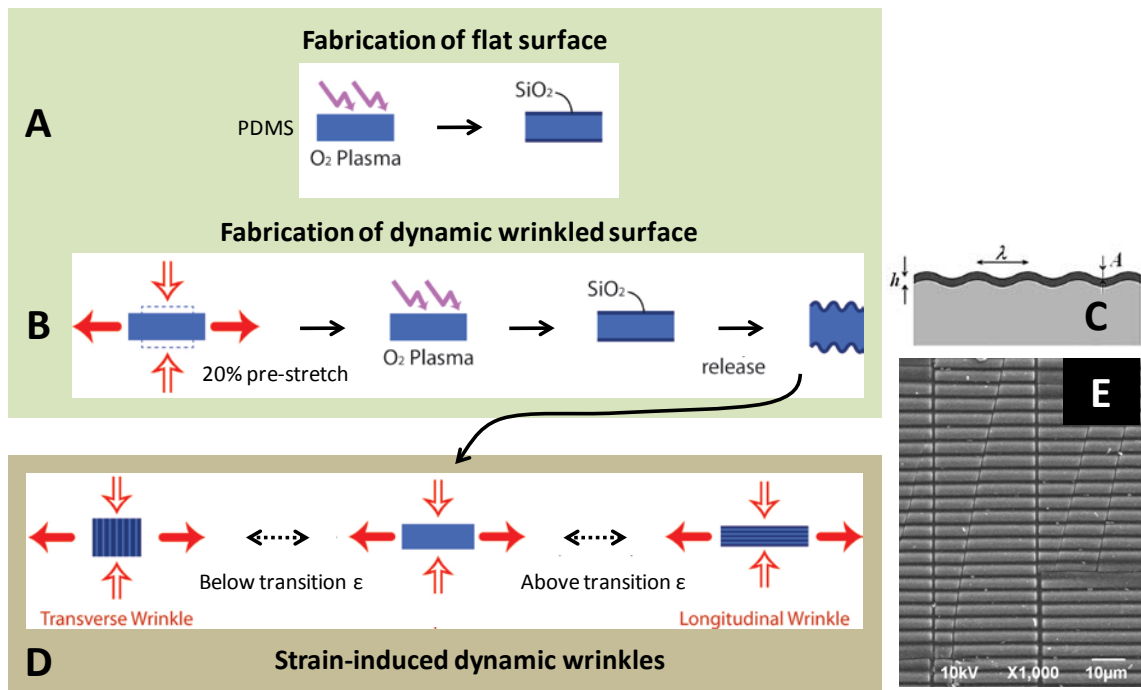


Figure 30. Fabrication and actuation of periodically wrinkled PDMS elastomer substrates. Polydimethylsiloxane (PDMS) substrates were treated with 60 seconds of oxygen plasma to create a nanoscale silica skin, thus presenting identical surface chemistry in all experiments. In contrast to flat substrates (a) that were plasma treated without applied strain, dynamic wrinkle substrates were fabricated by applying a 20% pre-stretch during oxidation. Upon relaxation, highly controlled and regular buckling of the silica skin results, as schematically shown in (c). (d) The pre-stretch amplitude determines a sharp

Figure 30 (Continued)

transition point for wrinkle orientation, whereby the wrinkles are transverse below the pre-stretch point and primarily longitudinal above it. (e) SEM image of wrinkled PDMS surface, with regular wrinkles seen in the horizontal direction and small perpendicular cracks, which are a minor fabrication artifact.

compression when the bulk PDMS is released, as shown in Figure 30b-c. For this study, it was found that 60 seconds of oxygen plasma treatment and a pre-stretch of  $\epsilon = 20\%$  would generate surface micro-wrinkles on the order of  $1\ \mu\text{m}$  wavelength and aspect ratio  $\sim 0.5$ . Moreover, the wrinkles are oriented transverse to the pre-stretch direction when the substrate is subsequently strained by  $\epsilon < 20\%$ ; but owing to Poisson contraction, the wrinkles switch to mainly longitudinal orientation for  $\epsilon > 20\%$ . (134) Hence the topography itself is highly dynamic and is mechanically actuated simply by stretching or relaxing the substrate within a narrow strain range about the switching point, as shown in Figure 30d. A minor and inevitable artifact of the fabrication process for dynamic wrinkle topography is the generation of small longitudinal cracks, as seen running perpendicular to the regular wrinkles in Figure 30e. However, these only affect a small fraction of the overall sample surface area.

Since plasma treatment of PDMS leads to vitrification of the surface layer, the surface chemistry is no longer identical to that of native PDMS, but is similar to hydrophilic glass. To ensure identical surface chemistry across all samples in the study, the flat PDMS substrates were also plasma treated but without pre-stretching (Figure 30a), such that they did not form significant, regular wrinkles.

As imaged by fluorescence microscopy in Figure 31a, the attachment of *Pseudomonas aeruginosa* PA-14 bacteria on a flat PDMS surface appears random and isotropic, whereas the bacteria spontaneously pattern on static PDMS wrinkles, closely registering with the wrinkle spacing and orientation (Figure 31b). SEM inspection also reveals preferential attachment of bacteria to the troughs of the physical surface features, as seen in Figure 3c. While directed bacterial attachment behavior has also been reported on high aspect ratio pillar arrays (86, 128), the lower aspect ratio structures on the wrinkled PDMS are mechanically more robust and feasible to fabricate on a large scale.

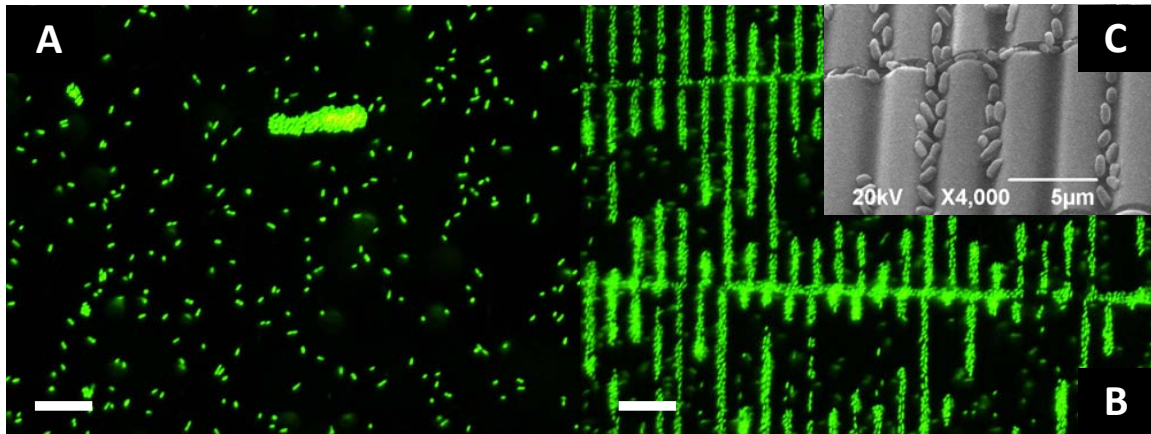


Figure 31. As imaged by fluorescence microscopy, (a) the attachment of *Pseudomonas aeruginosa* PA-14 bacteria on a flat PDMS surface appears random and isotropic, while (b) the bacteria spontaneously pattern on PDMS wrinkles, reflecting the wrinkle spacing and vertical orientation in the image. The horizontal chains of bacteria follow small perpendicular substrate cracks. (c) SEM image showing the registration of bacteria with the physical surface features. The bacteria are preferentially attached to the troughs of the surface wrinkles. This selective behavior suggests that introducing dynamic re-orientation of the wrinkles as well as tensile strain can frustrate bacterial attachment. Scale bar = 10 µm.

We have investigated how introducing dynamic re-orientation of the wrinkles, as well as cyclic tensile strain of the surface, can synergistically frustrate bacterial attachment of marine organisms' active skins.

Combining dynamic strain, dynamic topography, and other factors introduced a large parameter space. Potentially relevant parameters were identified as: surface wrinkle length scale; mechanical strain amplitude, time scale and continuous versus intermittent operation; variation of biofilm-forming bacterial species and cell geometry; and bacterial growth time. To probe these effects, a multifactorial design of experiments was conducted.

## **2. Parameter space explored**

### **A. Strain amplitude, rate, intermittent vs. continuous**

Notwithstanding the 300% elastic limit of PDMS, the practically achievable strain was limited between ~5% and ~50% due to the precision and force limitations of our instrument. Preliminary testing of biofilm attachment following 24 hr growth on flat substrates did not show significantly different attachment levels regardless of whether the substrates were cycled between 0% (relaxed) and 10%, 0% and 20%, or 0% and 50% strain, suggesting low sensitivity to this parameter. For fabricating dynamic wrinkle substrates, a 20% pre-stretch during plasma treatment was adopted. Both small (4%) and large (10%) cyclic strain amplitudes about the 20% pre-stretch point (i.e., 16-24% and 10-30%) were tested for biofilm attachment, also showing no significant difference. Thus the larger 10% strain amplitude (cycling between 10% and 30% absolute strain) was chosen as the standard for all experiments, in light of instrument precision limits and

potential for substrates to slightly creep out of the grippers over extended experiments.. That large strain magnitudes and/or amplitudes are not critical is a promising factor for the dynamic surface concept's application potential.

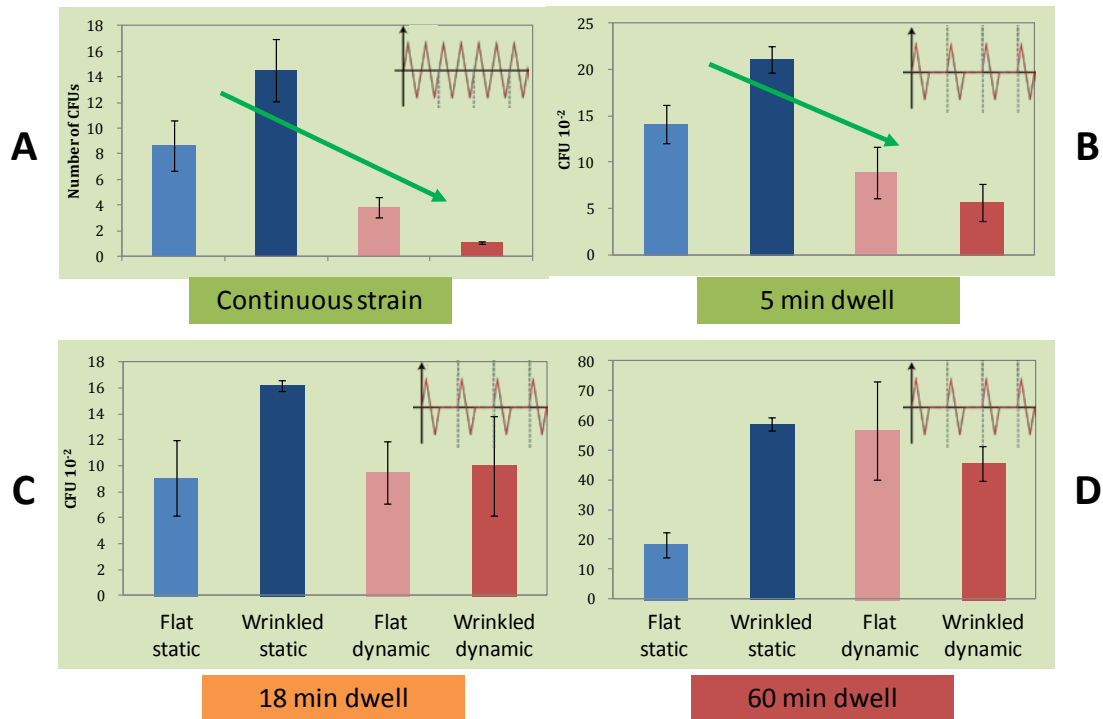


Figure 32. Bacterial biofilm attachment after 24 hr growth on elastomeric substrates with respect to topography, dynamic strain (cycling between 10% and 30%), and dwell time between strain events. Insets show schematic waveform of strain applied to dynamic substrates with respect to time. (a) In the continuous strain condition, with no dwell time, an attachment decrease of almost 80% occurred on dynamic wrinkled substrates versus the static substrates and the dynamic flat substrate. (b-d) However, the introduction of dwell time, particularly beyond 5 minutes duration between strain cycles negated the inhibitive properties of dynamic elastomer wrinkles. In these cases, biofilm attachment leveled or even increased versus a flat static substrate.

*P. aeruginosa* biofilm attachment was grown for 24 hr on flat and wrinkled static substrates, as well as flat and wrinkled dynamic substrates. As seen in Figure 32a, the application of continuous cyclic strain to the flat substrates decreased biofilm attachment by ~56%. The addition of wrinkled topography in the static condition increased biofilm relative to the flat substrate, consistent with an increase in available surface area for bacteria. However, an attachment decrease of ~78% occurred on dynamic wrinkled substrates versus the static flat substrates--indeed pointing to a synergy of the strain and the dynamic wrinkles that, like the echinoderm skin, serves to frustrate biofilm accumulation.

To minimize energy input and disruption of the antifouling surface, the effectiveness of intermittent “shocks” as opposed to continuous cyclic strain was considered. Dwell times of 5, 18, and 60 min were added between strain cycles, as shown schematically by the inset waveforms in Figure 32b-d. However, the introduction of dwell time, particularly beyond 5 minute duration, negated the inhibitive properties of dynamic elastomer wrinkles (Figure 32c-d). In these cases, biofilm attachment leveled (or, curiously, even increased) versus a flat static substrate. But it is notable that the characteristic viscoelastic relaxation time of a wide range of bacterial biofilms has been reported to be ~18 min. (135) As this is the longest time within which a biofilm may mount a phenotypic response to an imposed mechanical force, it stands to reason that dwell times must not be too intermittent in order to still mechanically affect the development of the biofilm.

## B. Topography length scale

Previous work showed that topography on the order of the bacterial length scale would maximize patterned attachment of bacteria. (86, 128) At the same time, studies have suggested that smaller length scale topography can reduce bacterial and other microorganismal attachment due to a geometric decrease in available attachment area. (136-137) To investigate this point in the context of a dynamic surface, we varied the width of the surface wrinkles by controlling the duration of plasma treatment during substrate fabrication. Wrinkle troughs were produced either submicron wide,  $\sim 1 \mu\text{m}$ , or  $\sim 2 \mu\text{m}$ . As shown in Figure 33a, *P. aeruginosa* biofilm attachment decreased  $\sim 54\%$  with the addition of submicron wrinkles, but then no further decrease resulted from introducing dynamic strain. It is conceivable that a reduced available surface area also reduces the frustration effects of mechanical strain. Exceeding bacterial dimensions,  $\sim 2 \mu\text{m}$  valley width resulted in significantly increased biofilm attachment (Figure 33c), dominating over inhibition from dynamic strain. Approximately  $\sim 1 \mu\text{m}$  valley width appeared to be optimal, yielding a decrease of nearly 80%.



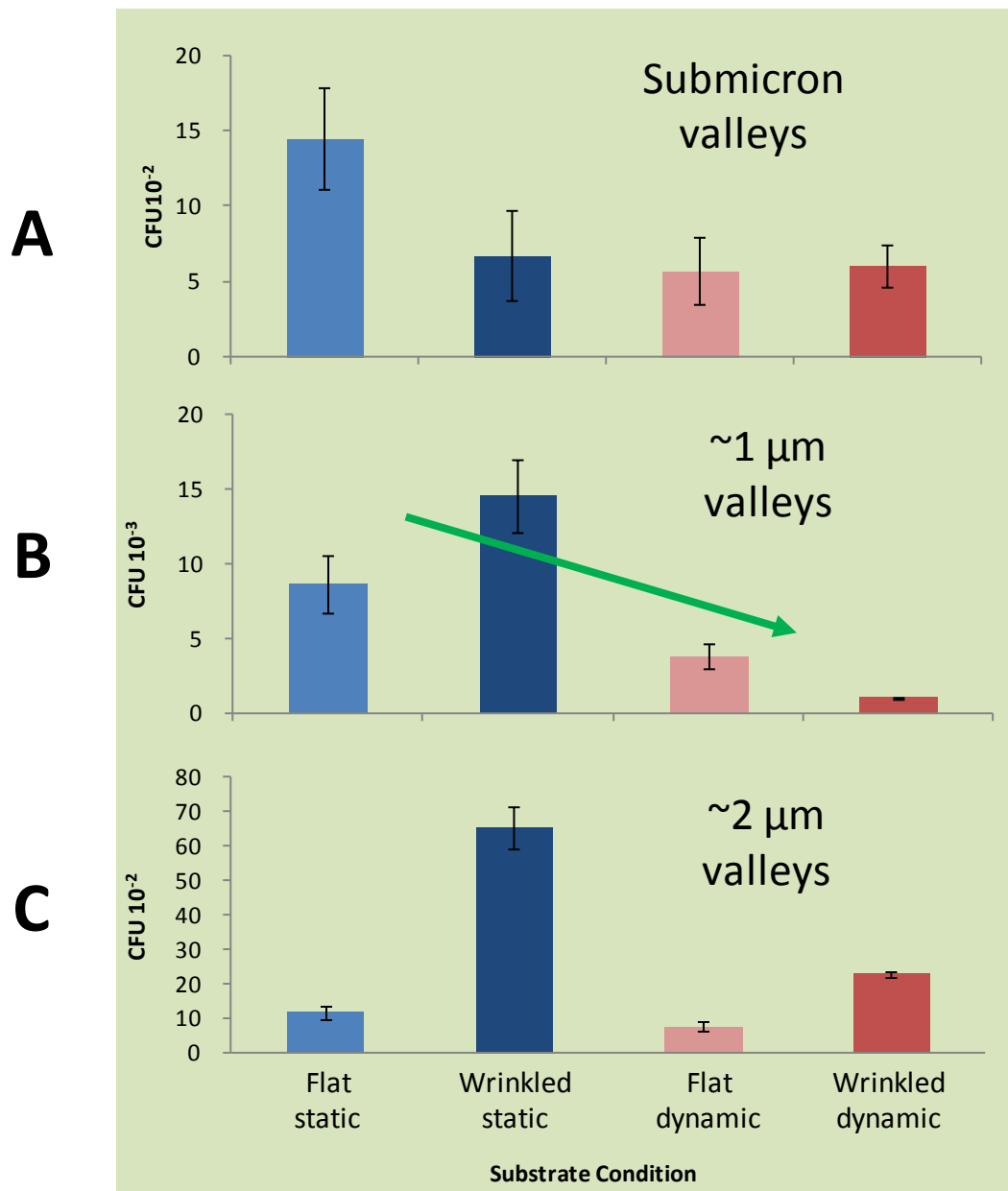


Figure 33. Effect of dynamic elastomer surface wrinkle length scale and continuously applied cyclic strain on 24 hr bacterial biofilm attachment. By varying the time of plasma treatment during the substrate fabrication, the width of the surface wrinkles was tuned, and the troughs of the wrinkles were made either submicron wide (10 seconds plasma),  $\sim 1 \mu\text{m}$  (60 seconds), or  $\sim 2 \mu\text{m}$  (300 seconds). (a) In the first case, biofilm attachment decreased 50% with the addition of submicron wrinkles, but no further decrease resulted from introducing continuous strain. (b) Approximately  $1 \mu\text{m}$  valley width was optimal for bacterial patterning and resulted in the largest attachment decrease

Figure 33 (Continued)

of 78% under continuous cyclic strain. (c) The 2  $\mu\text{m}$  valley width resulted in significantly increased biofilm attachment, dominating over the inhibitive effect of dynamic strain.

### **C. Growth time scale**

Inhibition of *Pseudomonas aeruginosa* biofilm attachment persisted to 48 hours of growth, with 62% reduction in the dynamic wrinkled condition. However, only strain appeared to support any inhibition at 72 hours, as shown in Figure 34. The topography no longer provided incremental value over flat static substrates at this extended growth point; in fact, increased growth occurred in the presence of topography in both static and dynamic conditions. Hence, the optimal design of dynamic surfaces for up to 2 days of bacterial exposure may no longer be optimal at 3 days. The factors in this transition remain an open question deserving of future study.

### **D. Bacterial species dependence**

Biofilms in nature are formed by countless different species of bacteria, and they are most commonly comprised of multiple species. In some application contexts, e.g., biomedical devices, a complete lack of biofilm may be desired, while in other cases selectively preventing the adhesion of specific types of bacteria may be advantageous, e.g., on surfaces in the oral cavity. (138-139) The species dependence of our surface's attachment inhibition was further studied with the biofilm-forming pathogens *Staphylococcus aureus* MN8 and *Escherichia coli* W3110. As seen in Figure 35a, spherical *S. aureus* bacteria showed no statistically significant attachment relationship to

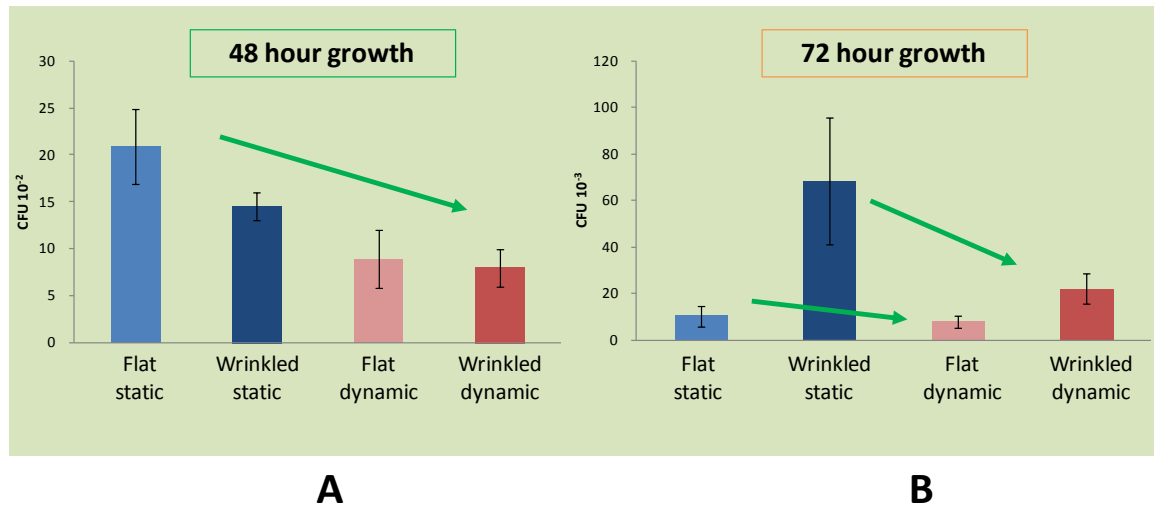


Figure 34. Attachment inhibition of *Pseudomonas aeruginosa* biofilm owing to dynamic strain persists at (a) 48 hours and (b) 72 hours of growth. While there is a 62% reduction in the dynamic wrinkled condition at 48 hours, only strain appears to support any inhibition at 72 hours. The dynamic topography no longer provides an incremental attachment decrease over flat static substrates at this extended growth point. The anti-biofilm effect of the dynamic structured surface extends to but significantly diminishes after 3 days of bacterial growth.

either dynamic strain or dynamic wrinkle topography, in sharp contrast to *P. aeruginosa* (Figure 32a). Attachment of *E. coli*, which like *P. aeruginosa* is rod-shaped, actually increased by ~250% in the presence of dynamic strain, yet showed no attachment relationship with respect to topography. It is possible that the geometry of the bacterial cell is an important factor in whether a dynamic surface affects biofilm attachment. If so, this raises the intriguing question of why *P. aeruginosa* attachment is inhibited while *E. coli* attachment is promoted under equivalent dynamic and topographic conditions. Regardless of the mechanism, our bioinspired synthetic surface platform promises an

exceptional new capability for species-specific biofilm inhibition, or inversely, selection for a desired type of bacteria--and without the use of any antibiotics or toxic chemistry.

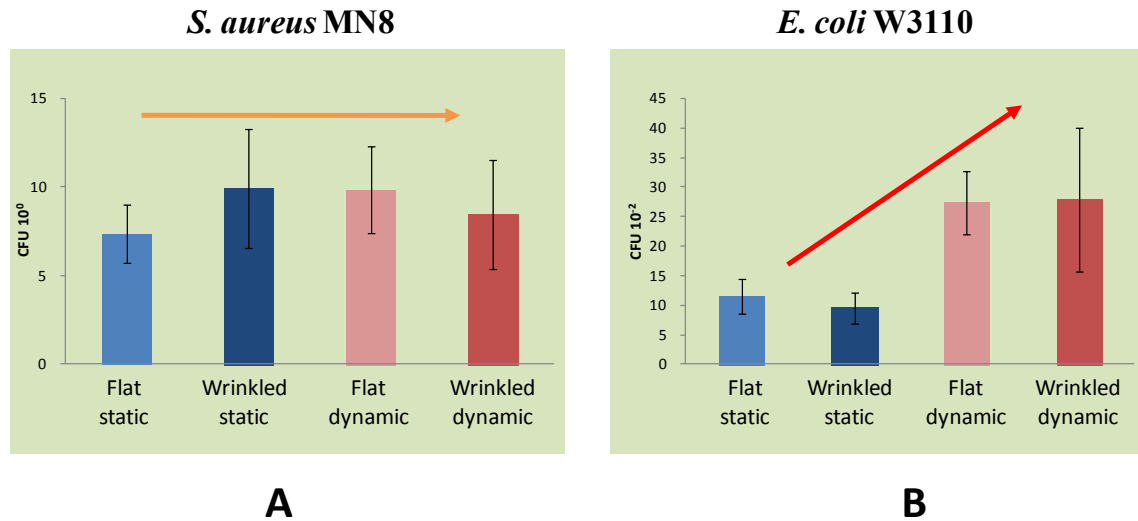


Figure 35. The species dependence of biofilm attachment following 24 hr growth under the matrix of substrate conditions was screened using (a) *Staphylococcus aureus* MN8 and (b) *Escherichia coli* W3110. (a) Spherical *S. aureus* bacteria showed no relationship to either dynamic strain or dynamic wrinkle topography of the elastomer substrate. (b) *E. coli*, which is rod-shaped, as is *P. aeruginosa*, increased attachment by 250% in the presence of dynamic strain, but showed no attachment relationship with respect to topography. It is possible that the geometry of the species is a factor in whether a dynamic surface affects biofilm attachment. Raising the intriguing question of why *P. aeruginosa* attachment is inhibited while *E. coli* attachment is promoted under equivalent dynamic conditions, the substrate represents a new means of species-specific biofilm inhibition, or inversely, selection for a desired type of bacteria.

We have demonstrated a novel approach for selectively reducing biofilm attachment--adapting the bioinspired principle of a mechanically frustrating dynamic surface—and potentially obviating the need for biofilm control by toxic release, intensive

chemical attack, or mechanical removal after the fact. The conditions for achieving up to ~80% *Pseudomonas aeruginosa* biofilm reduction on biocompatible PDMS after 24 hour growth were combinatorially elucidated. From a fabrication standpoint, the dynamically wrinkled surface is extremely simple to produce and scalable to large areas.

Highly divergent effects on the attachment of *P. aeruginosa*, *S. aureus*, and *E. coli* biofilm showed that our bioinspired dynamic substrate provides a new means of species-specific biofilm inhibition that does not rely on any toxic or transient surface chemical treatments, or inversely, enables selection for a desired type of bacteria. In future designs, this strategy could be modified to employ smaller strain amplitudes, as the dynamic wrinkle switching does not require more than a few percent strain difference. It would also be possible to capture passive sources of energy such as wind or ocean waves to drive perpetual cyclic mechanical strain of the surface. For example, an elastomeric buoy tether with dynamic surface wrinkles may continuously extend and relax, driving surface wrinkle switching and the associated attachment inhibition of selected micro-organisms.

### **Experimental method details**

*Fabrication of periodically wrinkled PDMS elastomer substrates* Substrates were cast from Dow Corning Sylgard 184 polydimethylsiloxane (PDMS), with 10:1 base- hardener ratio. The PDMS was mixed, degassed 1 hour, poured to 1 mm thickness in large dishes, and cured 3 hours at 70 °C. Uniform PDMS strips of 1 x 5 cm were cut. These were treated with 10, 60, or 300 seconds of oxygen plasma on both sides to create a nanoscale silica skin, thus presenting identical surface chemistry in all experiments. Flat substrates

were plasma treated in the relaxed state, while dynamic wrinkle substrates were fabricated by applying a 20% pre-stretch during plasma treatment. Upon relaxation, highly controlled and regular buckling (wrinkling) of the silica skin resulted. The pre-stretch amplitude determined the transition point for wrinkle orientation, whereby the wrinkles are transverse below the pre-stretch point and primarily longitudinal above.

## **V. Top down high-aspect-ratio posts**

### **1. Notional results**

In contrast to the plasma- and buckling-induced surface wrinkles of the dynamic elastomer surfaces, which display an aspect ratio of approximately 0.5, echinoderm pedicellariae, cilia, and other similar biological antifouling surface structures are typically of aspect ratio 10 or higher. As discussed in 6.A-II, high aspect ratio surface nanostructures can be designed to exhibit sufficiently low effective stiffness for bacterial attachment to be inhibited. This strategy is not exploited in the case of the low-aspect ratio wrinkle-based microtopography, although spontaneous registration of attaching bacteria with the topography occurs, similar to the HAR posts discussed in 6.A-I.

To maximize the mechanoselective adhesion effect, it may be advantageous to localize contact of bacterial cells to only the nanostructure distal ends or tips, where the effective stiffness is lowest. This can be accomplished by reducing the interstitial

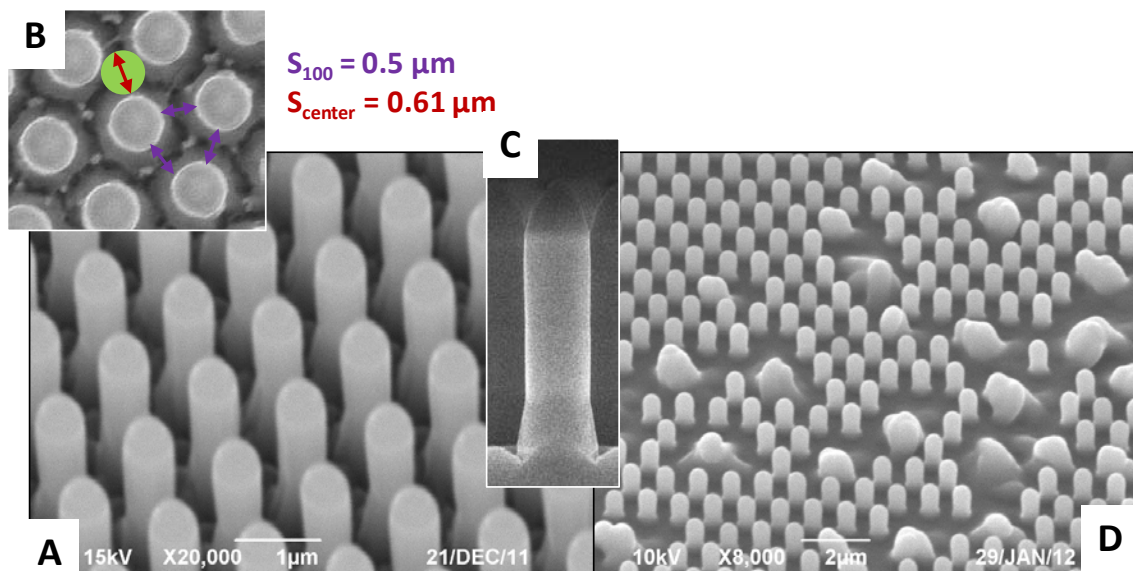


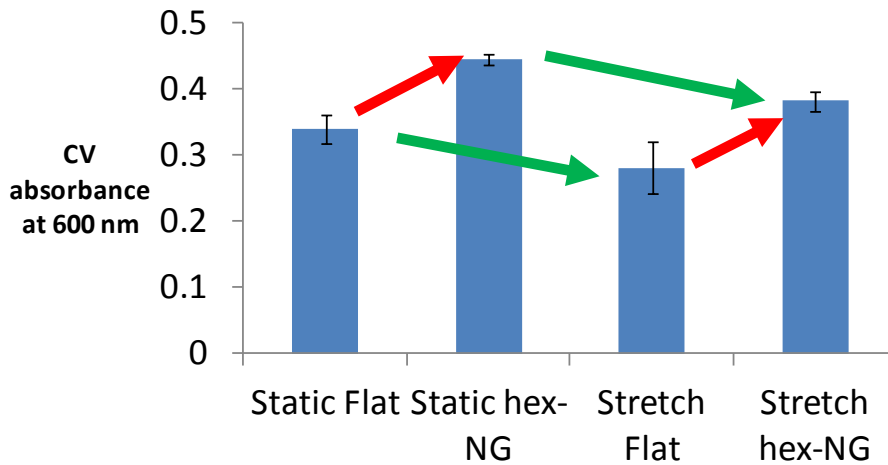
Figure 36. Geometry and replication issues of HAR high-density hexagonal post array. (a) SEM image of original silicon master with photoresist conical tips. (b) Higher magnification showing interstitial dimensions. (c) Side view of single conical-tip nanopost. (d) Replication defects that appeared in PDMS elastomeric replicas.

spacing of the nanoarray to the point that individual bacteria can no longer penetrate vertically between neighboring posts. Moreover, to further reduce the effective stiffness of the tips, a tapered tip geometry was fabricated by photolithographic methods. As shown in Figure 36A-C, a hexagonal array of conical-tipped HAR nanoposts with  $0.5 \mu\text{m}$  interstitial diameter was fabricated. The hexagonal array was double replicated via fluorosilanized PDMS negative molds into PDMS arrays. These elastomeric nanoarrays were then tested under identical dynamic strain actuation conditions as used for the wrinkled-based substrates. The effective stiffness of the hexagonal PDMS nanoarray was of the same order of magnitude as the PU nanoposts reported in 6.A-I. However, pervasive defects invariably resulted from the replication into PDMS, with collapsed,

missing, or coalesced structures as shown in Figure 36D. In addition to being at the mechanical stability limit of aspect ratio, as discussed in Section 3.G., the array's high density may have caused issues in the lift-off of the PDMS replicas.

The notional results of dynamic, low effective stiffness nanoposts tuned for maximum tip contact with bacteria did not indicate that the topographic properties inhibited biofilm attachment. Biofilm attachment decreased with the application of dynamic strain, but the addition of the hexagonal array resulted in larger magnitude attachment increases. Fabrication challenges precluded the testing of defect-free PDMS HAR nanoarrays, and it is possible that the defective regions served as sites for biofilm attachment to initiate. Future advances in fabrication will be necessary to address whether the addition of HAR nanotopography can in fact contribute to the reduction of biofilm attachment on a dynamically strained substrate.





CV absorbances

	Flat	Hex NG	Change
Static	0.34	0.445	30.88%
Stretch	0.28125	0.3825	36.00%
Change	-17.28%	-14.04%	12.50%

Figure 37. Effects of PDMS hexagonal HAR conical nanopost array and dynamic strain. Biofilm attachment decreased with the application of dynamic strain, but the addition of the hexagonal array resulted in larger attachment increases.

### C. Molecularly mobile: slippery liquid infused porous surface (SLIPS)

#### VI. Bioinspiration from the pitcher plant and the nonwetable biofilm

Clearly, it is extremely desirable to *prevent* rather than treat biofilm formation, and accordingly a wide range of bacteria-resistant surfaces have been proposed. Most strategies rely either on a release of biocidal compounds or on inhibiting adhesion. (16, 36-38) The latter approach has focused on the use of surface chemical functional groups

that inhibit protein adsorption as a means to inhibit bacterial adhesion. One of the most commonly studied such surface modifications is poly(ethylene glycol), or PEG. (39-40) More recently, structured superhydrophobic surfaces have been suggested for preventing biofilm attachment owing to the trapped air between their micro/nanoscale surface features and therefore, in principle, the reduced available solid attachment area for biofilm. (36, 140)

Both of these strategies, however, are generally transient. Materials that persistently resist bacteria are difficult to achieve by surface chemistry alone. The surface molecules are subject to desorption over time, a limitation that has driven much research in the area of strengthening the physisorption of, e.g., PEG coatings. (16) However, even if no desorption occurs and bacteria are unable to attach directly to a substrate, nonspecific adsorption of proteins and surfactants secreted by bacteria can still mask the underlying chemical functionality. (23-24, 42) Additionally, any defects or voids in the surface chemistry could serve as nucleation sites for bacterial attachment. Structured superhydrophobic surfaces in the Cassie (trapped air) state are prone to irreversible wetting (Wenzel transition), especially with the production of bacterial surfactant, seriously limiting their lifetime in submerged environments. (141) Strategies involving leaching of biocides are limited over a longer timescale since their reservoir is finite and subject to depletion. (38) Also, the emergence of antibiotic- and silver-resistant pathogenic strains, along with new restrictions on the use of biocide-releasing coatings in the marine environment, has necessitated the development of new strategies. (26-28)

Traditional anti-biofouling surfaces are in solid forms (e.g., polymers), which are either static or quasi-static in nature. Therefore, permanent interactions between the solid surfaces and the biological adhesives can be readily established, leading to bio-fouling. Creating a surface that possesses dynamic features down to nanometer scale (i.e., mobility of surface molecules or structures) may inhibit these permanent interactions, thereby significantly disrupting the bio-adhesion. A potential approach to generate dynamic surfaces is to utilize a stabilized liquid interface. Inspired by the *Nepenthes* pitcher plant (142), we recently developed a new model of omni-repellent surface, one based not on an unstable and transient solid-air Cassie-type interface but rather on a stable, immobilized, and smooth liquid surface locked in place by a specially designed porous solid. (143) This novel slippery liquid infused porous surface (SLIPS) exploits the extreme stability of the fully wetted liquid film to maintain repellency across a broad range of temperature, pressure, surface tension, and other conditions. (143) Following a set of surface energy design parameters (143), a highly immiscible liquid is simply added to a porous or textured material to create the SLIPS.

Here we report on the exceptional ability of SLIPS to prevent biofilm attachment. The SLIPS liquid in our setup is immobilized on a porous polytetrafluoroethylene (PTFE) substrate (144-147) and presented as a smooth liquid-liquid interface to bacteria. Through rigorous quantification, we demonstrate that our SLIPS platform prevents up to 96-99% of common bacterial biofilms from attaching over at least a 7-day period in a low flow environment, a 35x advance over best-case-scenario, state-of-the-art surface chemistry treatments based on PEGylation (148). This result extends across bacterial species, including the clinical pathogens *P. aeruginosa*, *S. aureus*, and *E. coli*. We

furthermore confirm that the lack of biofilm attachment is not caused by any cytotoxicity of the SLIPS liquid, but by its exceptional mobility on the slippery interface. Moreover, the SLIPS anti-biofilm surfaces are simple to manufacture, low-cost, passive, and can be incorporated on arbitrarily shaped surface contours, such as catheters, pipelines, or other systems requiring prolonged biofilm resistance.

## 1. Fabrication overview

*SLIPS fabrication.* To prepare SLIPS, lubricating fluid was added onto the porous solids to form an over-coated layer. The lubricating fluids used for the anti-biofilm experiments were perfluorinated fluids: Dupont™ Krytox® 100 and 103, 3M™ Fluorinert™ FC-70, and Perfluorodecalin (Sigma Aldrich). The porous solids used were Teflon membranes with average pore size of  $\geq 200$  nm and thickness of  $\sim 60 - 80$   $\mu\text{m}$ , which were manufactured by Sterlitech Corporation, WA, USA. These membranes were used as received without further modification. With matching surface chemistry and substrate roughness, the fluid will spread spontaneously onto the whole substrate through capillary wicking. The excess liquid not bound to the underlying solid was removed by tilting the surface and mildly applying compressed air.

*Silicon microstructure array fabrication.* Superhydrophobic microstructure arrays were fabricated on a 4" silicon wafer by the Bosch process. (149) The microstructures consist of four types of geometries:  $d = 500$  nm high-aspect-ratio (HAR) nanoposts,  $2$   $\mu\text{m}$  pitch ( $p$ );  $d = 1$   $\mu\text{m}$  HAR microposts,  $p = 3$   $\mu\text{m}$ ;  $5$   $\mu\text{m}$  T-shaped microposts; and  $10$   $\mu\text{m}$  T-shaped microposts. The wafer was rinsed with EtOH, oxygen plasma treated for 30 seconds and was rendered hydrophobic by putting the sample in a vacuum desiccator

overnight with a glass vial containing 0.2 mL heptadecafluoro-1,1,2,2-tetrahydrodecyltrichlorosilane (Gelest Inc).

*Flow cell setup.* A Tygon tube of inner diameter 3 mm was mounted in a peristaltic pump (Cole Parmer) and connected via hose barb fittings (World Precision Instruments) to a dual-chamber 3D-printed flow cell (chamber dimensions  $l = 10$  cm,  $w = 1$  cm,  $h = 1$  mm). The bottom surface and sidewalls of each chamber were lined with press-fit porous Teflon membrane; one was infused with Krytox 103 to create a SLIPS and the other was left untreated as a control. Bacterial culture was pumped into each tube until the loop was full and trapped air had been eliminated through a bubble escape, after which the pump was operated for the desired periods of time (24 h, 48 h, 7 d).

## **VII. Static condition growth**

### **1. Attachment comparison to Teflon and superhydrophobic silicon nanoarrays**

In a simple test scheme, *Pseudomonas aeruginosa* TB culture was deposited in puddles that were statically grown upon three surface typologies, two of which are shown in Figure 38. A porous PTFE membrane (0.2  $\mu\text{m}$  pore size) served as a flat, conventional low-adhesive control surface; a fluorosilanized patterned silicon wafer (Figure 39)

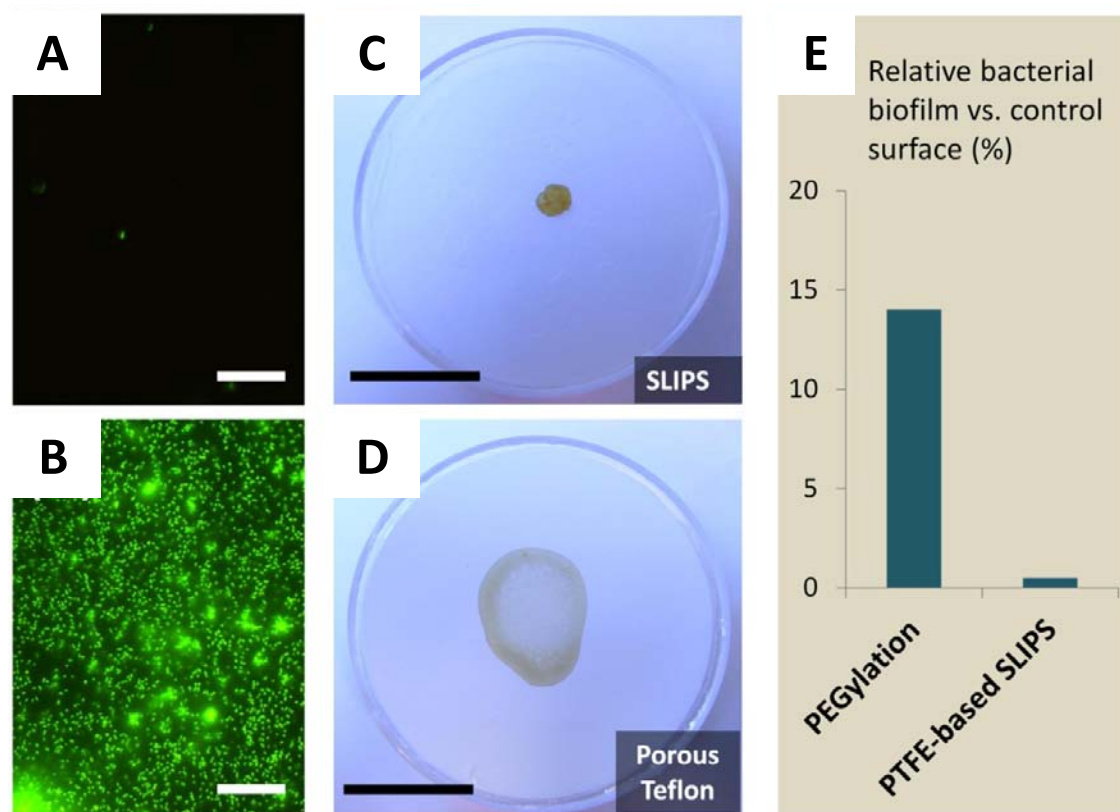


Figure 38. Biofilm attachment properties of surface typologies investigated in this study. (a-b) Fluorescence micrographs of attached bacteria following 48 hour incubation of *P. aeruginosa* biofilm on each surface. Robust and uniform attachment resulted on the superhydrophobic PTFE (and microstructured silicon seen in Figure 39 but virtually none resulted on the slippery liquid infused porous surface (SLIPS), which presents a highly immiscible, nonvolatile, and immobilized liquid surface. Scale bar = 30  $\mu\text{m}$ . (c-d) Remains of an evaporated drop of *Pseudomonas aeruginosa* biofilm-forming culture on each surface. Note that the poorly attached biofilm on the SLIPS substrate (c) cleanly retracts from the surface as it evaporates (see Figure 41), leaving behind a small pellet that is easily removed by tape, as shown in Figure 42. In contrast, biofilm grown on the PTFE (d) and microstructured superhydrophobic silicon (Movie S1) shows complete wetting of the surface and leaves behind a slimy coffee ring. Scale bar = 2 cm. (e) Comparison of biofilm attachment to our SLIPS substrate and to a state-of-the-art PEGylated substrate, assuming in a best-case scenario that its 5 hour PEG performance

Figure 38 (Continued)

(148) can be maintained at 7 days without degradation of surface chemistry due to desorption or masking. The 0.4% relative attachment, based on crystal violet quantification, is a >30x improvement over PEG-functionalized surfaces.

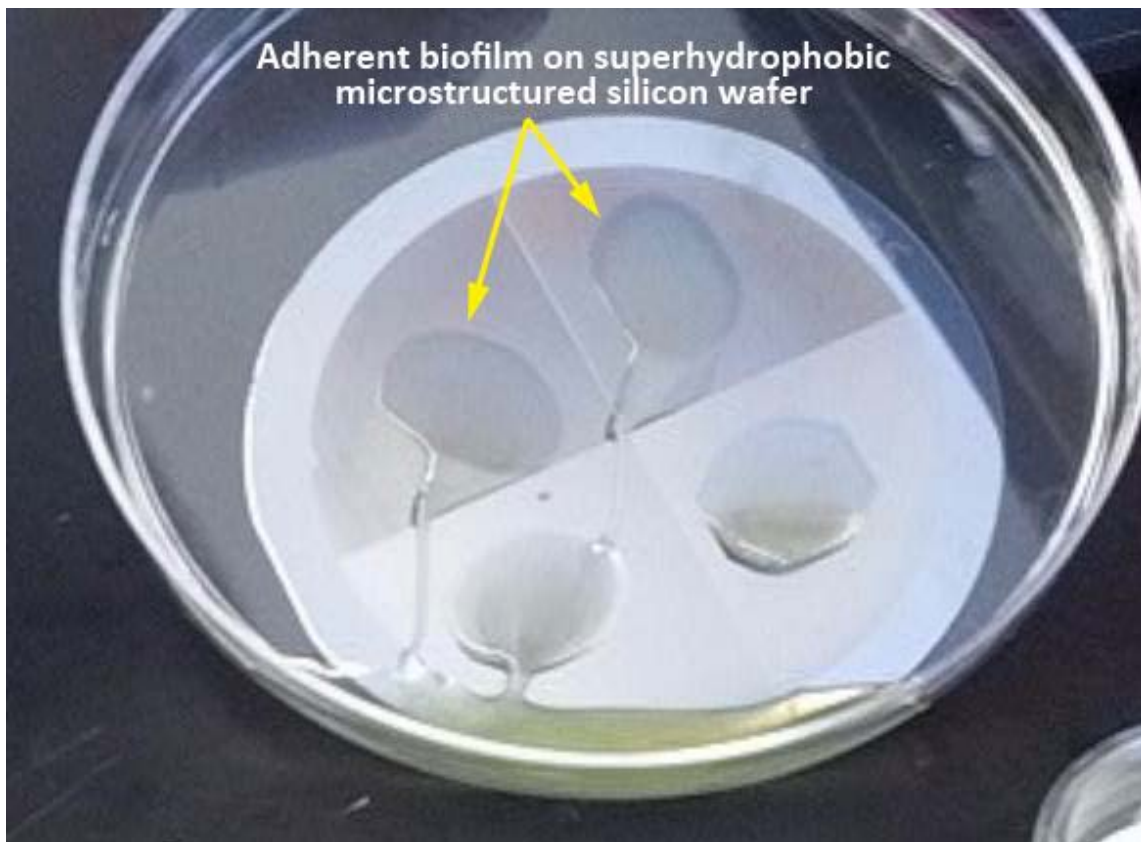


Figure 39. 48-hour *P. aeruginosa* biofilm puddles grown at room temperature on a superhydrophobic nanopost array silicon wafer, subsequently tilted to observe biofilm adhesion. The puddles consist of TB with 1% initial seeding concentration of *P. aeruginosa* LB culture. Biofilm shows complete wetting of the surface and leaves a film of slime as it is tilted.

featuring four different high-aspect-ratio micropost arrays presented a superhydrophobic surface, able to repel and roll off water; and a PTFE membrane infused with Krytox-103

provided a SLIPS liquid slippery surface. After 48 hours of room temperature growth in static culture, the viable cell concentration of the imposed bacterial films on both surfaces was on the order of  $10^8$  mL<sup>-1</sup>. The bacteria were fixed and stained, and the fluorescence micrographs of resulting growth are shown in Figure 38a. While robust and uniform biofilm coverage is observed on both flat PTFE and superhydrophobic silicon, only sparse and isolated cells are seen on the SLIPS. The test surfaces were also manually tilted to compare the adhesion of the macroscopic biofilm slime as shown in Figure 40. Biofilm grown on the control and superhydrophobic substrates shows complete wetting of the surface and either leaves a film of slime or remains pinned as it is tilted. In contrast, biofilm on the SLIPS substrate (Figure 40) slides readily without leaving any visible residue behind.

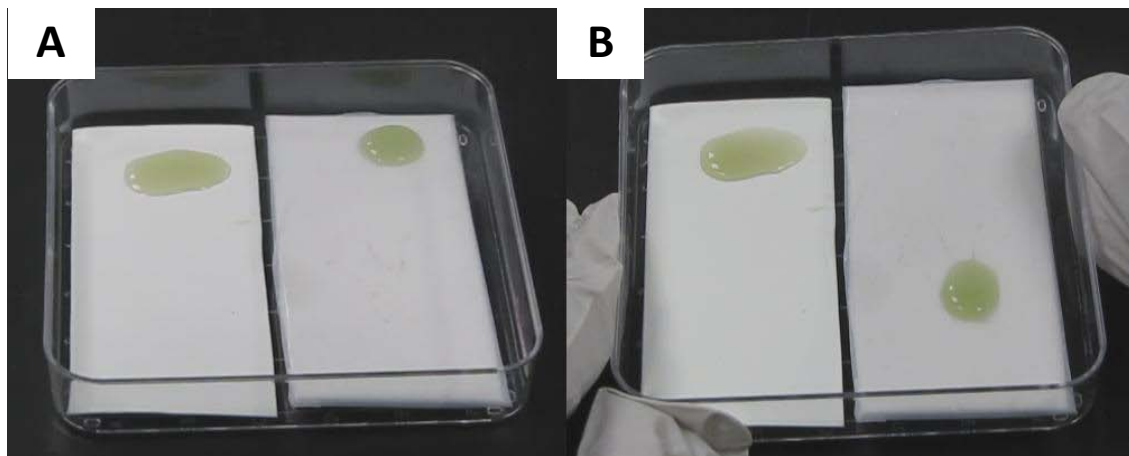


Figure 40. *P. aeruginosa* biofilm puddles grown 24 h on a PTFE porous surface and a PTFE SLIPS surface infused with Krytox 103, before (a) and after (b) being tilted to test biofilm adhesion. Biofilm grown on the control PTFE substrate shows complete wetting of the surface and remains pinned in place. In contrast, biofilm on the SLIPS substrate slides readily without leaving any slime film or other visible residue behind.



## 2. Biofilm slime evaporation, adhesion, and removal

We further characterized the contact line pinning characteristics of the surfaces (i.e., SLIPS and porous Teflon) by monitoring the evaporation dynamics of the bacterial culture droplets, as well as the stains remaining on the surfaces upon drying (Figure 38c-d). In the absence of pinning, the droplet should follow a nearly constant contact angle mode of evaporation (150), without the formation of a coffee ring stain (151). Indeed, this mode was consistent with our observations of the contact line movement for the bacterial droplet evaporation from the SLIPS surface. The absence of the coffee ring formation also indicates that the adhesion of the bacteria on the SLIPS is small as compared to the forces imparted by the meniscus of the droplet (152-153), and we

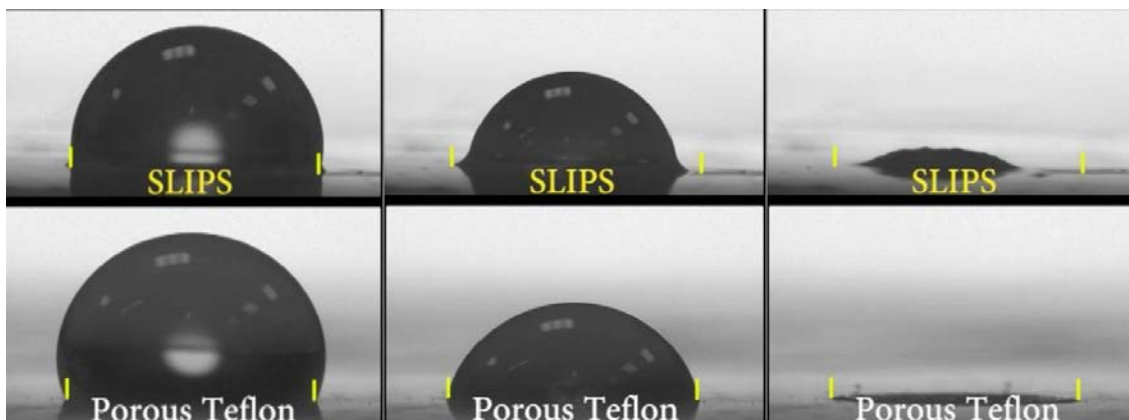


Figure 41. Split-frame still images and movie showing evaporation dynamics of *P. aeruginosa* culture droplets on a superhydrophobic PTFE porous surface and a PTFE SLIPS surface infused with Krytox 103. The pinning characteristics as well as the stains remaining on the surfaces upon drying indicate the level of adhesion between the bacterial droplet and the substrate. In the absence of contact line pinning, the droplet should follow a nearly constant contact angle mode of evaporation (150), without the formation of a coffee ring stain. (151) The absence of the coffee ring formation also indicates that the adhesion of the bacteria on the SLIPS is small compared to the forces imparted by the meniscus of the droplet.

demonstrate in Figure 42 that the dried biofilm is extremely easily removed from SLIPS by adhesive tape. In contrast, an evaporating droplet on the porous Teflon was strongly pinned, leading to a constant contact area mode of evaporation (150) and to the formation of an irremovable coffee ring. (151) These visual demonstrations of biofilm non-attachment to SLIPS and of resisting  $3.5 \times 10^8 \text{ mL}^{-1}$  bacterial liquid are consistent with both macroscopic and microscopic quantification in the present study.

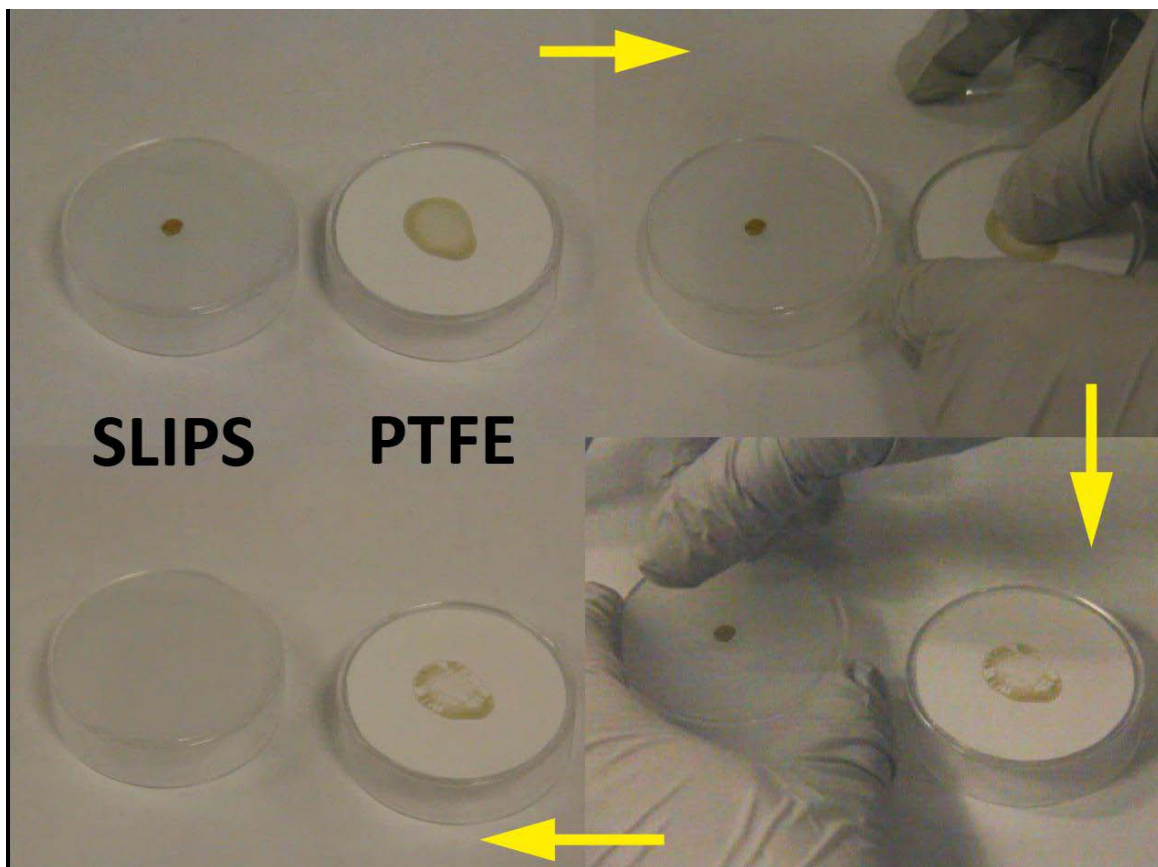


Figure 42 .Due to the low adhesion of the biofilm-forming bacterial droplet on the SLIPS, the dried bacteria following evaporation of the droplet can be removed from SLIPS simply by adhesive tape. In contrast, an evaporating droplet on the porous Teflon is strongly pinned, leading to the formation of an irremovable coffee ring.

## **VIII. Flow condition growth**

### **1. Context of physiological and engineered system flows**

While the above static experiments clearly show poor biofilm attachment to SLIPS compared to other surfaces, it is important to emphasize that many, if not most, environments, in which biofilm prevention is imperative, are not static. In particular, most submerged biofilm formation occurs under various flow conditions, e.g., in plumbing, ship hulls, catheters, or implant surfaces, and biofilms are known to attach robustly to substrates under flow. (21, 154) The design of surfaces on which biofilm attachment is sufficiently weak such that the cells can be removed even by gentle flow would provide a persistent antifouling strategy superior to bactericidal or chemical approaches.

It should be noted that the flow velocity of  $\sim 1$  cm/s that we chose for this study was intended as a conservatively gentle condition. In other environments where biofilms form, e.g., a residential building water pipe or a ship hull at 20 knot cruise speed, typical flow velocities can be on the order of 1 m/s and 10 m/s respectively, with proportionately higher shear forces that would accelerate biofilm removal from a SLIPS substrate. In biological and biomedical systems such as indwelling catheters, urinary tracts, and the human vascular system, flow velocities are also frequently more aggressive, on the order of 10-100 cm/s. (155-156)

## 2. Stability of SLIPS function under prolonged flow

Biofilm attachment was studied on test surfaces lining a dual 3D-printed flow cell, through which the bacterial culture was continuously circulated by a peristaltic pump. Under flow conditions of 10 mL/min volume flow rate and  $\sim 1$  cm/s linear velocity, both a control PTFE and SLIPS surface were exposed in parallel to PA14

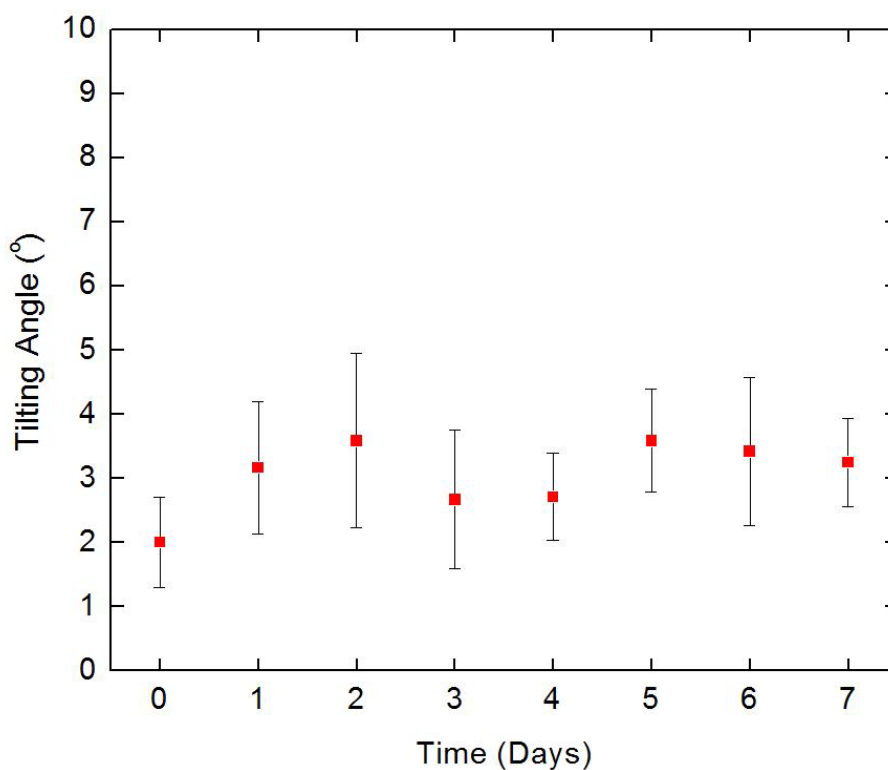


Figure 43. SLIPS stability in the flow. The tilt angle of water droplets on the surface of the SLIPS was measured over the course of 7 d under water flow of 10mL/min (1 cm/s) through the dual chamber. The chamber was opened every 24 h, 30  $\mu$ L water droplets were applied to the SLIPS at  $0^\circ$ , and the angle was slowly adjusted until the droplet began to slide to measure the sliding angle of the SLIPS over time. The statistically unchanged sliding angle over the time period confirms that SLIPS functionality does not degrade under prolonged flow. Error bars = standard deviation; n = 6.

bacterial culture for 24 h, 48 h, and 7 d (168 h) periods. We further verified that the functionality of SLIPS does not degrade over the experimental time frame (Figure 43). Indeed, the PTFE and SLIPS substrates following 48 h growth show a yellowish, slimy control substrate and a visually uncontaminated SLIPS (Figure 44a-b). To visually inspect and quantitatively compare the biomass attached in flow by optical density,

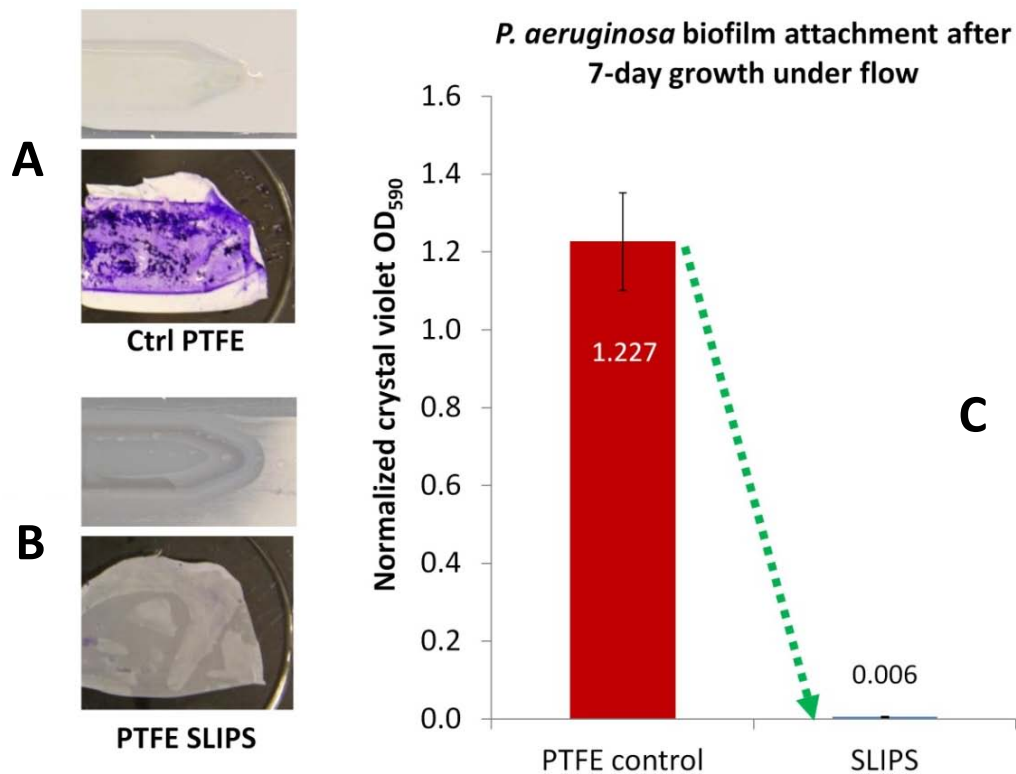


Figure 44. Macroscale view of biofilm attachment inhibition on SLIPS. Growth was conducted in a peristaltic pump at 10 mL/min (velocity  $\sim$ 1 cm/s) and dual-chamber 3D-printed flow cells with  $h = 1$  mm,  $l = 10$  cm,  $w = 1$  cm channels. (a-b) Photographs of the control PTFE and SLIPS PTFE substrates after the flow cell was opened following 48 hour growth under 10 mL/min flow, both before crystal violet staining (top) and after (bottom). Equal-area samples of the substrates were prepared for crystal violet quantification, a measurement of attached biomass. (c) Following 7 days of growth, crystal violet staining-based quantification showed a 99.6% reduction in attached biofilm on SLIPS versus control PTFE.

attached biofilm was stained by crystal violet. (157) This macroscopic assay showed a dramatic difference between the substrates, seen in Figure 44a-b. Crystal violet absorbance, proportional to the attached biomass, showed a 99.6% average reduction in biofilm on SLIPS as compared to control PTFE following 7-day bacterial growth in the flow (Figure 44c). By comparison, PEGylated titanium surfaces have been reported to reduce biofilm attachment by 86% after 5 h of growth. (148) We measured the 48 h growth of *P. aeruginosa* on Ti-coated glass slides (prepared as described in (148)) to differ by < 19% from PTFE, indicating similar long-term biofilm attachment on these two controls and thus a similar starting point for attachment reduction. Even if no PEG desorption or chemical masking were to occur following 7 days in bacterial culture, the 14% relative biofilm attachment (148) would still be ~35 times more than we measured on the SLIPS substrate after one week of growth.

To characterize biofilm attachment to PTFE and SLIPS substrates on the microscale, we fluorescently imaged multiple sample areas following 24 h, 48 h, and 7-day flow condition growths. The results were analogous to the initial static growth experiment. Biofilm on the control surface appeared characteristically dense, three-dimensional, and uniform (Figure 45ab). On the SLIPS, only sparse, isolated single cells or microcolonies were observed (Figure 45cd), and these appeared to be unattached, i.e., drifting with convective currents in the ambient fluid. This observation further supports that SLIPS provides very low adhesion to the individual bacteria or micro-colonies. The average fluorescence intensities of 20 representative fields of view per substrate were computed as numeric pixel averages  $[(R+G+B)/3]$ . While not fully capturing intensity from out-of-focus biofilm structure on the control surface, the control values may be

considered a lower limit; thus there is at least a 98% average intensity reduction in the fluorescence signal from PTFE to SLIPS, similar to the global quantification by crystal violet absorbance.

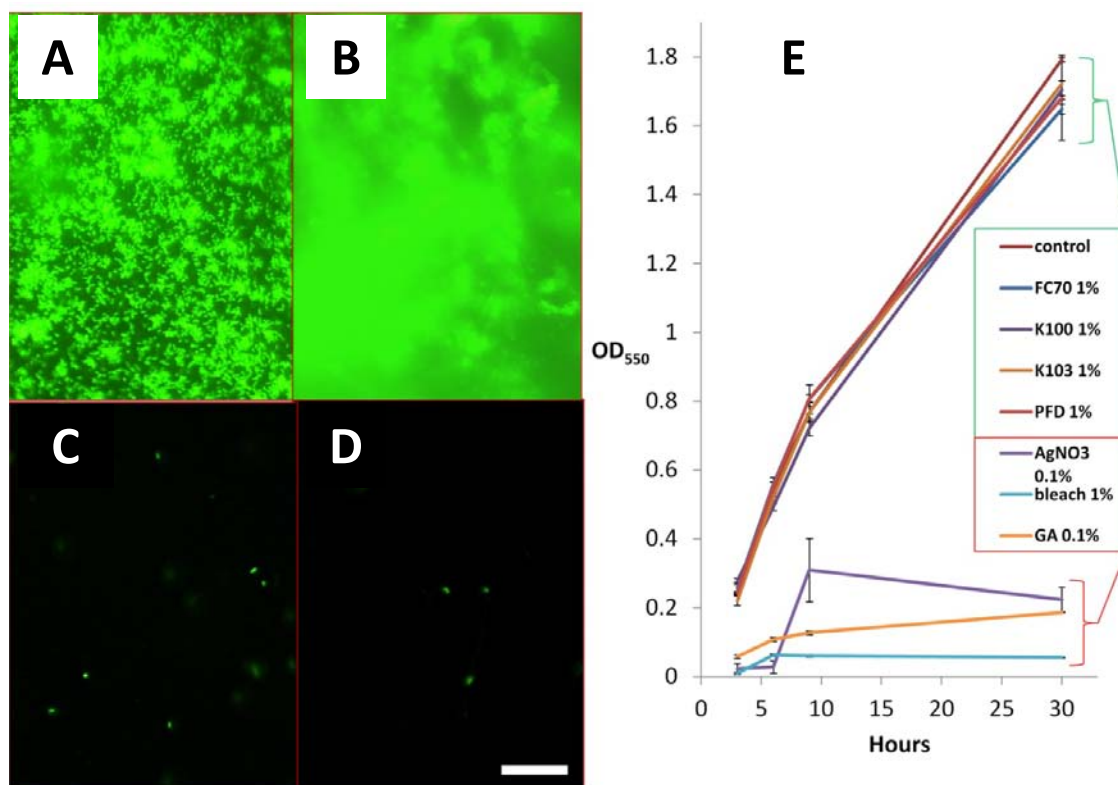


Figure 45. Microscale view of *P. aeruginosa* biofilm attachment on SLIPS and control PTFE surfaces after 24 hour and 7-day growths in 10 mL/min flow. Growth on the PTFE surface (a-b) appeared dense, three-dimensional, and uniform, whereas on the SLIPS (c-d), only sparse, isolated single cells or microcolonies were observed. These appeared to be unattached or poorly attached, i.e., drifting with convective currents in the fluid, further supporting that a liquid surface provides very low adhesion to the individual bacteria or micro-colonies. Scale bar = 30 μm. (e) To confirm that biofilm attachment inhibition is not due to toxicity of the SLIPS liquids FC70, Krytox 100, Krytox 103, and perfluorodecalin, growth curves of *P. aeruginosa* were obtained with 1% and 0.1% (data not shown) concentrations of each liquid in shaken TB cultures at 3, 6, 9, and 30 h. All growth curves progressed indistinguishably, even to 30 h [n=3]. As negative controls,

Figure 45 (Continued)

silver nitrate (a common antiseptic compound and representative of silver impregnated surfaces), bleach, and glutaraldehyde, commonly used for clinical tool sterilization, were also tested for effects on growth. They exhibited massive toxicity within these timeframes, in contrast to the null effect of SLIPS liquids, which may provisionally be considered biocompatible.

### 3. Cytotoxicity screening via growth curves

To confirm that the dramatic biofilm attachment inhibition on SLIPS substrates is not a result of cytotoxicity of the SLIPS liquids, we screened four of the liquids for effects on bacterial growth. These included the Krytox 103 used for SLIPS fabrication in this study, as well as FC70, Krytox 100, and perfluorodecalin. (158) The growth curves of *P. aeruginosa* were measured following growth in shaken TB cultures—thereby assuring uniform exposure—with 1% concentrations of each SLIPS liquid. As seen in Figure 45e, optical densities show statistically indistinguishable bacterial growth at 3, 6, 9, and 30 h for all tested SLIPS liquids as compared to the control culture. Equivalent or lower concentrations of three negative controls--silver nitrate (a common antiseptic compound and representative of silver impregnated surfaces), bleach, and glutaraldehyde (commonly used for clinical tool sterilization)--were also investigated. As expected, all three exhibited massive toxicity within these timeframes, in contrast to the null effect of the SLIPS liquids.



#### 4. Multiple species and extended growth time scales

The exceptional ability of SLIPS to resist the attachment of *P. aeruginosa* by providing a non-adhesive, slippery interface, independent of any specific chemical or physical features of the cells, raised the exciting question of SLIPS's potential as a general antifouling material resisting a broad spectrum of biofilms. Of particular importance is the potential to resist pathogenic biofilms encountered in biomedical settings and accumulated on devices such as catheters and implants under flow. To test the species generality of the SLIPS platform, we studied attachment of two other clinically important, biofilm-forming pathogens, *Staphylococcus aureus* (SC01) and *Escherichia coli* (ZK2686), for 48 h under identical flow conditions. As shown in Figure 46a-b, *S. aureus* attachment was reduced by 97.2% and *E. coli* by 96% versus PTFE, based on crystal violet absorbance. While these species form variably robust biofilms on PTFE, their final attachment to SLIPS was comparably minimal. Visualized by fluorescence in Figure 46c-f, dense uniform coverage and sparse, isolated cells respectively attached to the control surface and SLIPS. This indicates that SLIPS's anti-fouling function is nonspecific and spans phylogenetically diverse pathogenic bacteria.

From our experimental observations, it is apparent that the bacteria are presented with a smooth liquid "surface," and as such, there may be no ability to anchor to the mobile interface via pili and other cellular mechanisms as would be possible on a solid surface. (159-160) The SLIPS liquid is also immiscible with aqueous bacterial medium, and the surface tension at the interface (on the order of 50 mN/m)(29) may be difficult for bacteria to penetrate, even with bacterial surfactant production. Indeed, we did not observe bacteria embedding within the SLIPS, indicating that bacteria cannot swim

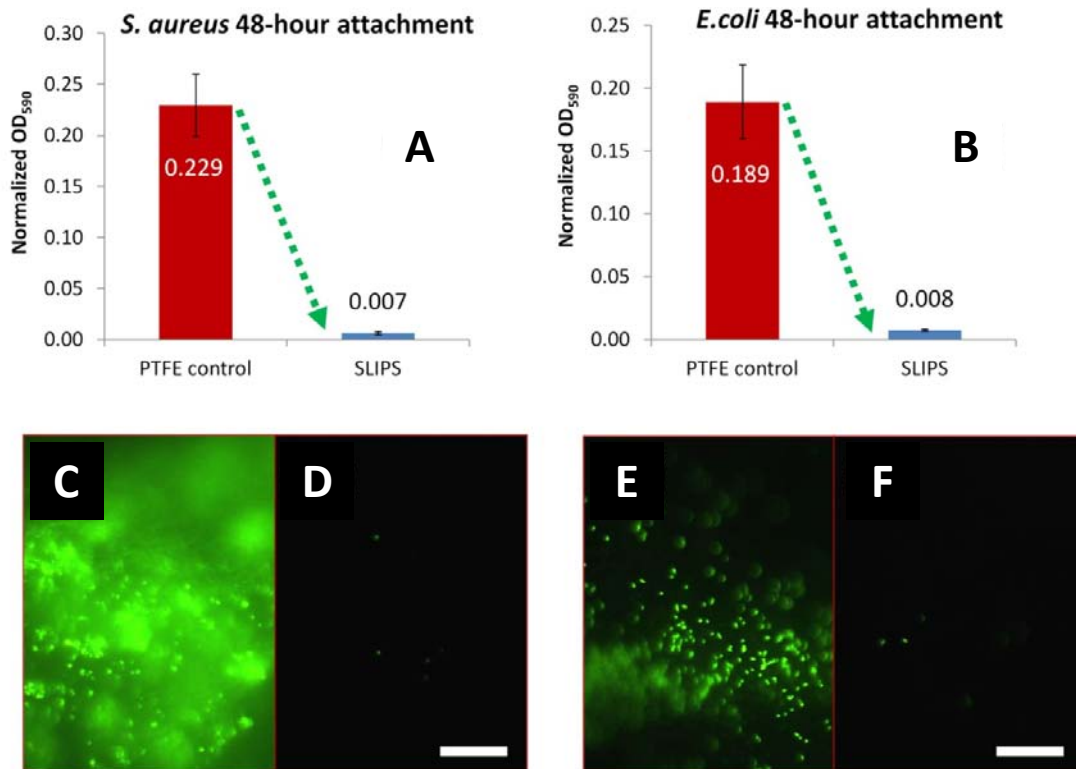


Figure 46. Biofilm attachment reduction by SLIPS is species independent. (a-b) The attachment of two other clinically important and highly pathogenic biofilm-forming species, *Staphylococcus aureus* and *Escherichia coli*, was reduced by 97.2% and 96%, respectively, versus PTFE following 48 h growth under identical flow conditions to *P. aeruginosa*, showing that the anti-fouling function of SLIPS is nonspecific and spans phylogenetically diverse pathogenic bacteria. While neither of these species formed as robust biofilms as does *P. aeruginosa*, their final attachment to SLIPS was comparably minimal. (c-f) Visualized by fluorescence, dense uniform biofilm coverage and sparse, isolated cells respectively attached to control and SLIPS substrates. Scale bar = 30  $\mu\text{m}$ .

through the interface and consistent with emulsion-based bacterial confinement studies.

(161) Without access to the solid material beneath the liquid, bacteria may be unable to attach, remaining subject to ambient flow and thus subject to passive removal. Whether

any cohesive biofilm does transiently form on SLIPS before being sheared off by even mild flow, or whether the bacteria simply remain planktonic in the medium, is still an open question deserving of future study.

In any case, at present there are no known nontoxic anti-biofilm synthetic surfaces that are capable of preventing biofilm accumulation over a period of 1 week or longer under low flow conditions. Our result of up to 96-99.6% attachment reduction over a 7-day range is a step change beyond state-of-the-art technology and is promising for a wide range of applications.

### **Experimental method details**

*SLIPS degradation measurements.* To determine if the slipperiness of SLIPS is maintained during extended biofilm growths, the SLIPS-lined flow cell was subjected to continuous 10 mL/min water flow (set up as above) over 7 d, stopping the pump and opening the flow cell each 24 h for testing. Slipperiness was quantified by recording the sliding angle of a 30  $\mu$ L water droplet applied to the surface, using a Fowler Premium V-block variable-angle stage. The water droplets were applied at 0° (horizontal) and the angle was slowly adjusted in 0.5° increments until droplet movement was observed.

*Cytotoxicity screening.* Shaken cultures of 1% *P. aeruginosa* in TB were grown in triplicate in the presence of 1% by volume of the following reagents: Krytox 100, Krytox 103, Perfluorodecalin, FC70, bleach, as well as with 0.1% of AgNO<sub>3</sub>, and 0.1% glutaraldehyde. Background samples containing only media and reagents were also prepared, as well as control cultures without added reagents. Samples were incubated in

an orbital shaker at 37 °C at 200 rpm. Optical density measurements at 550 nm were taken at 3, 6, 9, and 30 h on a Perkin Elmer Lambda 40 UV-Vis spectrometer. Optical densities were normalized by subtracting backgrounds, i.e., the reagents in TB only.

## IX. Prospects for technological development

We have demonstrated a novel approach for preventing surface biofilm attachment—simply presenting a porous surface with immobilized liquid to bacteria—and obviating the need for biofilm control by toxic release, intensive chemical attack, or even mechanical removal after the fact. We have presented proof of concept, including a 1-2 order of magnitude advance in 7-day attachment prevention versus best-case-scenario PEG-functionalized surfaces, for one of the most common and opportunistic pathogens in both terrestrial and aquatic environments, *Pseudomonas aeruginosa*, as well as for *Staphylococcus aureus* and *Escherichia coli*. From a fabrication standpoint, the SLIPS lubricant can be chosen from a wide range of biocompatible liquids, while the immobilizing texture of the solid substrate can be derived by simply casting or etching porous texture directly on device surfaces that must remain biofilm-free. Insensitive to the structural details of the underlying porous solid (143), integrated SLIPS-based surfaces that are both nontoxic and biofilm-resistant hold exciting promise for a range of cost- and potentially life-saving applications in the biomedical and industrial spaces.

## 7. Conclusions

### **A. All structured surfaces compared for effectiveness against biofilm attachment**

In this work, we have reported that bacterial biofilms, when characterized as a physical material, can present daunting treatment challenges: impenetrability to vapors and liquids alike, repelling even low surface tension commercial antimicrobials, and far exceeding the capabilities of the iconic lotus leaf. The multiple contributing factors for this defense mechanism include both biochemical components and multiscale reentrant topography. The identity of the exact molecule(s) involved has remained elusive and deserves future attention.

Faced with a natural problem, we have at the same time gained inspiration from the principles of natural solutions for biofouling, ranging from echinoderms to pitcher plants. Indeed, we have developed versatile surface nanofabrication platforms capable of programming functional surfaces with arbitrary geometric structures, tunable mechanical properties, dynamic deformation, and even a liquid slippery interface. Altogether, these platforms enable a truly novel approach to the microbiological challenge of biofilm attachment and contamination. Our portfolio of passive, active, and liquid dynamic structured surfaces has shown that physical surface properties alone can be used to direct the collective attachment behavior of bacteria. Uniquely inherent to this strategy is the combined lack of chemical toxicity and avoidance of masking.

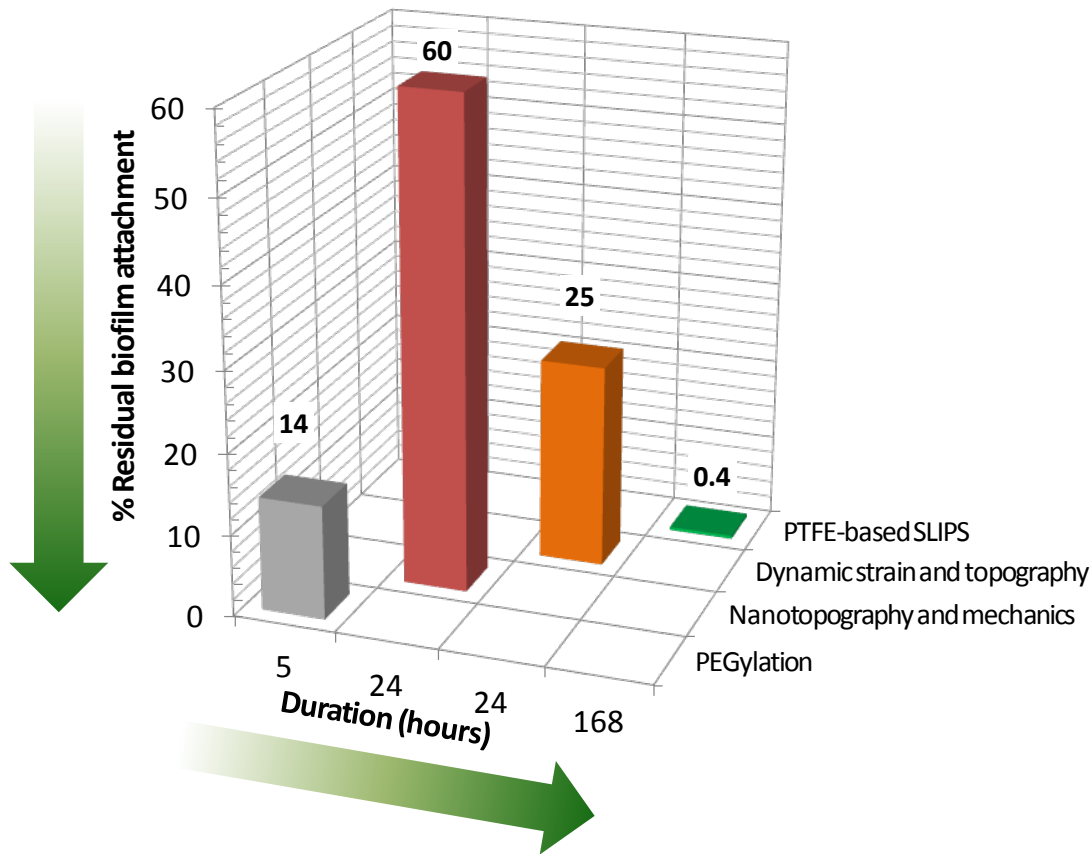


Figure 47. Efficacy and duration comparison of bioinspired biofilm prevention methods compared to state of the art surface chemistry. Desirable performance trends are in the green arrow directions. State of the art multivalent PEGylation of a titanium surface is reported to provide 86% reduction of *Pseudomonas aeruginosa* biofilm up to 5 hours. (148) Compared to this baseline, passive polymeric HAR nanorarrays mechanoselectively inhibit up to ~40% of biofilm attachment following 24 hours of growth—a reduction in resistance yet a nearly 5x advance in duration. Twice more effective at 24 hours (and to a lesser extent at 48 and 72 hours) is the application of cyclic surface strain and dynamic micro-topography. Our atomically-mobile SLIPS-based platform realizes the most significant performance increase in both metrics. Up to 99.6% of a range of pathogenic bacterial biofilms are prevented from attaching for at least a one-week duration. This represents a 35x improvement over PEG-based surface functionalization, in addition to being nontoxic, highly stable, low cost, and simple to fabricate.

The functional performance of each bioinspired biofilm prevention method and of state of the art PEG-based surface chemistry is compared in Figure 47. Minimal biofilm attachment and maximal duration of surface function are the desired property trends. Compared to the 5-hour baseline functionality of surface PEGylation, passive polymeric HAR nanorarrays mechanoselectively inhibit biofilm attachment following 24 hours of growth, nearly 5 times longer, although the reduction is less pronounced. Of the same order of magnitude as PEGylation yet effective to 24 hours (and to a lesser extent to 48 and 72 hours) is cyclic surface strain and dynamic micro-topography. If future fabrication advances allow effectively-compliant high-aspect-ratio topography to be incorporated, the performance could conceivably be improved further. However, the SLIPS-based platform realizes the most significant performance increase in both metrics and offers the greatest technological promise yet. In addition to being potentially biocompatible, highly stable, low cost, and simple to fabricate, SLIPS prevents ~97-99.6% of multiple pathogenic bacterial biofilms over an entire week of growth. This step change beyond conventional anti-biofilm strategies promises a tremendous range of industrial, clinical, and consumer applications.

## **B. Future bioinspired antifouling surface opportunities**

Many opportunities for developing the new surface platforms studied in this work into technological solutions can be identified. It is important to consider the potential impact of candidate applications. Here we highlight five promising areas.



Figure 48. Five potentially high-impact opportunities for developing future anti-biofilm technology based on our proofs of principle. (A) Indwelling medical devices, (B) ship hulls and other marine surfaces, (C) HVAC systems, (D) fuel tanks in aircraft and other vehicles, and (E) water distribution.

As previously described the biomedical and clinical spaces—implants, catheters, and intravenous lines as shown in Figure 48A—are key opportunities. The susceptibility of these devices to biofilm contamination is routinely a life-and-death matter. Prolonged resistance to bacterial contamination may be possible with future development of dynamic structured surfaces, exploiting their duration and potential lack of toxicity. Of course, development for medical applications will require far more rigorous and longer term clinical studies than the screening performed in the present work prior to any patient use. In contrast, the opportunity of ship hulls, which have relied for decades on toxic organometallic antifouling paints (Figure 48B) to mitigate fouling, drag, and fuel burn,

may be a low-barrier-to-entry market for our bioinspired approach. Large economic gains and emissions reductions would result from preventing up to 40% extra fuel expenditure in the marine transport system. Less obvious but also high-impact targets include heating, ventilation, and air conditioning (HVAC) systems, Figure 48C ; hydrocarbon fuel tanks and lines, Figure 48D; and water distribution, Figure 48E. HVAC systems and cooling towers are ubiquitous in most buildings and industrial plants. Preventing their contamination would address not only interior occupants' exposure to often fatal infections such as Legionnaire's disease, but also those who are present as far as 6 km away. (162) Another high-impact target for preventing the attachment of biofilm would be aircraft and other fuel tanks, as bacteria frequently contaminate jet fuel and cause corrosion of the tank and fuel line metals. (163) Toxic biocidal fuel additives are used in military fuel, but this increases environmental pollution and may lead to resistant bacterial strains. (164) Water distribution systems ranging from mains to fountains are subject to biofilm contamination at all stages and would also be a logical target application. Water distribution in hospitals is especially critical, where the addition of biocidal compounds poses risks to patients, indeed sometimes no less than the presence of the bacteria itself. (165)

## 8. Appendix

### A. Hierarchical fibrous superhydrophobic surfaces for tunable wetting properties<sup>5</sup>

In many situations, it is necessary or desirable to control the wetting properties of a surface, that is, how a liquid spreads on the surface or beads up and even rolls off. Anti-fog shower mirrors must be hydrophilic such that moisture condenses in a specular film that maintains the optical function of the mirror. Vehicle windshields, in contrast, are chemically treated for water repellency to promote water removal by wind. But to achieve both greater control of wetting and wetting function longevity, more than surface chemical treatments must be used. The physical texture of a surface, specifically the roughness and presence of tall or overhanging structures, generally leads to an amplification of the surface chemistry, with the result in principle ranging from full wetting ( $0^\circ$  apparent contact angle between liquid and solid) to full repellency ( $180^\circ$ ). (48, 166-167) The natural model of the Lotus leaf, which combines micro- and nano-scale surface structures with hydrophobic wax chemistry, has motivated two decades of work in designing synthetic surface morphologies to control wetting. (43, 168-169) Recently, PPy nanofiber arrays have been shown to exhibit superhydrophilicity with a contact angle near zero. (170) However, the same fiber network can also exhibit superhydrophobicity (171-172) after appropriate chemical treatment. Large-area samples of both nanofibers and low-pH, hierarchical morphologies were treated with perfluorooctyl trichlorosilane for 24 hours in a vacuum desiccator. Therefore, with

---

<sup>5</sup> These results are to be published in *Small*.

identical surface chemistry, the effect of the nanostructure on wetting angle could be determined. The contact angle of water droplets placed on the PPy nanofiber-coated surface (shown in Figure 49a) in normal atmosphere was measured to be  $148.4^\circ$  with a standard deviation of  $9.1^\circ$ . The water contact angle of the polypyrrole hierarchical structure (shown in Figure 49b) created via the single deposition at low pH was measured to be  $126.8^\circ$  with a standard deviation of  $10.0^\circ$ . Although not tested, a combination of both morphologies, with the fibers created in a second deposition step on already-deposited hierarchical structures obtained at low pH would likely exhibit a higher water contact angle than either morphology alone.

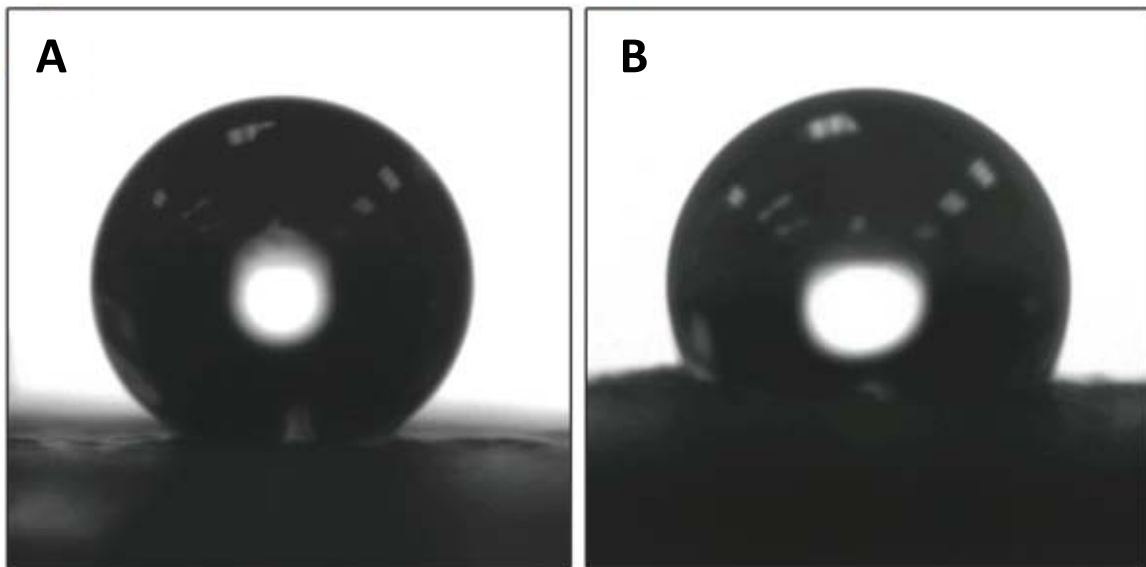


Figure 49. Photographs of a water droplet sitting on large area of bulk deposited polypyrrole structures to show the contact angle between the two surfaces in air. Deposition conditions in image (a) were: 0.075 M Py, 0.25 M PBS (pH 7.5), 0.07 M LiClO<sub>4</sub>, 10 minutes at 0.85 V resulting in nanofibers. Deposition conditions in image (b) were: 0.075 M Py, 0.25 M PBS (pH 5.8), and 0.07 M LiClO<sub>4</sub>, 10 minutes at 0.85 V resulting in low pH hierarchical structures.

The natural “lotus effect” of surface liquid repellency and roll-off is limited to water. However, water possesses exceptionally high surface tension, 72.8 mN/m at 20° C, in contrast to many liquids relevant in manmade settings. For instance, the surface tension of alcohols is ~22 mN/m, causing even dilute mixtures of ethanol and water to wet extremely readily on most surfaces. A recent study reported that a bacterial biofilm, unlike the lotus, could resist wetting by such low surface tension mixtures. (173)

Adapting the same methodology, we characterized the wetting properties of three synthetic surfaces (Figure 50a-c) as a function of surface tension by varying the test liquid’s volume fraction of ethanol. In addition to starting with a flat epoxy substrate, we also employed a high-aspect-ratio (AR = 32) epoxy nanopost array as described previously, (174) and decorated certain replicas of both substrates with PPy fiber. The surfaces thus represented conditions of no topography, two single-length-scale topographies, and a hierarchical surface. All were chemically treated to be hydrophobic, as described above. Shown in Figure 50d, the contact angle of liquid on the flat surface decreased from ~110° to ~40°, whereas all the textured surfaces functioned in the superhydrophobic regime (>150°) up to 40% ethanol. As the surface tension was further decreased, the nanoposts failed, undergoing a Cassie (liquid atop the structures) to Wenzel (fully wetted) transition. The flat-fiber surface failed more gradually between the 50% and 70% ethanol levels, and the hierarchical nanopost-fiber surface robustly maintained the Cassie state up to 80% ethanol before failing. The superhydrophobic robustness of the hierarchical surface, under up to 80% ethanol, is consistent with greatly increased interfacial area occurring between the liquid and air trapped within the posts and reentrant PPy fibrous network.

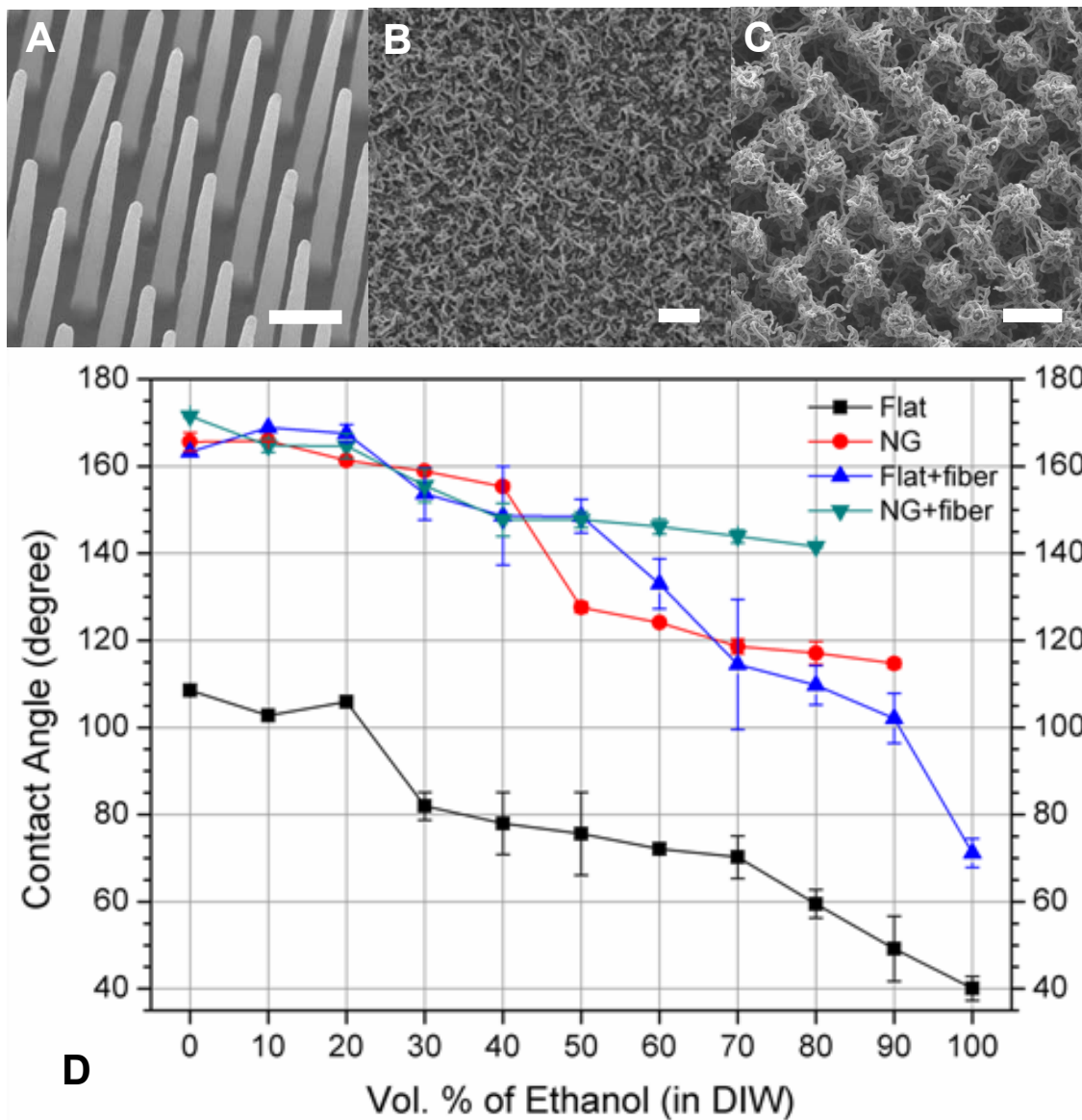


Figure 50. Three nanostructured surfaces and their wetting properties. (a)-(c): SEM images of (a) a square array of  $h = 8 \mu\text{m}$ ,  $d = 200 \text{ nm}$  epoxy nanopillars with  $2 \mu\text{m}$  pitch, (b) PPy nanofiber on a flat substrate, (c) a hierarchical structure combining (a) and (b). Scale bars represent  $2 \mu\text{m}$ . (d): Static contact angles of a droplet of water-ethanol mixture on various substrates. Flat: flat epoxy substrate; NG, Flat + fiber, NG + fiber represent the structures shown in (a), (b), and (c), respectively.

Because of the high surface area, porosity and three-dimensionality of the electrodes coated in PPy nanofibers, these surfaces would also be useful for either impregnation with another material or a secondary deposition of a non-conductive material. For example, the nanofiber network would be a suitable substrate for the addition of a lubricating film to create a slippery surface using the SLIPS method. (143) Furthermore, our nanofiber networks could provide a 3D electrode onto which hydrogel could be electrochemically deposited. (175) The possible thickness of electrochemically deposited hydrogel is limited by the poor conductivity of the hydrogel. However, starting with a 3D substrate could provide the conductive pathways for the deposition of thicker films of hydrogel.

### **Experimental Method Details**

*Contact Angle Experiments.* Water contact angle experiments were performed by first creating large sample areas using bulk deposition in the conditions found from the gradient experiments. The samples were treated with Perfluorooctyl trichlorosilane for 24 hours in a vacuum desiccator. Small droplets of water were placed in multiple areas over the surface of the samples and observed using a video camera. The angle was then estimated from the photos using photo analysis software.

*Electrodeposition.* All chemicals were purchased from Sigma-Aldrich and used as received except for pyrrole. Pyrrole was purified by double filtering through an alumin-packed plastic disposable syringe immediately before use. The applied potential was controlled by a computer-controlled potentiostat/galvanostat (Versastat 3, Princeton Applied Research).

## B. Copyright permissions

### JOHN WILEY AND SONS LICENSE TERMS AND CONDITIONS

Mar 08, 2012

This is a License Agreement between Alexander K Epstein ("You") and John Wiley and Sons

("John Wiley and Sons") provided by Copyright Clearance Center ("CCC"). The license consists of your order details, the terms and conditions provided by John Wiley and Sons, and the payment terms and conditions.

License Number 2864390459658

License date Mar 08, 2012

Licensed content publisher John Wiley and Sons

Licensed content publication Advanced Materials

Licensed content title Fabrication of Bioinspired Actuated Nanostructures with Arbitrary Geometry and Stiffness

Licensed content author Boaz Pokroy, Alexander K. Epstein, Maria C. M. Persson-Gulda, Joanna Aizenberg

Licensed content date Jan 26, 2009

Start page 463

End page 469

Type of use Dissertation/Thesis

Requestor type Author of this Wiley article

Format Electronic

Portion Full article

Will you be translating? No

Order reference number

Total 0.00 USD

DOI: 10.1002/adma.200801432



**CAMBRIDGE UNIVERSITY PRESS LICENSE  
TERMS AND CONDITIONS**

Mar 08, 2012

This is a License Agreement between Alexander K Epstein ("You") and Cambridge University Press ("Cambridge University Press") provided by Copyright Clearance Center

("CCC"). The license consists of your order details, the terms and conditions provided by Cambridge University Press, and the payment terms and conditions.

License Number 2864390889844

License date Mar 08, 2012

Licensed content publisher Cambridge University Press

Licensed content publication MRS Online Proceedings Library

Licensed content title Biomimetic Nanostructured Surfaces with Designer Mechanics and Geometry for Broad Applications

Licensed content author Alexander K Epstein and Joanna Aizenberg

Licensed content date Dec 31, 1969

Volume number 1236

Issue number -1

Start page 0

End page 0

Type of Use Dissertation/Thesis

Requestor type Author

Portion Full article

Author of this Cambridge

University Press article Yes

Author / editor of the new work Yes

Order reference number

Territory for reuse North America Only

Title of your thesis / dissertation

Bioinspired, dynamic, structured surfaces for biofilm attachment prevention

Expected completion date Jun 2012

Estimated size(pages) 130

Billing Type Invoice

Billing address 278 Beacon Street

Apt. 55

Somerville, MA 02143

United States

Customer reference info

Total 0.00 USD

DOI: 10.1557/PROC-1236-SS09-07

**Title:** Structural Transformation by Electrodeposition on Patterned Substrates (STEPS):  
A New Versatile Nanofabrication Method

**Author:** Philseok Kim et al.

**Publication:** Nano Letters

**Publisher:** American Chemical Society

**Date:** Feb 1, 2012

Copyright © 2012, American Chemical Society

Logged in as: Alexander Epstein

**PERMISSION/LICENSE IS GRANTED FOR YOUR ORDER AT NO CHARGE**

This type of permission/license, instead of the standard Terms & Conditions, is sent to you because no fee is being charged for your order. Please note the following: Permission is granted for your request in both print and electronic formats. If figures and/or tables were requested, they may be adapted or used in part. Please print this page for your records and send a copy of it to your publisher/graduate school.

Appropriate credit for the requested material should be given as follows: "Reprinted (adapted) with permission from (COMPLETE REFERENCE CITATION). Copyright (YEAR) American Chemical Society." Insert appropriate information in place of the capitalized words.

One-time permission is granted only for the use specified in your request. No additional uses are granted (such as derivative works or other editions). For any other uses, please submit a new request.

DOI: 10.1021/nl200426g

**Title:** Steering nanofibers: An integrative approach to bio-inspired fiber fabrication and assembly

**Author:** A. Grinthal, S.H. Kang, A.K Epstein, M. Aizenberg, M. Khan, J.Aizenberg

**Publication:** Nano Today

**Publisher:** Elsevier

**Date:** February 2012

Copyright © 2012, Elsevier

Logged in as: Alexander Epstein

Account #: 3000508172

**Order Completed**

Thank you very much for your order.

This is a License Agreement between Alexander K Epstein ("You") and Elsevier ("Elsevier"). The license consists of your order details, the terms and conditions provided by Elsevier, and the payment terms and conditions.

[Get the printable license.](#)

License Number 2866520103295

License date Mar 12, 2012

Licensed content publisher Elsevier

Licensed content publication Nano Today

Licensed content title Steering nanofibers: An integrative approach to bio-inspired fiber fabrication and assembly

Licensed content author A. Grinthal, S.H. Kang, A.K Epstein, M. Aizenberg, M. Khan, J. Aizenberg

Licensed content date February 2012

Licensed content volume number 7

Licensed content issue number 1

Number of pages 18

Type of Use reuse in a thesis/dissertation

Portion full article

Format electronic

Are you the author of this Elsevier article? Yes

Will you be translating? No

Order reference number

Title of your thesis/dissertation Bioinspired, dynamic, structured surfaces for biofilm attachment prevention

Expected completion date Jun 2012

Estimated size (number of pages) 130

Elsevier VAT number GB 494 6272 12

Permissions price 0.00 USD

VAT/Local Sales Tax 0.0 USD / 0.0

DOI: 10.1016/j.nantod.2011.12.005

**Title:** Bacterial biofilm shows persistent resistance to liquid wetting and gas penetration  
**Author:** A.K Epstein, B. Pokroy, A. Seminara, J.Aizenberg  
**Publication:** Proceedings of the National Academy of Sciences  
**Publisher:** National Academy of Sciences

**PNAS Permissions** <PNASPermissions@nas.edu> **Mon, Mar 12, 2012 at 10:31 AM**  
To: Alexander K Epstein <aepstein@seas.harvard.edu>

Dear Dr. Epstein,

Authors need not obtain permission for the following uses of material they have published in PNAS: (1) to use their original figures or tables in their future works; (2) to make copies of their papers for their classroom teaching; or (3) to include their papers as part of their dissertations.

Of course, citation to the original source should be included (full journal references).

Please feel free to contact us with any additional questions you might have.

Thank you!

Best regards,  
Kelly Gerrity for  
Diane Sullenberger  
Executive Editor  
PNAS

DOI: 10.1073/pnas.1011033108

**Title:** Control of bacterial biofilm growth on surfaces by nanostructural mechanics and geometry

**Author:** A.K Epstein, A.I. Hochbaum, P. Kim, J.Aizenberg

**Publication:** Nanotechnology

**Publisher:** IOP Publishing, Ltd

DOI:10.1088/0957-4484/22/49/494007



To: permissions@iop.org,  
Cc:  
Bcc:  
Subject: Permission to reprint in dissertation  
From: Alexander K Epstein <aepstein@seas.harvard.edu> - Monday 12/03/2012 15:07  
Sent by: alexepstein@gmail.com

Dear IOP:

I am writing to request permission to reprint my *Nanotechnology* publication "Control of bacterial biofilm growth on surfaces by nanostructural mechanics and geometry" (<http://iopscience.iop.org/0957-4484/22/49/494007/>) as part of my dissertation. I understand that I need not seek permission for this use, but if a notice of explicit permission can be provided nevertheless, I would appreciate it. Otherwise, could you confirm that the Copyright Notice that I must show in my dissertation appendix is this one: <http://www.iop.org/copyright/index.html>

Thank you,  
Alex Epstein

--

Alexander K Epstein  
PhD Candidate '12 in Engineering Sciences  
School of Engineering and Applied Sciences  
Harvard University

PERMISSION TO REPRODUCE AS REQUESTED IS GIVEN PROVIDED THAT:

- (a) ~~the consent of the author(s) is obtained~~
- (b) the source of the material including author, title of article, title of journal, volume number, issue number (if relevant), page range (or first page if this is the only information available), date and publisher is acknowledged.
- (c) for material being published electronically, a link back to the original article should be provided (via DOI).

IOP Publishing Ltd  
Temple Circus  
Temple Way  
BRISTOL  
BS1 6BE

13/03/2012  
Date

Sarah Lyde  
Rights & Permissions

## 9. List of publications

- Kim, P.; Burgoyne, H.; Kolle, M.; **Epstein, A.K**; Adorno, W.; Aizenberg, J. Screening Conditions for Rationally Engineered Electrodeposition of Nanostructures (SCREEN): Deposition of Polypyrrole Nanofibers using Microfluidic Gradients. Submitted to *Small*.
- Epstein, A.K**; Hong, D.; Kim, P.; Aizenberg, J. Biofilm attachment reduction on bio-inspired, dynamic, micro-wrinkling surfaces. In preparation for submission to *New Journal of Physics*.
- Epstein, A.K**; Wong, T.-S.; Boggs, E.M.; Belisle, R.A.; Aizenberg, J. Effective Resistance of Liquid-Infused Porous Surfaces to Biofilm Attachment under Static and Flow Conditions. In revision for *Proc. Natl Acad Sci USA*, 2012.
- Grinthal, A.; Kang, S.H.; **Epstein, A.K**; Aizenberg, M.; Khan, M, Aizenberg, J. Steering nanofibers: Integrative approach to bio-inspired fiber fabrication and assembly. *Nano Today* 2011, 7, 35-52.
- Epstein, A. K.**; Hochbaum, A.I.; Khan, M; Kim, P; Aizenberg, J. Control of bacterial biofilm growth on surfaces by nanostructural mechanics and geometry. *Nanotechnology*, 2011, 22, 494007.
- Kim, P.; **Epstein, A. K.**; Khan, M.; Zarzar, L. D.; Lipomi, D. J.; Whitesides, G. M.; Aizenberg, J. Structural Transformation by Electrodeposition on Patterned Substrates (STEPS): A New Versatile Nanofabrication Method. *Nano Letters*, 2011, 12, 527-533.
- Epstein, A. K.**; Pokroy, B.; Seminara, A.; Aizenberg, J. Bacterial biofilm shows persistent resistance to liquid wetting and gas penetration. *Proc. Natl Acad Sci USA*, 2011, **108** (3), 995-1000.
- Epstein, A.**; Aizenberg, J. Biomimetic Nanostructured Surfaces with Designer Mechanics and Geometry for Broad Applications, *Mater. Res. Soc. Symp. Proc.*, 2010, 1236E:1236-SS1209-1207.
- Pokroy, B.; **Epstein, A. K.**; Persson-Gulda, M. C. M.; Aizenberg, J., Fabrication of Bioinspired Actuated Nanostructures with Arbitrary Geometry and Stiffness. *Adv Mater*, 2009, **21** (4), 463-469.

## 10. References

1. Hogan CM (2010) Bacteria. *Encyclopedia of Earth*, ed Sidney Draggan CJC (Environmental Information Coalition, National Council for Science and the Environment, Washington, D.C.).
2. Shapiro J (1998) Thinking about bacterial populations as multicellular organisms. *Annual Reviews in Microbiology* 52(1):81-104.
3. Marsh P (2005) Dental plaque: biological significance of a biofilm and community life style. *Journal of clinical periodontology* 32:7-15.
4. Blango M & Mulvey M (2009) Bacterial landlines: contact-dependent signaling in bacterial populations. *Curr Opin Microbiol* 12(2):177-181.
5. Ben-Jacob E, Cohen I, & Gutnick DL (1998) Cooperative organization of bacterial colonies: from genotype to morphotype. *Annual Reviews in Microbiology* 52(1):779-806.
6. Klausen M, Aaes Jørgensen A, Molin S, & Tolker Nielsen T (2003) Involvement of bacterial migration in the development of complex multicellular structures in *Pseudomonas aeruginosa* biofilms. *Molecular microbiology* 50(1):61-68.
7. Stewart PS & Franklin MJ (2008) Physiological heterogeneity in biofilms. *Nat Rev Microbiol* 6(3):199-210.
8. Vlamakis H, Aguilar C, Losick R, & Kolter R (2008) Control of cell fate by the formation of an architecturally complex bacterial community. *Genes & development* 22(7):945.
9. Epstein A, Pokroy B, Seminara A, & Aizenberg J (2010) Bacterial biofilm shows persistent resistance to liquid wetting and gas penetration. *Proceedings of the National Academy of Sciences*.
10. Costerton JW & Stewart PS (2001) Battling biofilms - The war is against bacterial colonies that cause some of the most tenacious infections known. The weapon is knowledge of the enemy's communication system. *Sci Am* 285(1):74-81.
11. Dalley AACaR (1987) Barnacle fouling and its prevention. *Barnacle Biology*, ed Southward AJ (A. A. Balkema, Rotterdam, NL), pp 419-433.
12. Davies D (2003) Understanding biofilm resistance to antibacterial agents. *Nat Rev Drug Discov* 2(2):114-122.
13. Klevens R, *et al.* (2007) Estimating health care-associated infections and deaths in US hospitals, 2002. *Public Health Rep* 122(2):160.
14. Klevens RM, *et al.* (2007) Estimating health care-associated infections and deaths in US hospitals, 2002. *Public Health Rep* 122(2):160-166.
15. Sadykov MR, *et al.* (2008) Tricarboxylic acid cycle-dependent regulation of *Staphylococcus epidermidis* polysaccharide intercellular adhesin synthesis. *J Bacteriol* 190(23):7621-7632.
16. Banerjee I, Pangule R, & Kane R (2010) Antifouling Coatings: Recent Developments in the Design of Surfaces That Prevent Fouling by Proteins, Bacteria, and Marine Organisms. *Adv Mater*.
17. Autumn K, *et al.* (2002) Evidence for van der Waals adhesion in gecko setae. *Proceedings of the National Academy of Sciences* 99(19):12252.
18. Harris JM (1992) *Poly(ethylene glycol) chemistry: biotechnical and biomedical applications*. (Plenum Press, New York).

19. Jiang S & Cao Z (2010) Ultralow Fouling, Functionalizable, and Hydrolyzable Zwitterionic Materials and Their Derivatives for Biological Applications. *Adv Mater* 22(9):920-932.
20. Gudipati CS, Finlay JA, Callow JA, Callow ME, & Wooley KL (2005) The antifouling and fouling-release performance of hyperbranched fluoropolymer (HBFP)-poly (ethylene glycol)(PEG) composite coatings evaluated by adsorption of biomacromolecules and the green fouling alga ulva. *Langmuir* 21(7):3044-3053.
21. Purevdorj B, Costerton J, & Stoodley P (2002) Influence of hydrodynamics and cell signaling on the structure and behavior of *Pseudomonas aeruginosa* biofilms. *Applied and environmental microbiology* 68(9):4457.
22. Scardino AJ & De Nys R (2010) Mini review: Biomimetic models and bioinspired surfaces for fouling control. *Biofouling* 27(1):73-86.
23. Bos R, Mei H, Gold J, & Busscher H (2000) Retention of bacteria on a substratum surface with micro patterned hydrophobicity. *Fems Microbiol Lett* 189(2):311-315.
24. Gristina A (1987) Biomaterial-centered infection: microbial adhesion versus tissue integration. *Science* 237(4822):1588.
25. Neu TR (1996) Significance of bacterial surface-active compounds in interaction of bacteria with interfaces. *Microbiol Mol Biol R* 60(1):151.
26. Hall-Stoodley L, Costerton JW, & Stoodley P (2004) Bacterial biofilms: from the natural environment to infectious diseases. *Nat Rev Microbiol* 2(2):95-108.
27. Trevors J (1987) Silver resistance and accumulation in bacteria. *Enzyme and Microbial Technology* 9(6):331-333.
28. Costerton J, Stewart P, & Greenberg E (1999) Bacterial biofilms: a common cause of persistent infections. *Science* 284(5418):1318.
29. McDonnell G & Russell AD (1999) Antiseptics and disinfectants: Activity, action, and resistance. *Clinical Microbiology Reviews* 12(1):147-179.
30. Ishida H, *et al.* (1998) In vitro and in vivo activities of levofloxacin against biofilm-producing *Pseudomonas aeruginosa*. *Antimicrob Agents Ch* 42(7):1641-1645.
31. Giwercman B, Jensen ET, Hoiby N, Kharazmi A, & Costerton JW (1991) Induction of Beta-Lactamase Production in *Pseudomonas-Aeruginosa* Biofilm. *Antimicrob Agents Ch* 35(5):1008-1010.
32. Lomovskaya O & Lewis K (1992) Emr, an *Escherichia coli* locus for multidrug resistance. *Proceedings of the National Academy of Sciences of the United States of America* 89(19):8938.
33. Branda S, Vik Å, Friedman L, & Kolter R (2005) Biofilms: the matrix revisited. *Trends in Microbiology* 13(1):20-26.
34. Anderson RL, Holland BW, Carr JK, Bond WW, & Favero MS (1990) Effect of Disinfectants on *Pseudomonads* Colonized on the Interior Surface of Pvc Pipes. *Am J Public Health* 80(1):17-21.
35. Panlilio AL, *et al.* (1992) Infections and Pseudoinfections Due to Povidone-Iodine Solution Contaminated with *Pseudomonas-Cepacia*. *Clin Infect Dis* 14(5):1078-1083.



36. Genzer J & Efimenko K (2006) Recent developments in superhydrophobic surfaces and their relevance to marine fouling: a review. *Biofouling* 22(5):339-360.
37. Meyer B (2003) Approaches to prevention, removal and killing of biofilms. *International biodeterioration & biodegradation* 51(4):249-253.
38. Zhao L, Chu PK, Zhang Y, & Wu Z (2009) Antibacterial coatings on titanium implants. *Journal of Biomedical Materials Research Part B: Applied Biomaterials* 91(1):470-480.
39. Park KD, *et al.* (1998) Bacterial adhesion on PEG modified polyurethane surfaces. *Biomaterials* 19(7-9):851-859.
40. Prime KL & Whitesides GM (1991) Self-assembled organic monolayers: model systems for studying adsorption of proteins at surfaces. *Science (New York, NY)* 252(5010):1164.
41. Bos R, Mei H, & Busscher H (1999) Physico chemistry of initial microbial adhesive interactions—its mechanisms and methods for study. *Fems Microbiol Rev* 23(2):179-230.
42. Neu T (1996) Significance of bacterial surface-active compounds in interaction of bacteria with interfaces. *Microbiol Mol Biol R* 60(1):151.
43. Barthlott W & Neinhuis C (1997) Purity of the sacred lotus, or escape from contamination in biological surfaces. *Planta* 202(1):1-8.
44. Aguilar C, Vlamakis H, Losick R, & Kolter R (2007) Thinking about *Bacillus subtilis* as a multicellular organism. *Curr Opin Microbiol* 10(6):638-643.
45. Branda SS, Gonzalez-Pastor JE, Ben-Yehuda S, Losick R, & Kolter R (2001) Fruiting body formation by *Bacillus subtilis*. *Proceedings of the National Academy of Sciences of the United States of America* 98(20):11621-11626.
46. Tuteja A, Choi W, Mabry JM, McKinley GH, & Cohen RE (2008) Robust omniphobic surfaces. *Proceedings of the National Academy of Sciences of the United States of America* 105(47):18200-18205.
47. Branda SS, Chu F, Kearns DB, Losick R, & Kolter R (2006) A major protein component of the *Bacillus subtilis* biofilm matrix. *Molecular Microbiology* 59(4):1229-1238.
48. Cassie A & Baxter S (1944) Wettability of porous surfaces. *Trans. Faraday Soc.* 40:546-551.
49. Roach P, Shirtcliffe NJ, & Newton MI (2008) Progress in superhydrophobic surface development. *Soft Matter* 4(2):224-240.
50. Tuteja A, *et al.* (2007) Designing superoleophobic surfaces. *Science* 318(5856):1618-1622.
51. Pokroy B, Epstein AK, Persson-Gulda MCM, & Aizenberg J (2009) Fabrication of Bioinspired Actuated Nanostructures with Arbitrary Geometry and Stiffness. *Adv Mater* 21(4):463-+.
52. Furstner R, Barthlott W, Neinhuis C, & Walzel P (2005) Wetting and self-cleaning properties of artificial superhydrophobic surfaces. *Langmuir* 21(3):956-961.
53. Dorman HJD & Deans SG (2000) Antimicrobial agents from plants: antibacterial activity of plant volatile oils. *J Appl Microbiol* 88(2):308-316.

54. Hoffman RK & Warshowsky B (1958) Beta-Propiolactone Vapor as a Disinfectant. *Appl Microbiol* 6(5):358-362.
55. Sapers GM, Walker PN, Sites JE, Annous BA, & Eblen DR (2003) Vapor-phase decontamination of apples inoculated with *Escherichia coli*. *J Food Sci* 68(3):1003-1007.
56. Simmons GF, Smilanick JL, John S, & Margosan DA (1997) Reduction of microbial populations on prunes by vapor-phase hydrogen peroxide. *J Food Protect* 60(2):188-191.
57. Bais HP, Fall R, & Vivanco JM (2004) Biocontrol of *Bacillus subtilis* against infection of *Arabidopsis* roots by *Pseudomonas syringae* is facilitated by biofilm formation and surfactin production. *Plant Physiol* 134(1):307-319.
58. Angelini TE, Roper M, Kolter R, Weitz DA, & Brenner MP (2009) *Bacillus subtilis* spreads by surfing on waves of surfactant. *Proceedings of the National Academy of Sciences of the United States of America* 106(43):18109-18113.
59. Be'er A, *et al.* (2009) *Paenibacillus dendritiformis* Bacterial Colony Growth Depends on Surfactant but Not on Bacterial Motion. *J Bacteriol* 191(18):5758-5764.
60. Aussillous P & Quere D (2001) Liquid marbles. *Nature* 411(6840):924-927.
61. Blossey R (2003) Self-cleaning surfaces - virtual realities. *Nat Mater* 2(5):301-306.
62. Feng L, *et al.* (2002) Super-hydrophobic surfaces: From natural to artificial. *Adv Mater* 14(24):1857-1860.
63. Gao XF & Jiang L (2004) Water-repellent legs of water striders. *Nature* 432(7013):36-36.
64. Ahuja A, *et al.* (2008) Nanonails: A simple geometrical approach to electrically tunable superhydrophobic surfaces. *Langmuir* 24(1):9-14.
65. Ruibal R & Ernst V (1965) Structure of Digital Setae of Lizards. *Journal of Morphology* 117(3):271.
66. Autumn K, *et al.* (2006) Dynamics of geckos running vertically. *Journal of Experimental Biology* 209(2):260-272.
67. Aizenberg J, Sundar VC, Yablon AD, Weaver JC, & Chen G (2004) Biological glass fibers: Correlation between optical and structural properties. *Proceedings of the National Academy of Sciences of the United States of America* 101(10):3358-3363.
68. Sundar VC, Yablon AD, Grazul JL, Ilan M, & Aizenberg J (2003) Fibre-optical features of a glass sponge - Some superior technological secrets have come to light from a deep-sea organism. *Nature* 424(6951):899-900.
69. McHenry MJ & van Netten SM (2007) The flexural stiffness of superficial neuromasts in the zebrafish (*Danio rerio*) lateral line. *Journal of Experimental Biology* 210(23):4244-4253.
70. Montgomery J & Coombs S (1992) Physiological Characterization of Lateral Line Function in the Antarctic Fish *Trematomus-Bernacchii*. *Brain Behavior and Evolution* 40(5):209-216.
71. Ruppert EE, Fox RS, & Barnes RB (2004) *Invertebrate zoology* (Brooks Cole Thomson, Belmont, CA) 7th Ed.

72. Huber G, *et al.* (2005) Evidence for capillarity contributions to gecko adhesion from single spatula nanomechanical measurements. *Proceedings of the National Academy of Sciences of the United States of America* 102(45):16293-16296.
73. Rios PF, Dodiuk H, Kenig S, McCarthy S, & Dotan A (2007) Transparent ultra-hydrophobic surfaces. *Journal of Adhesion Science and Technology* 21(5-6):399-408.
74. Geim AK, *et al.* (2003) Microfabricated adhesive mimicking gecko foot-hair. *Nature Materials* 2(7):461-463.
75. del Campo A, Greiner C, & Arzt E (2007) Contact shape controls adhesion of bioinspired fibrillar surfaces. *Langmuir* 23(20):10235-10243.
76. Peleshanko S, *et al.* (2007) Hydrogel-encapsulated microfabricated haircells mimicking fish cupula neuromast. *Advanced Materials* 19(19):2903-2909.
77. Sidorenko A, Krupenkin T, Taylor A, Fratzl P, & Aizenberg J (2007) Reversible switching of hydrogel-actuated nanostructures into complex micropatterns. *Science* 315(5811):487-490.
78. Schumacher J, *et al.* (2007) Engineered antifouling microtopographies—effect of feature size, geometry, and roughness on settlement of zoospores of the green alga *Ulva*. *Biofouling* 23(1):55-62.
79. McKenzie J & Grigolava I (1996) The echinoderm surface and its role in preventing microfouling. *Biofouling* 10(1-3):261-272.
80. Campbell A & Rainbow P (1977) The role of pedicellariae in preventing barnacle settlement on the sea-urchin test. *Marine & Freshwater Behaviour & Phy* 4(4):253-260.
81. Ralston E & Swain G (2009) Bioinspiration—the solution for biofouling control? *Bioinspiration & biomimetics* 4:015007.
82. Discher D, Janmey P, & Wang Y (2005) Tissue cells feel and respond to the stiffness of their substrate. *Science* 310(5751):1139.
83. Huebsch N, *et al.* (2010) Harnessing traction-mediated manipulation of the cell/matrix interface to control stem-cell fate. *Nat Mater.*
84. Stevens MM & George JH (2005) Exploring and engineering the cell surface interface. *Science* 310(5751):1135-1138.
85. Davey M & O'toole G (2000) Microbial biofilms: from ecology to molecular genetics. *Microbiol Mol Biol R* 64(4):847.
86. Hochbaum A & Aizenberg J (2010) Bacteria Pattern Spontaneously on Periodic Nanostructure Arrays. *Nano Lett.*
87. Zhao XM, Xia Y, & Whitesides GM (1997) Soft lithographic methods for nanofabrication. *J. Mater. Chem.* 7(7):1069-1074.
88. Xia YN & Whitesides GM (1995) Reduction in the Size of Features of Patterned Sams Generated by Microcontact Printing with Mechanical Compression of the Stamp. *Advanced Materials* 7(5):471-473.
89. Xia YN & Whitesides GM (1998) Soft lithography. *Annual Review of Materials Science* 28:153-184.
90. Xia YN & Whitesides GM (1998) Soft lithography. *Angewandte Chemie-International Edition* 37(5):551-575.

91. Tan JL, *et al.* (2003) Cells lying on a bed of microneedles: An approach to isolate mechanical force. *Proceedings of the National Academy of Sciences of the United States of America* 100(4):1484-1489.
92. Zheng ZJ, Azzaroni O, Zhou F, & Huck WTS (2006) Topography printing to locally control wettability. *Journal of the American Chemical Society* 128(24):7730-7731.
93. Courbin L, *et al.* (2007) Imbibition by polygonal spreading on microdecorated surfaces. *Nature Materials* 6(9):661-664.
94. Roca-Cusachs P, *et al.* (2005) Stability of microfabricated high aspect ratio structures in poly(dimethylsiloxane). *Langmuir* 21(12):5542-5548.
95. Pokroy B, Epstein AK, Persson-Gulda MCM, & Aizenberg J (2009) Fabrication of Bioinspired Actuated Nanostructures with Arbitrary Geometry and Stiffness. *Adv. Mater.* 21(4):463-469.
96. Epstein AK, Aizenberg, J. (2010) Biomimetic Nanostructured Surfaces with Designer Mechanics and Geometry for Broad Applications. *Mater. Res. Soc. Symp. Proc.* 1236E:1236-SS1209-1207
97. Kim P, *et al.* (Structural Transformation by Electrodeposition on Patterned Substrates (STEPS): A New Versatile Nanofabrication Method. *Nano Lett.* DOI: 10.1021/nl200426g.
98. Epstein AK, Pokroy B, Seminara A, & Aizenberg J (2011) Bacterial biofilm shows persistent resistance to liquid wetting and gas penetration. *Proc. Natl. Acad. Sci. USA* 108(3):995-1000.
99. McAuley SA, *et al.* (2001) Silicon micromachining using a high-density plasma source. *Journal of Physics D-Applied Physics* 34(18):2769-2774.
100. Krupenkin TN, Taylor JA, Schneider TM, & Yang S (2004) From rolling ball to complete wetting: The dynamic tuning of liquids on nanostructured surfaces. *Langmuir* 20(10):3824-3827.
101. Ruibal R & Ernst V (1965) Structure of Digital Setae of Lizards. *J. Morphol.* 117(3):271-294.
102. Autumn K, Dittmore A, Santos D, Spenko M, & Cutkosky M (2006) Frictional adhesion: a new angle on gecko attachment. *J. Exp. Biol.* 209(18):3569-3579.
103. Zhao BX, *et al.* (2008) Adhesion and friction force coupling of gecko setal arrays: Implications for structured adhesive surfaces. *Langmuir* 24(4):1517-1524.
104. Sommers AD & Jacobi AM (2006) Creating micro-scale surface topology to achieve anisotropic wettability on an aluminum surface. *Journal of Micromechanics and Microengineering* 16(8):1571-1578.
105. Lotters JC, Olthuis W, Veltink PH, & Bergveld P (1997) The mechanical properties of the rubber elastic polymer polydimethylsiloxane for sensor applications. *Journal of Micromechanics and Microengineering* 7(3):145-147.
106. Epstein AK, Aizenberg, J. (2010) Biomimetic Nanostructured Surfaces with Designer Mechanics and Geometry for Broad Applications. *Mater. Res. Soc. Symp. Proc.* 1236E:1236-SS1209-1207
107. Pokroy B, Kang SH, Mahadevan L, & Aizenberg J (2009) Self-Organization of a Mesoscale Bristle into Ordered, Hierarchical Helical Assemblies. *Science* 323(5911):237-240.

108. Seminara A, Pokroy B, Kang SH, Brenner MP, & Aizenberg J (2011) Mechanism of nanostructure movement under an electron beam and its application in patterning. *Physical Review B* 83(23):235438.
109. Chang C, *et al.* (2005) Etching submicrometer trenches by using the Bosch process and its application to the fabrication of antireflection structures. *J. Micromech. Microeng.* 15:580.
110. Kim P, Zarzar LD, Khan M, Aizenberg M, & Aizenberg J (2011) Environmentally responsive active optics based on hydrogel-actuated deformable mirror arrays. *SPIE Photonics West*, (SPIE), pp 792705-792711.
111. Hochbaum AI & Aizenberg J (2010) Bacteria Pattern Spontaneously on Periodic Nanostructure Arrays. *Nano Lett.* 10(9):3717-3721.
112. Bettinger CJ, Borenstein JT, & Langer R (2009) Engineering Substrate Topography at the Micro- and Nanoscale to Control Cell Function. *Angew. Chem. Int. Ed.* 48(30):5406-5415.
113. Mishchenko L, *et al.* (2010) Design of Ice-free Nanostructured Surfaces Based on Repulsion of Impacting Water Droplets. *ACS Nano*.
114. Zhang Y, Lo CW, Taylor JA, & Yang S (2006) Replica molding of high-aspect-ratio polymeric nanopillar arrays with high fidelity. *Langmuir* 22(20):8595-8601.
115. Hui CY, Jagota A, Lin YY, & Kramer EJ (2002) Constraints on microcontact printing imposed by stamp deformation. *Langmuir* 18(4):1394-1407.
116. Ragab AR & Bayoumi SEA (1998) *Engineering Solid Mechanics: Fundamentals and Applications* (CRC Press, Boca Raton, FL).
117. Autumn K, Majidi C, Groff RE, Dittmore A, & Fearing R (2006) Effective elastic modulus of isolated gecko setal arrays. *J. Exp. Biol.* 209(18):3558-3568.
118. Tong T, *et al.* (2008) Height independent compressive modulus of vertically aligned carbon nanotube arrays. *Nano Lett.* 8(2):511-515.
119. Wang LF, Ortiz C, & Boyce MC (2011) Mechanics of Indentation into Micro- and Nanoscale Forests of Tubes, Rods, or Pillars. *J. Eng. Mater.-T. ASME* 133(1).
120. Schubert B, Lee J, Majidi C, & Fearing RS (2008) Sliding-induced adhesion of stiff polymer microfibre arrays. II. Microscale behaviour. *J. R. Soc. Lond. Interface* 5(25):845.
121. Xiu YH, Liu Y, Hess DW, & Wong CP (2010) Mechanically robust superhydrophobicity on hierarchically structured Si surfaces. *Nanotechnology* 21(15):155705.
122. Kim P, *et al.* (2011) Structural Transformation by Electrodeposition on Patterned Substrates (STEPS): A New Versatile Nanofabrication Method. *Nano Lett.*
123. Song JH, Wang XD, Riedo E, & Wang ZL (2005) Elastic property of vertically aligned nanowires. *Nano Lett.* 5(10):1954-1958.
124. Wu B, Heidelberg A, & Boland JJ (2005) Mechanical properties of ultrahigh-strength gold nanowires. *Nature Mater.* 4(7):525-529.
125. Cuenot S, Fretigny C, Demoustier-Champagne S, & Nysten B (2004) Surface tension effect on the mechanical properties of nanomaterials measured by atomic force microscopy. *Phys. Rev. B* 69(16).
126. Kahn H, Ballarini R, Mullen RL, & Heuer AH (1999) Electrostatically actuated failure of microfabricated polysilicon fracture mechanics specimens. *Proc. R. Soc. A* 455(1990):3807-3823.

127. van Melick HGH, Meijer HEH, & Govaert LE (2003) On the origin of strain hardening in glassy polymers. *Polymer* 44(8):2493-2502.
128. Epstein A, Hochbaum A, Kim P, & Aizenberg J (2011) Control of bacterial biofilm growth on surfaces by nanostructural mechanics and geometry. *Nanotechnology* 22:494007.
129. Epstein AKW, Tak-Sing; Boggs, Emily Marie; Belisle, Rebecca A.; Aizenberg, Joanna (In review) Effective Resistance of Liquid-Infused Porous Surfaces to Biofilm Attachment under Static and Flow Conditions.
130. Lichter J, *et al.* (2008) Substrata mechanical stiffness can regulate adhesion of viable bacteria. *Biomacromolecules* 9(6):1571-1578.
131. Grinthal A, *et al.* (2012) Steering nanofibers: An integrative approach to bio-inspired fiber fabrication and assembly. *Nano Today*.
132. Pokroy B, Epstein A, Persson Gulda M, & Aizenberg J (2009) Fabrication of bioinspired actuated nanostructures with arbitrary geometry and stiffness. *Adv Mater* 21(4):463-469.
133. Lötters J, Olthuis W, Veltink P, & Bergveld P (1997) The mechanical properties of the rubber elastic polymer polydimethylsiloxane for sensor applications. *Journal of Micromechanics and Microengineering* 7:145.
134. Kim P (2012) Private communication. ed Epstein AK (Cambridge, MA).
135. Shaw T, Winston M, Rupp C, Klapper I, & Stoodley P (2004) Commonality of elastic relaxation times in biofilms. *Physical review letters* 93(9):98102.
136. Boyd RD, Verran J, Jones M, & Bhakoo M (2002) Use of the atomic force microscope to determine the effect of substratum surface topography on bacterial adhesion. *Langmuir* 18(6):2343-2346.
137. Scardino A, Guenther J, & De Nys R (2008) Attachment point theory revisited: the fouling response to a microtextured matrix. *Biofouling* 24(1):45-53.
138. Gibbons R (1989) Bacterial adhesion to oral tissues: a model for infectious diseases. *Journal of dental research* 68(5):750-760.
139. Orstavik D, Kraus FW, & Henshaw LC (1974) In vitro attachment of streptococci to the tooth surface. *Infection and immunity* 9(5):794.
140. Fadeeva E, *et al.* (2011) Bacterial retention on superhydrophobic titanium surfaces fabricated by femtosecond laser ablation. *Langmuir*.
141. Poetes R, Holtzmann K, Franze K, & Steiner U (2010) Metastable Underwater Superhydrophobicity. *Physical review letters* 105(16):166104.
142. Bohn HF & Federle W (2004) Insect aquaplaning: Nepenthes pitcher plants capture prey with the peristome, a fully wettable water-lubricated anisotropic surface. *Proceedings of the National Academy of Sciences of the United States of America* 101(39):14138.
143. Wong TS, *et al.* (2011) Bioinspired self-repairing slippery surfaces with pressure-stable omniphobicity. *Nature* 477(7365):443-447.
144. Boswell PG & Bühlmann P (2005) Fluorous bulk membranes for potentiometric sensors with wide selectivity ranges: Observation of exceptionally strong ion pair formation. *Journal of the American Chemical Society* 127(25):8958-8959.
145. Zhang H, Hussam A, & Weber SG (2010) Properties and Transport Behavior of Perfluorotripropylamine (FC-70)-Doped Amorphous Teflon AF 2400 Films. *Journal of the American Chemical Society*.

146. Zhao H, Ismail K, & Weber SG (2004) How Fluorous Is Poly (2, 2-bis (trifluoromethyl)-4, 5-difluoro-1, 3-dioxido-co-tetrafluoroethylene)(Teflon AF)? *Journal of the American Chemical Society* 126(41):13184-13185.
147. Zhao H, *et al.* (2005) Transport of organic solutes through amorphous Teflon AF films. *Journal of the American Chemical Society* 127(43):15112-15119.
148. Khoo X, *et al.* (2010) Staphylococcus aureus resistance on titanium coated with multivalent PEGylated-peptides. *Biomaterials* 31(35):9285-9292.
149. Sugawara M & Stansfield BL (1998) *Plasma etching: fundamentals and applications* (Oxford University Press, USA).
150. Picknett R & Bexon R (1977) The evaporation of sessile or pendant drops in still air. *Journal of Colloid and Interface Science* 61(2):336-350.
151. Deegan RD, Bakajin O, & Dupont TF (1997) Capillary flow as the cause of ring stains from dried liquid drops. *Nature* 389(6653):827-829.
152. Jung J, Kim YW, Yoo JY, Koo J, & Kang YT (2010) Forces acting on a single particle in an evaporating sessile droplet on a hydrophilic surface. *Analytical chemistry* 82(3):784-788.
153. Wong TS, Chen TH, Shen X, & Ho CM (2011) Nanochromatography Driven by the Coffee Ring Effect. *Analytical chemistry*.
154. Tsai YP (2005) Impact of flow velocity on the dynamic behaviour of biofilm bacteria. *Biofouling* 21(5-6):267-277.
155. Gabe IT, *et al.* (1969) Measurement of instantaneous blood flow velocity and pressure in conscious man with a catheter-tip velocity probe. *Circulation* 40(5):603-614.
156. Ozawa H, Kumon H, Yokohama T, Watanabe T, & Chancellor MB (1998) Development of noninvasive velocity flow video urodynamics using Doppler sonography. Part II: clinical application in bladder outlet obstruction. *The Journal of Urology* 160(5):1792-1796.
157. O'Toole GA & Kolter R (1998) Initiation of biofilm formation in *Pseudomonas fluorescens* WCS365 proceeds via multiple, convergent signalling pathways: a genetic analysis. *Molecular microbiology* 28(3):449-461.
158. Lowe KC (2003) Engineering blood: synthetic substitutes from fluorinated compounds. *Tissue engineering* 9(3):389-399.
159. Gibiansky ML, *et al.* (2010) Bacteria use type IV pili to walk upright and detach from surfaces. *Science* 330(6001):197.
160. O'Toole GA & Kolter R (1998) Flagellar and twitching motility are necessary for *Pseudomonas aeruginosa* biofilm development. *Molecular Microbiology* 30(2):295-304.
161. Marcoux PR, *et al.* (2010) Micro-confinement of bacteria into w/o emulsion droplets for rapid detection and enumeration. *Colloids and Surfaces A: Physicochemical and Engineering Aspects*.
162. Nguyen TMN, *et al.* (2006) A community-wide outbreak of legionnaires disease linked to industrial cooling towers—how far can contaminated aerosols spread? *Journal of Infectious Diseases* 193(1):102-111.
163. McNamara CJ, *et al.* (2005) Corrosion of aluminum alloy 2024 by microorganisms isolated from aircraft fuel tanks. *Biofouling* 21(5-6):257-265.

164. Neihof RA (1988) Microbes in fuel: An overview with a naval perspective. *Distillate fuel: contamination, storage, and handling*:6-14.
165. Hoenich NA (2009) Disinfection of the hospital water supply: a hidden risk to dialysis patients. *Critical Care* 13(6):1007.
166. Wenzel RN (1936) Resistance of solid surfaces to wetting by water. *Industrial & Engineering Chemistry* 28(8):988-994.
167. Cassie A & Baxter S (1945) Large contact angles of plant and animal surfaces. *Nature* 155(3923):21-22.
168. Feng X & Jiang L (2006) Design and creation of superwetting/antiwetting surfaces. *Advanced Materials* 18(23):3063-3078.
169. Nosonovsky M & Bhushan B (2008) Biologically Inspired Surfaces: Broadening the Scope of Roughness\*\*. *Advanced Functional Materials* 18(6):843-855.
170. Zang J, *et al.* (2008) Template-free electrochemical synthesis of superhydrophilic polypyrrole nanofiber network. *Macromolecules* 41(19):7053-7057.
171. Darmanin T, Nicolas M, & Guittard F (2008) Synthesis and properties of perfluorinated conjugated polymers based on polyethylenedioxythiophene, polypyrrole, and polyfluorene. Toward surfaces with special wettabilities. *Langmuir* 24(17):9739-9746.
172. Teh K & Lu YW (2008) Surface nanostructuring of biocompatible polymer for wettability control in MEMS. (IEEE), pp 363-366.
173. Epstein AK, Pokroy B, Seminara A, & Aizenberg J (2011) Bacterial biofilm shows persistent resistance to liquid wetting and gas penetration. *Proceedings of the National Academy of Sciences* 108(3):995.
174. Pokroy B, Epstein AK, Persson-Gulda M, & Aizenberg J (2009) Fabrication of bioinspired actuated nanostructures with arbitrary geometry and stiffness. *Advanced Materials* 21(4):463-469.
175. Reuber J, Reinhardt H, & Johannsmann D (2006) Formation of surface-attached responsive gel layers via electrochemically induced free-radical polymerization. *Langmuir* 22(7):3362-3367.